



University of Pennsylvania  
**ScholarlyCommons**

---

Publicly Accessible Penn Dissertations


---

2021

## Vip Interneuron Cell And Circuit Dysfunction Underlying Dravet Syndrome

Kevin Mitchell Goff  
*University of Pennsylvania*

Follow this and additional works at: <https://repository.upenn.edu/edissertations>

 Part of the [Neuroscience and Neurobiology Commons](#)

---

### Recommended Citation

Goff, Kevin Mitchell, "Vip Interneuron Cell And Circuit Dysfunction Underlying Dravet Syndrome" (2021).  
*Publicly Accessible Penn Dissertations*. 5208.  
<https://repository.upenn.edu/edissertations/5208>

This paper is posted at ScholarlyCommons. <https://repository.upenn.edu/edissertations/5208>  
For more information, please contact [repository@pobox.upenn.edu](mailto:repository@pobox.upenn.edu).

---

# Vip Interneuron Cell And Circuit Dysfunction Underlying Dravet Syndrome

## Abstract

GABAergic inhibitory interneurons of the cerebral cortex expressing vasoactive intestinal peptide (VIP-INS) are rapidly emerging as important regulators of network dynamics and normal circuit development. Several recent studies have also identified VIP-IN dysfunction in models of genetically determined neurodevelopmental disorders (NDDs). In this dissertation, we review the known circuit functions of VIP-INS and how they may relate to accumulating evidence implicating VIP-IN dysfunction in the mechanisms of prominent NDDs. We highlight recurring VIP-IN mediated circuit motifs that are shared across cerebral cortical areas, and how VIP-IN activity can shape sensory input, development, and behavior. Ultimately, we extract a set of themes that inform our understanding of how VIP-INS influence pathogenesis of NDDs. We focus on a particularly enticing disease candidate: Dravet Syndrome, a severe NDD characterized by epilepsy, autism spectrum disorder (ASD), and intellectual disability (ID) caused by loss of function variants in SCN1A which codes for the voltage-gated Na<sup>+</sup> channel  $\alpha$  subunit, Nav1.1. We go on to show that Nav1.1 is expressed in VIP-INS, and loss of a single copy causes VIP-INS to be hypoexcitable in acute brain slices from Scn1a<sup>+/-</sup> mice. Using this same model, we show that this intrinsic hypoexcitability translates to decreased VIP-IN activity and impaired cortical network dynamics in vivo using two-photon calcium imaging. We find that the above results are replicated when using a conditional deletion of Scn1a in VIP-INS. However, these conditional mutants do not have epilepsy like the global model, but do replicate core features of ASD and ID. This dissociates the roles of VIP-IN dysfunction from potential involvement of other cell types in Dravet pathogenesis. Finally, using publicly available single cell RNA sequencing (scRNA-seq) data from the Allen Institute, we also identify several underexplored disease-associated genes that are highly expressed in VIP-INS. We survey these genes and their shared related disease phenotypes that may broadly implicate VIP-INS in ASD and ID rather than epilepsy. We conclude with a discussion of the relevance of cell type-specific investigations to drive the potential development of therapeutics targeting VIP-INS in the age of genomic diagnosis and precision medicine.

## Degree Type

Dissertation

## Degree Name

Doctor of Philosophy (PhD)

## Graduate Group

Neuroscience

## First Advisor

Ethan M. Goldberg

## Keywords

Autism, Circuits, disinhibition, Epilepsy, Interneurons, VIP

## Subject Categories

Neuroscience and Neurobiology

VIP INTERNEURON CELL AND CIRCUIT DYSFUNCTION UNDERLYING DRAVET

SYNDROME

Kevin M. Goff

A DISSERTATION

in

Neuroscience

Presented to the Faculties of the University of Pennsylvania

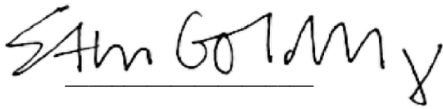
in

Partial Fulfillment of the Requirements for the

Degree of Doctor of Philosophy

2021

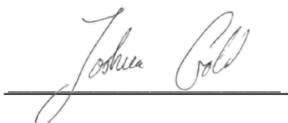
Supervisor of Dissertation



Ethan M. Goldberg, MD PhD

Assistant Professor of Neurology

Graduate Group Chairperson



Joshua Gold, PhD

Professor of Neuroscience

Dissertation Committee

Maria Geffen, PhD

Associate Professor of Otorhinolaryngology

John Dani, PhD

David J. Mahoney Professor of Neurological Sciences

Toshinori Hoshi, PhD

Professor of Physiology

Marc Fuccillo, MD PhD

Assistant Professor of Neuroscience

Peyman Golshani, MD PhD

Professor of Neurology, Brain Research Institute, UCLA

VIP INTERNEURON CELL AND CIRCUIT DYSFUNCTION UNDERLYING DRAVET  
SYNDROME

COPYRIGHT

2021

Kevin Mitchell Goff

*To my wife Lindsay. I love you so much I married you twice.*

*If I have the gift of prophecy and can fathom all mysteries and all knowledge, and if I have a faith that can move mountains, but do not have love, I am nothing.*

- 1 Corinthians 13:2

## ACKNOWLEDGMENT

This work was supported by NIH NINDS F31 NS111803 to K.M.G. and NIH NINDS K08 NS097633 and R01 NS110869 and a Career Award for Medical Scientists from the Burroughs Wellcome Fund to E.M.G. I thank Dr. Jennifer A. Kearney at Northwestern University for the generous gift of *Scn1a*<sup>+/-</sup> mice and Drs. Bernardo Rudy and Robert Machold at NYU for the gift of the VIP/CCK and VIP/CR mice. I thank Dr. Xiaohong Zhang for expert technical assistance. I thank members of the Goldberg Lab, Ala Somarowthu and Evan Jiang, for their help and co-authorship on Chapter 3, and all other members of the Goldberg lab past and present for countless hours of teaching, discussion, and feedback. I thank Ethan for 4 great years as an invaluable mentor and friend.

## ABSTRACT

### VIP INTERNEURON CELL AND CIRCUIT DYSFUNCTION UNDERLYING DRAVET SYNDROME

Kevin M. Goff

Ethan M. Goldberg

GABAergic inhibitory interneurons of the cerebral cortex expressing vasoactive intestinal peptide (VIP-INS) are rapidly emerging as important regulators of network dynamics and normal circuit development. Several recent studies have also identified VIP-IN dysfunction in models of genetically determined neurodevelopmental disorders (NDDs). In this dissertation, we review the known circuit functions of VIP-INS and how they may relate to accumulating evidence implicating VIP-IN dysfunction in the mechanisms of prominent NDDs. We highlight recurring VIP-IN mediated circuit motifs that are shared across cerebral cortical areas, and how VIP-IN activity can shape sensory input, development, and behavior. Ultimately, we extract a set of themes that inform our understanding of how VIP-INS influence pathogenesis of NDDs. We focus on a particularly enticing disease candidate: Dravet Syndrome, a severe NDD characterized by epilepsy, autism spectrum disorder (ASD), and intellectual disability (ID) caused by loss of function variants in *SCN1A* which codes for the voltage-gated Na<sup>+</sup> channel  $\alpha$  subunit, Nav1.1. We go on to show that Nav1.1 is expressed in VIP-INS, and loss of a single copy causes VIP-INS to be hypoexcitable in acute brain slices from *Scn1a*<sup>+/-</sup> mice. Using this same model, we show that this intrinsic hypoexcitability translates to decreased VIP-IN activity and impaired cortical network dynamics *in vivo* using two-photon calcium imaging. We find that the above results are replicated when using a conditional deletion of *Scn1a* in VIP-INS. However, these conditional mutants do not

have epilepsy like the global model, but do replicate core features of ASD and ID. This dissociates the roles of VIP-IN dysfunction from potential involvement of other cell types in Dravet pathogenesis. Finally, using publicly available single cell RNA sequencing (scRNA-seq) data from the Allen Institute, we also identify several underexplored disease-associated genes that are highly expressed in VIP-INs. We survey these genes and their shared related disease phenotypes that may broadly implicate VIP-INs in ASD and ID rather than epilepsy. We conclude with a discussion of the relevance of cell type-specific investigations to drive the potential development of therapeutics targeting VIP-INs in the age of genomic diagnosis and precision medicine.



## TABLE OF CONTENTS

<b>ACKNOWLEDGMENT</b> .....	<b>IV</b>
<b>ABSTRACT</b> .....	<b>V</b>
<b>LIST OF TABLES</b> .....	<b>IX</b>
<b>LIST OF ILLUSTRATIONS</b> .....	<b>X</b>
<b>CHAPTER 1: A ROLE FOR VIP INTERNEURONS IN NEURODEVELOPMENTAL DISORDERS</b> .....	<b>1</b>
<b>INTRODUCTION</b> .....	<b>1</b>
<b>CIRCUIT FUNCTIONS OF VIP-INS</b> .....	<b>2</b>
<b>VIP-INS SHAPE RESPONSE TO SENSORY INPUTS</b> .....	<b>5</b>
<b>VIP-INS INFLUENCE ATTENTION AND PERFORMANCE ACROSS MULTIPLE LEARNING PARADIGMS</b> .....	<b>7</b>
<b>VIP-INS ARE REQUIRED FOR NORMAL CIRCUIT DEVELOPMENT</b> .....	<b>8</b>
<b>VIP-IN DYSFUNCTION IS IMPLICATED IN A PROMINENT NDD</b> .....	<b>9</b>
<b>VIP-INS MAY BE INVOLVED IN BROADER NEUROPSYCHIATRIC DISORDERS</b> .....	<b>10</b>
<b>VIP-IN FUNCTION IN THE CONTEXT OF DRAVET SYNDROME</b> .....	<b>10</b>
<b>REFERENCES</b> .....	<b>14</b>
<b>CHAPTER 2: VIP INTERNEURONS ARE IMPAIRED IN A MOUSE MODEL OF DRAVET SYNDROME</b> .....	<b>25</b>
<b>ABSTRACT</b> .....	<b>25</b>
<b>INTRODUCTION</b> .....	<b>26</b>
<b>RESULTS</b> .....	<b>29</b>
<b>DISCUSSION</b> .....	<b>49</b>
<b>MATERIALS AND METHODS</b> .....	<b>54</b>
<b>SUPPLEMENTAL FIGURES</b> .....	<b>72</b>
<b>REFERENCES</b> .....	<b>90</b>

<b>CHAPTER 3: VIP INTERNEURON DYSFUNCTION UNDERLIES ABNORMAL NEOCORTICAL STATE TRANSITIONS AND BEHAVIOR IN A SEVERE NEURODEVELOPMENTAL DISORDER.....</b>	<b>98</b>
ABSTRACT .....	98
INTRODUCTION.....	100
RESULTS .....	104
DISCUSSION.....	116
MATERIALS AND METHODS .....	121
SUPPLEMENTAL FIGURES.....	139
REFERENCES.....	149
<b>CHAPTER 4: EXPLORING VIP-INS AS A THERAPEUTIC TARGET IN DRAVET SYNDROME AND BEYOND .....</b>	<b>159</b>
SEARCHING FOR DISEASE GENES IMPORTANT FOR VIP-IN FUNCTION.....	160
POINTS OF CONVERGENCE BETWEEN EXPERIMENTAL MODELS OF ASD.....	166
TOWARDS CELL TYPE-SPECIFIC THERAPIES .....	169
REFERENCES.....	173

## LIST OF TABLES

TABLE 2.1. KEY RESOURCES .....	54
TABLE 2.2. PROPERTIES OF VIP-INS FROM <i>SCN1A</i> <sup>+/-</sup> AND WT LITTERMATES .....	79
TABLE 3.1 KEY RESOURCES .....	121
TABLE 3.2. DATA AND NETWORK TRAINING PARAMETERS USED IN DLC POSE ESTIMATION. ....	148
TABLE 4.1. CELL TYPE SPECIFIC EXPRESSION OF NDD GENES .....	161

## LIST OF ILLUSTRATIONS

FIGURE 1.1. CIRCUIT FUNCTIONS OF VIP-INS IN NDDS.....	4
FIGURE 2.1. VIP-INS EXPRESS NAV1.1 AND ARE HYPOEXCITABLE IN <i>SCN1A</i> <sup>+/-</sup> MICE	31
FIGURE 2.2. TWO VIP-IN FIRING PATTERNS REVEALED WITH LONG DEPOLARIZATION	34
FIGURE 2.3. IS VIP-INS ARE PREFERENTIALLY IMPAIRED IN <i>SCN1A</i> <sup>+/-</sup> MICE .....	35
FIGURE 2.4. HM1A APPLICATION MODULATES NA <sup>+</sup> CHANNELS CONTAINING NAV1.1 SUBUNITS IN VIP-INS AND RECOVERS IS VIP-IN HYPOFUNCTION IN <i>SCN1A</i> <sup>+/-</sup> MICE ..	39
FIGURE 2.5. INTERSECTIONAL EXPRESSION OF CR AND CCK LABELS ANATOMICAL SUBSETS OF VIP-INS BUT DOES NOT CORRELATE WITH IS VS. CA FIRING PATTERNS. .....	42
FIGURE 2.6. KCNQ CHANNELS REGULATE VIP-IN FIRING PATTERNS.....	43
FIGURE 2.7. CHOLINERGIC MODULATION INDUCES SWITCHING FROM IRREGULAR TO CONTINUOUS FIRING IN IS VIP-INS .....	45
FIGURE 2.8. SINGLE COMPARTMENT MODEL OF A VIP-IN ILLUSTRATES THE INTERACTION BETWEEN M-CURRENT AND NA <sup>+</sup> CURRENT .....	48
FIGURE 2.S1. <i>SCN1A</i> EXPRESSION IN VIP-INS .....	72
FIGURE 2.S2. LOCALIZATION OF NAV1.1 ON VIP-IN AXONS. ....	73
FIGURE 2.S4. IS VIP-IN FIRING PATTERNS ARE ROBUST TO A VARIETY OF STIMULATION METHODS .....	76
FIGURE 2.S5. A SUBSET OF BOTH CA AND IS VIP-INS SHOW BURSTING AT RHEOBASE .....	78
FIGURE 2.S6. IS VIP-IN DEFICITS IN <i>SCN1A</i> <sup>+/-</sup> MICE ARE CONSISTENT ACROSS DEVELOPMENT.....	80

FIGURE 2.S7. IS VIP-IN DEFICITS IN <i>SCN1A</i> <sup>+/-</sup> MICE ARE CONSISTENT ACROSS CORTICAL AREAS.....	82
FIGURE 2.S8. EFFECTS OF LOW CONCENTRATION HM1A ON IS VIP-IN FIRING.....	83
FIGURE 2.S9. KCNQ5 IS SELECTIVELY EXPRESSED IN A SUBSET OF VIP-INS .....	84
FIGURE 2.S10. KCNQ5 BUT NOT KCNQ3 IS EXPRESSED IN VIP-INS .....	86
FIGURE 2.S11. LINOPIRDINE HAS NO EFFECT ON CA VIP-IN EXCITABILITY .....	87
FIGURE 2.S12. MUSCARINIC BUT NOT NICOTINIC RECEPTOR ACTIVATION IS SUFFICIENT TO INDUCE IRREGULAR-TONIC SWITCHING IN IS VIP-INS .....	88
FIGURE 3.1. ALTERED <i>IN VIVO</i> VIP-IN ACTIVITY AND CSTS IN <i>SCN1A</i> <sup>+/-</sup> MICE. ....	105
FIGURE 3.2. EFFECT OF CHOLINERGIC MODULATION ON VIP-IN CELLULAR EXCITABILITY AND SODIUM CURRENT.....	107
FIGURE 3.3. OPTOGENETIC ACTIVATION OF VIP-INS DURING LOCOMOTION BOUTS RESTORES ASPECTS OF NORMAL CORTICAL DYNAMICS IN <i>SCN1A</i> <sup>+/-</sup> MICE.....	107
FIGURE 3.4. VIP-IN SPECIFIC LOSS OF <i>SCN1A</i> RECAPITULATES THE CELLULAR DEFICITS OBSERVED IN VIP-INS IN GLOBAL <i>SCN1A</i> <sup>+/-</sup> MICE.....	111
FIGURE 3.5. LOSS OF <i>SCN1A</i> IN VIP-INS PRODUCES CIRCUIT DEFICITS <i>IN VIVO</i> THAT ARE EXACERBATED BY MUSCARINIC ACTIVATION. ....	113
FIGURE 3.6. LOSS OF <i>SCN1A</i> IN VIP-INS REPLICATES CORE COGNITIVE IMPAIRMENTS AND ASD ENDOPHENOTYPES OF THE GLOBAL <i>SCN1A</i> <sup>+/-</sup> DS MODEL.....	115
FIGURE 3.S1: MARKERS OF BEHAVIORAL STATE CHANGES ARE CONSISTENT ACROSS GENOTYPES DURING 2P IMAGING SESSIONS. ....	139
FIGURE 3.S2: NEUROPIIL BACKGROUND FLUORESCENCE CORRECTION. ....	140
FIGURE 3.S3: ISOLATING DEFINITIVE PYRAMIDAL NEURONS FROM TDT- NON-VIP NEURONS.....	141
FIGURE 3.S4: VIP-IN TO NETWORK CORRELATION IS REDUCED IN <i>SCN1A</i> <sup>+/-</sup> MICE..	143

<b>FIGURE 3.S5: EVENT DECONVOLUTION FROM DF/F0.....</b>	<b>144</b>
<b>FIGURE 3.S6: CARBACHOL HAS A SIMILAR EFFECT ON VIP-INS WITH DIFFERING FIRING PATTERNS.....</b>	<b>145</b>
<b>FIGURE 3.S7: DIVERSE NETWORK RESPONSES IN RESPONSE TO OPTOGENETICALLY STIMULATION OF VIP-INS.....</b>	<b>146</b>
<b>FIGURE 3.S8: COMPARISON OF DLC BASED PROXIMITY SCORING AND BLINDED MANUAL SCORING OF NOR INTERACTIONS. ....</b>	<b>147</b>
<b>FIGURE 4.1. RELATIVE EXPRESSION OF NDD RELATED DISEASE GENES IN VIP-INS .</b>	<b>164</b>
<b>FIGURE 4.2. SEPARATION OF IN SUBCLASSES BASED ON NDD DIAGNOSTIC PANEL GENES.....</b>	<b>169</b>

# **CHAPTER 1: A Role for VIP Interneurons in Neurodevelopmental Disorders**

## **Introduction**

While comprising only a fraction of the total cells in the cerebral cortex, interneurons (INs) have garnered significant attention due to their complex and dynamic roles in shaping network activity and behavior. Furthermore, many neurological disorders may involve impaired IN function (Hattori et al., 2017). IN dysfunction is often framed in the context of excitation/inhibition (E/I) imbalance, a useful simplification. However, INs are embedded within myriad complex repeating circuit motifs in the cerebral cortex, including feedforward, feedback, and disinhibitory interconnectivity (Kepecs and Fishell, 2014). As a result, the three largest subclasses of INs, which express parvalbumin, somatostatin, or vasoactive intestinal peptide (PV, SST, and VIP-INs) (Rudy et al., 2011), take part in diverse circuit functions, from regulation of neuromodulatory influences on neocortex to spike timing and synchronization. INs also serve as mediators of normal circuit development by regulating critical period plasticity and shaping the formation of sensory maps (Hattori et al., 2017). There is strong interest in identifying the role of IN subclasses in genetically determined neurodevelopmental disorders (NDDs). VIP-INs in particular have unique circuit functions which position them as a potentially important locus of pathology in NDDs. While we have a blossoming understanding of how VIP-INs influence normal cortical circuit activity and development, the contributions of VIP-INs to specific NDDs are just beginning to be explored.

Here, we examine the circuit impact of VIP-INs, extracting recurrent themes to suggest how VIP-IN dysfunction might contribute to NDDs (Fig. 1). We summarize early evidence for VIP-IN involvement in Dravet syndrome (DS), a severe NDD caused by

loss of function mutations in *SCN1A*, and more broadly across epilepsy and autism spectrum disorder (ASD). We then present original research demonstrating that VIP-IN excitability depends upon expression of the voltage-gated sodium ( $\text{Na}^+$ ) channel subunit Nav1.1, which is coded by *Scn1a*, and that VIP-INs are dysfunctional in a mouse model of DS with heterozygous loss of *Scn1a*. This dysfunction causes abnormal activity in the neocortex and underlies ASD related endophenotypes in this model. Finally, using single cell RNA sequencing (scRNA-seq) data available from the Allen Institute (Yao et al., 2021), we highlight several prominent disease genes that are highly expressed in VIP-INs. Thus, we explore avenues for better understanding VIP-IN function while also implicating VIP-IN dysfunction in NDD pathogenesis and more broadly in ASD. We conclude by discussing how cell-type specific manipulations targeted at VIP-INs may drive the development of novel therapeutic approaches.

## **Circuit functions of VIP-INs**

The existence of VIP-expressing as well as IN-targeting cells in neocortex and hippocampus has been known for 30-40 years (Acsády et al., 1996; Dávid et al., 2007; Hájos et al., 1996; Porter et al., 1998, 1999). Comprising only 10% of cerebral cortex INs (Rudy et al., 2011), understanding of VIP-IN function has been accelerated by the availability of genetic tools to target discrete IN subpopulations (Dimidschstein et al., 2016; He et al., 2016; Taniguchi et al., 2011). Although it is the case that all INs target other INs to some extent, several studies using VIP-Cre mice to record, image, and manipulate VIP-INs indicate that they preferentially inhibit other INs, increase activity of local pyramidal neurons, and are functionally disinhibitory (Fu et al., 2014; Lee et al., 2013; Pfeffer et al., 2013; Pi et al., 2013). Nevertheless, VIP-INs do form direct inhibitory synapses onto local pyramidal neurons, although the functional significance of these



direct connections is not well understood (Zhou et al., 2017). There is considerable heterogeneity within VIP-INs including non-overlapping populations marked by the expression of cholecystokinin and calretinin, as well as a subset of VIP-INs that corelease acetylcholine (Gouwens et al., 2019, 2020; Granger et al., 2020; He et al., 2016; Obermayer et al., 2019; Paul et al., 2017; Prönneke et al., 2015; Tasic et al., 2016). There is some evidence that VIP itself can shape cerebral blood flow and neuronal excitability, but this has not been specifically tied to VIP-IN activity (Cunha-Reis and Caulino-Rocha, 2020; Cunha-Reis et al., 2005; Yang et al., 2010). It remains largely unknown how this within-type diversity relates to VIP-IN circuit function.

Despite unresolved aspects of diversity within the VIP-IN subclass, there remain several core features of circuits containing VIP-INs that are remarkably well conserved across brain regions (Guet-McCreight et al., 2020). For example, VIP-INs are uniformly recruited by cholinergic neuromodulation (Askew et al., 2019; Fu et al., 2014; Porter et al., 1999; Prönneke et al., 2020; Reimer et al., 2014), and preferentially target SST-INs (Fu et al., 2014; Krabbe et al., 2019; Lee et al., 2013; Muñoz et al., 2017; Pfeffer et al., 2013; Tyan et al., 2014; Walker et al., 2016). Taken together, this means that VIP-INs disinhibit the dendrite-targeted GABAergic input provided by SST-INs in brain states characterized by increased cholinergic tone. These occur during active behaviors like running and whisking in rodents, and are also marked by enhanced hippocampal theta rhythm (Fu et al., 2014; Gasselin et al., 2021; Jackson et al., 2016; Khan et al., 2018; Luo et al., 2020; McGinley et al., 2015; Reimer et al., 2014; Turi et al., 2019). VIP-INs express nicotinic (Askew et al., 2019; Paul et al., 2017; Porter et al., 1999; Tasic et al., 2016) and muscarinic (Goff and Goldberg, 2019) acetylcholine receptors, as well as receptors for other neuromodulators including the ionotropic serotonin receptor 5-HT<sub>3R</sub>

(Lee et al., 2010; Prönneke et al., 2020). Beyond direct depolarization by acetylcholine, a diverse repertoire of metabotropic receptors shapes the intrinsic excitability of VIP-INs through regulating ionic conductances such as M-type potassium current (Goff and Goldberg, 2019) and T-type calcium current (Prönneke et al., 2020). VIP-INs also integrate long-range cortico-cortical input (Lee et al., 2013; Zhang et al., 2014). Overall, this positions VIP-INs as a key component of top-down neuromodulation in the neocortex, defining the cellular and circuit basis for how VIP-INs shape cortical processing.

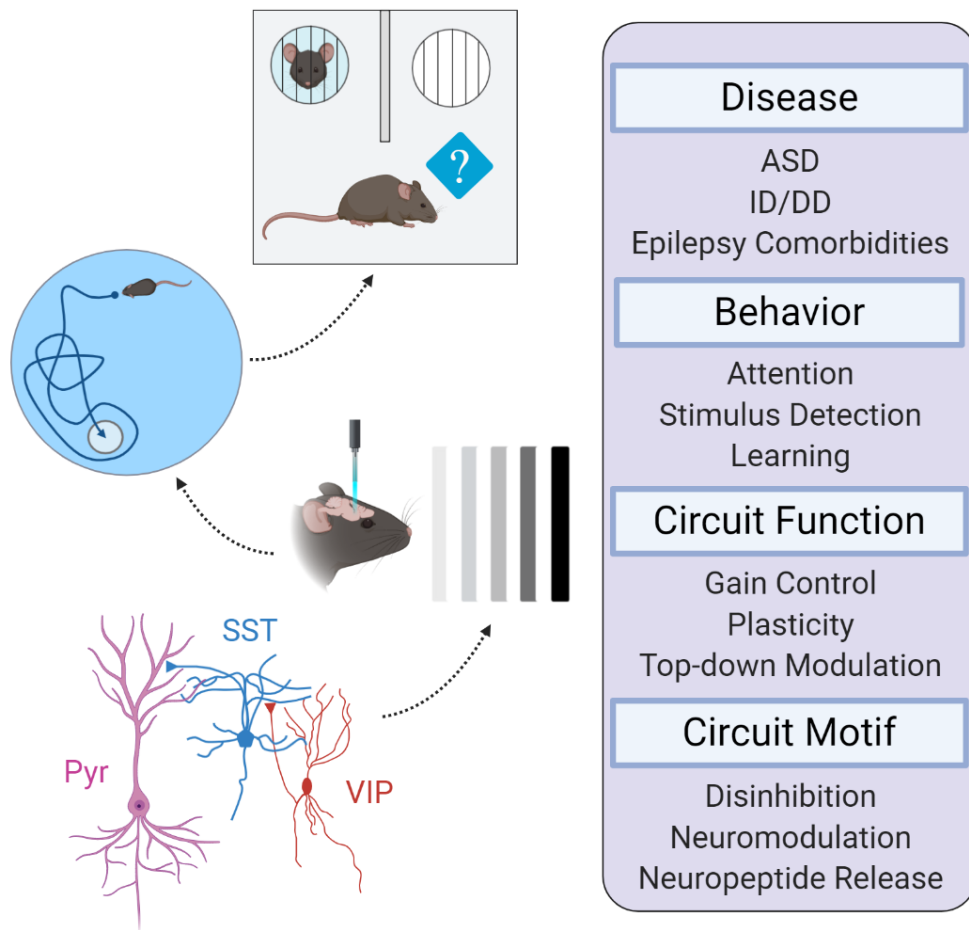


**Figure 1. Circuit Functions of VIP-INs in NDDs.** Diagrammatic representation of VIP-IN regulated circuits and their impact on biology and disease. VIP-INs are components

of several repetitive circuit motifs in the cerebral cortex, including a prominent disinhibitory circuit that is conserved across many brain areas. The activity of VIP-INs not only influences network dynamics, but also the development of normal neural circuits. This shapes behaviours in several important ways, including learning, memory, and attention. Finally, impaired VIP-IN function caused by mutations in certain disease genes may cause abnormal circuit function and behaviour that underlies NDD endophenotypes like autism spectrum disorder (ASD), intellectual disability (ID), and developmental delay (DD). Figure created with BioRender.com.

---

## **VIP-INs shape response to sensory inputs**

VIP-INs play a particularly important role in shaping neocortical response to sensory inputs. The canonical VIP-IN disinhibitory circuit is found in essentially all primary sensory areas in rodents. In visual cortex (V1), VIP-IN recruitment during active behaviors increases the gain of layer 2/3 pyramidal neurons without affecting their orientation selectivity (Fu et al., 2014; Reimer et al., 2014). Correspondingly, optogenetic stimulation of VIP-INs during a visual contrast detection task improves performance, while coactivating either SST or PV-INs reduces the ability of the mouse to detect lower contrasts (Cone et al., 2019). Long range projections from the cingulate cortex activate this circuit, providing another mechanism for top down modulation of early visual processing analogous to the frontal eye fields in primates (Zhang et al., 2014). This pathway drives narrow bands of disinhibition within visual columns and enhances both visual responses and performance on a discrimination task.

VIP-INs in auditory cortex (A1) are strongly activated by cholinergic stimulation (Askew et al., 2019), but the exact relationship between locomotion and VIP-IN-mediated disinhibition may be different than in V1 (Bigelow et al., 2019). Nevertheless, direct VIP-IN activation disinhibits a subset of tone-responsive neurons, resulting in an increase in the gain of the corresponding tuning curves (Pi et al., 2013). Cortico-cortical

motor signals arising from whisking act in parallel to ascending cholinergic neuromodulation to drive VIP-IN activity in barrel cortex (S1) (Lee et al., 2013). Interestingly, whisking causes inhibition of a subset of Martinotti-type SST-INs via VIP-INs, yet other SST-INs are actually recruited by muscarinic acetylcholine receptor activation (Muñoz et al., 2017). VIP-INs are clearly able to increase the gain of sensory responses in primary sensory areas, but there may be meaningful region-specific differences in what is otherwise a highly conserved circuit motif.

While top-down disinhibition through VIP-INs enhances the gain of sensory signals on a trial-by-trial basis, VIP-INs also promote plasticity and themselves exhibit plastic responses, which could influence developmental processes. Indeed, theoretical work suggests that disinhibition may be a mechanism for associative learning in the neocortex (Wilmes and Clopath, 2019). Supporting this hypothesis, inactivation, or activation, of VIP-INs in V1 can impair or enhance plasticity after monocular deprivation, respectively (Fu et al., 2015). While the response of V1 VIP-INs to simple visual stimuli like drifting gratings is variable (Millman et al., 2020; de Vries et al., 2020), VIP-INs are suppressed by familiar natural images but strongly activated by novel images during a discrimination task (Garrett et al., 2020). Moreover, VIP-INs show strong ramping activity during the omission of familiar images in the same task, suggesting that VIP-IN activity may enhance the cortical representation of salient sensory events such as the presentation of novel stimuli or the absence of expected stimuli. In A1, VIP-INs are recruited by signals reinforcing both reward and avoidance (Pi et al., 2013), further suggesting that VIP-INs are involved in encoding the salience of input features across sensory neocortex.

## **VIP-INs influence attention and performance across multiple learning paradigms**

In addition to shaping sensory processing, VIP-INs influence learning, attention, and plasticity in distributed brain regions. VIP-INs in the basolateral amygdala (BLA) are recruited by aversive foot shocks in a fear conditioning paradigm, and VIP-IN activity is enhanced when the shock is unexpected, or is stronger than expected (Krabbe et al., 2019). Furthermore, blocking VIP-IN activity during the unconditioned foot shock stimulus reduces projection neuron activity and prevents normal fear conditioning. In area CA1 of the hippocampus, VIP-INs are also modulated by locomotion (Luo et al., 2020; Turi et al., 2019), but respond strongly to rewards during spatial learning tasks (Turi et al., 2019). Blocking VIP-IN activity abolishes the remapping of place cells in CA1 around the location of a rewarding stimulus and negatively impacts the performance of mice learning the task, while direct activation of VIP-INs concurrent with the reward improves performance.

Finally, direct activation of VIP-INs in the prefrontal cortex (PFC) improves performance on a delayed forced choice task, but activation of PV, SST, or pyramidal neurons during the task all impairs performance (Kamigaki and Dan, 2017). Some VIP-INs also show ramping activity during the delay between the cue and test response, and their ability to increase both correct hits and correct rejections supports the conclusion that VIP-IN activation improves attention to stimulus presentation during this working memory task. Similarly, VIP-INs in the PFC are recruited when a mouse is in the open arm of an elevated plus maze, and inhibiting VIP-IN activity increases exploration of the open arm (Lee et al., 2019). Thus, VIP-INs in PFC, amygdala, and hippocampus

contribute to distinct learning modalities and respond to a variety of salient signals of both positive and negative valence.

## **VIP-INs are required for normal circuit development**

Overall, VIP-INs have emerged as important components of the cortical circuits underlying attention and arousal, particularly by attaching salience to features of sensory input. Through these functions, VIP-IN activity also has a profound impact on multiple mechanisms of cortical plasticity and forms of learning. The work described above defines roles for VIP-INs in cerebral cortical circuit operations, but it is now known that proper VIP-IN function is also required for normal development of these same circuits. Conditional VIP-IN deletion of *ErBb4*, a receptor important for normal migration and synapse formation, results in profound network abnormalities in V1 (Batista-Brito et al., 2017). This includes disruption of VIP-IN functions such as state transitions and gain modulation during locomotion, but this perturbation also affects basic network features including LFP-spike phase locking and orientation selectivity of layer II/III pyramidal neurons in V1. Interestingly, pyramidal neuron visual responses in the conditional *ErBb4* knockout mice closely resemble WT responses at post-natal day (P) 15-18, but these responses progressively degrade as the mice age, further supporting a dynamic intersection between VIP-IN function in established circuits and influence over developmental processes. Critically, these circuit-level deficits cause impaired performance during a contrast discrimination task, suggesting that VIP-IN dysfunction gives rise to pathological brain-state regulation that may lead to abnormal behavior.

## VIP-IN dysfunction is implicated in a prominent NDD

Many NDDs are characterized by behavioral abnormalities and network activity akin to features that we now know rely on VIP-IN activity. This positions VIP-INS as a potentially critical yet nearly unexplored cellular locus of circuit dysfunction in NDDs. Mouse models of prominent human NDDs combined with genetic targeting of VIP-INS are now being used to investigate the role of VIP-INS in disease. Rett syndrome is an early-onset NDD characterized by seizures, intellectual disability (ID), features of ASD, and repetitive stereotypical hand movements (Chahrour and Zoghbi, 2007; Hagberg et al., 1983). Most cases are found in girls and are caused by missense variants or deletions in the gene encoding methyl-CpG binding protein 2 (*MECP2*) located on the X chromosome. Hemizygous male mice lacking a copy of *Mecp2* show many features consistent with Rett syndrome (Chen et al., 2001; Guy et al., 2001), and, while *Mecp2* is expressed in essentially all neurons, conditional deletion of *Mecp2* in cerebral-cortical INs replicates many of the core features of the global model (Mossner et al., 2020). Interestingly, mice also show electrophysiological and behavioral deficits when deletion of *Mecp2* is further restricted to VIP-INS (Mossner et al., 2020). In particular, cortical state transitions at the onset of locomotion are diminished, and, while there is no increase in seizures or mortality, the mice show abnormal patterns of social behavior including a failure to display preference for a novel mouse versus an empty chamber. This phenotype is characteristic of many mouse models of ASD (Antoine et al., 2019; Tatsukawa et al., 2018), and it is notable that the features of ASD can be dissociated from the seizure phenotype in this Rett model by selective manipulation of VIP-INS. PV or SST-IN specific deletions of *Mecp2* did not cause the same social deficits. Therefore,

the primarily disinhibitory role of VIP-INs may underlie some aspects of ASD and/or ID in Rett syndrome without influencing seizure susceptibility.

### **VIP-INs may be involved in broader neuropsychiatric disorders**

Rett syndrome is an interesting early example of VIP-IN dysfunction in NDDs. However, there is increasing consensus that many neuropsychiatric disorders have 'developmental' origins, including prominent clinical entities like major depression, bipolar disorder, schizophrenia, and substance abuse/addiction (Owen and O'Donovan, 2017). In mice, expression of an  $\alpha 5$  nicotinic receptor (*CHRNA5*) human variant associated with nicotine abuse drastically decreases spontaneous VIP-IN activity *in vivo* with a corresponding increase in SST-IN activity (Koukouli et al., 2017). This also causes decreased PFC network activity, and thus may underlie the hypofrontality seen in patients with this gene variant. Interestingly, *Chrna5* variant mice also have social deficits – a recurring theme in all three of the above examples. At a mechanistic level, some VIP-INs in the anterior cingulate cortex respond directly to social stimuli (Johnson et al., 2020), but it remains unknown how VIP-INs influence social behavior. This represents exciting new territory for basic research into VIP-IN function. The themes shared between the above results compared to the Rett syndrome model point to a broader role for VIP-INs in NDDs, with particular reference to features of ASD and ID.

### **VIP-IN function in the context of Dravet Syndrome**

One of the most prominent NDDs that shares features with the diseases and models mentioned above is Dravet Syndrome (DS), a severe NDD that is characterized by treatment-resistant epilepsy, ASD, moderate to severe ID, and a high risk of sudden unexpected death (SUDEP) (Dravet, 2011; Li et al., 2011; Villas et al., 2017). DS is



caused by pathogenic heterozygous loss of function variants in *SCN1A* (Claes et al., 2001), the gene encoding the voltage-gated sodium (Na<sup>+</sup>) channel  $\alpha$  subunit Nav1.1. Initially, this presented a paradoxical genetic locus for DS: How does a decrease in expression of voltage-gated Na<sup>+</sup> channels, which drive the intrinsic excitability of neurons, lead to hyperexcitability and epilepsy? Data from human stem cell derived neurons, as well as the development of an *Scn1a*<sup>+/-</sup> mouse model helped identify that Nav1.1 is expressed in nearly all INs and is an important determinant of intrinsic excitability of these cells (Ogiwara et al., 2007; Sun et al., 2016; Tai et al., 2014). This led to the 'interneuron hypothesis' of DS, positing that INs are selectively impaired while glutamatergic principal neuron function is spared, which alters the excitatory/inhibitory (E/I) balance and is epileptogenic. While there is some evidence for small subsets of glutamatergic neurons expressing Nav1.1, both the global *Scn1a*<sup>+/-</sup> model and IN specific deletion replicate core features of the human disease (Cheah et al., 2012; Oakley et al., 2009; Richards et al., 2018; Rubinstein et al., 2015), while deletion of *Scn1a* from telencephalic glutamatergic neurons appears to protect against epilepsy (Ogiwara et al., 2013). However, the cellular and circuit bases of DS remains unknown and existing knowledge has yet to lead to cure or disease-modifying treatments. To this end, recent work has focused on the role of particular IN subclasses in this severe disease.

PV, and SST-INs from multiple cortical regions exhibit impaired action potential generation and repetitive firing in *Scn1a*<sup>+/-</sup> mice, although these abnormalities display different developmental time courses (Almog et al., 2021; Favero et al., 2018; Goff and Goldberg, 2019; Rubinstein et al., 2015; De Stasi et al., 2016; Tai et al., 2014). For instance, neocortical PV-INs are most dysfunctional around P16-P21, corresponding to

the onset of Nav1.1 expression when the mice are most prone to seizures and SUDEP, but regain normal excitability by young adulthood (P50+) (Favero et al., 2018; Kaneko et al., 2021). CA1 horizontal stratum-oriens INs (most likely expressing SST) also show a narrow window of severe impairment around P21-24 and partially regain their function in adult mice (Almog et al., 2021). While it is not clear how and why some IN subpopulations recover function in *Scn1a*<sup>+/-</sup> mice – perhaps through homeostatic upregulation of other Nav1.X channel subunits – there remains an interesting correlation between cellular function and DS seizure and behavior phenotypes. *Scn1a*<sup>+/-</sup> mice that survive past an early developmental window tend to have a much lower rate of spontaneous seizures and death. However, they continue to demonstrate abnormal behaviors consistent with ASD and ID. Overall, these findings closely mirror what is known about the human disease: seizure frequency typically decreases with age yet ID and ASD are durable and longstanding (Genton et al., 2011). Interestingly, some of these behaviors like sociability and fear conditioned memory are reversibly rescued by low dose GABA agonists during adulthood in *Scn1a*<sup>+/-</sup> mice (Han et al., 2012). This suggests that IN dysfunction remains in adult *Scn1a*<sup>+/-</sup> mice, necessitating the investigation of other IN subtypes like VIP-INs.

While VIP-INs were initially thought to only express Nav1.2 (Yamagata et al., 2017), Nav1.1 is expressed at the mRNA level (Goff and Goldberg, 2019; Gouwens et al., 2018; Yao et al., 2021). Additionally, given their role in plasticity, spatial memory, stimulus processing, and sociability, we hypothesize that VIP-IN dysfunction may be involved in the ASD and ID phenotypes of DS. In this series of work, we set out to investigate the role of VIP-INs in DS by answering the following questions: 1) How is the intrinsic excitability of VIP-INs affected by the loss of Nav1.1? 2) Does this translate to *in vivo* disinhibitory circuit dysfunction? 3) Are the ASD related behaviours found in DS

models caused by VIP-IN specific dysfunction? Ultimately, the goal of this work is to identify VIP-INS as a novel disease locus in DS, and if they represent a potential therapeutic target for ameliorating the core ASD-related aspects of this disease. Additionally, we explore the shared characteristics between DS and other NDDs to form a structured outlook on how VIP-INS may impact ASD, while other IN populations may underlie epilepsy.

## References

- Acsády, L., Görcs, T.J., and Freund, T.F. (1996). Different populations of vasoactive intestinal polypeptide-immunoreactive interneurons are specialized to control pyramidal cells or interneurons in the hippocampus. *Neuroscience* 73, 317–334.
- Almog, Y., Fadila, S., Brusel, M., Mavashov, A., Anderson, K., and Rubinstein, M. (2021). Developmental alterations in firing properties of hippocampal CA1 inhibitory and excitatory neurons in a mouse model of Dravet syndrome. *Neurobiol. Dis.* 148, 105209.
- Antoine, M.W., Langberg, T., Schnepel, P., and Feldman, D.E. (2019). Increased Excitation-Inhibition Ratio Stabilizes Synapse and Circuit Excitability in Four Autism Mouse Models. *Neuron* 101, 648-661.e4.
- Askew, C.E., Lopez, A.J., Wood, M.A., and Metherate, R. (2019). Nicotine excites VIP interneurons to disinhibit pyramidal neurons in auditory cortex. *Synapse* 73, 1–12.
- Batista-Brito, R., Vinck, M., Ferguson, K.A., Chang, J.T., Laubender, D., Lur, G., Mossner, J.M., Hernandez, V.G., Ramakrishnan, C., Deisseroth, K., et al. (2017). Developmental Dysfunction of VIP Interneurons Impairs Cortical Circuits. *Neuron* 95, 884-895.e9.
- Bigelow, J., Morrill, R.J., Dekloe, J., and Hasenstaub, A.R. (2019). Movement and VIP interneuron activation differentially modulate encoding in mouse auditory cortex. *ENeuro* 6.
- Chahrour, M., and Zoghbi, H.Y. (2007). The Story of Rett Syndrome: From Clinic to Neurobiology. *Neuron* 56, 422–437.
- Cheah, C.S., Yu, F.H., Westenbroek, R.E., Kalume, F.K., Oakley, J.C., Potter, G.B., Rubenstein, J.L., and Catterall, W.A. (2012). Specific deletion of NaV1.1 sodium channels in inhibitory interneurons causes seizures and premature death in a mouse

model of Dravet syndrome. *Proc. Natl. Acad. Sci. U. S. A.* *109*, 14646–14651.

Chen, R.Z., Akbarian, S., Tudor, M., and Jaenisch, R. (2001). Deficiency of methyl-CpG binding protein-2 in CNS neurons results in a Rett-like phenotype in mice. *Nat. Genet.* *27*, 327–331.

Claes, L., Del-Favero, J., Ceulemans, B., Lagae, L., Van Broeckhoven, C., and De Jonghe, P. (2001). De novo mutations in the sodium-channel gene *SCN1A* cause severe myoclonic epilepsy of infancy. *Am. J. Hum. Genet.* *68*, 1327–1332.

Cone, J.J., Scantlen, M.D., Histed, M.H., and Maunsell, J.H.R. (2019). Different inhibitory interneuron cell classes make distinct contributions to visual contrast perception. *ENeuro* *6*, 1–12.

Cunha-Reis, D., and Caulino-Rocha, A. (2020). VIP Modulation of Hippocampal Synaptic Plasticity: A Role for VIP Receptors as Therapeutic Targets in Cognitive Decline and Mesial Temporal Lobe Epilepsy. *Front. Cell. Neurosci.* *14*, 1–9.

Cunha-Reis, D., Ribeiro, J.A., and Sebastião, A.M. (2005). VIP enhances synaptic transmission to hippocampal CA1 pyramidal cells through activation of both VPAC1 and VPAC2 receptors. *Brain Res.* *1049*, 52–60.

Dávid, C., Schleicher, A., Zuschratter, W., and Staiger, J.F. (2007). The innervation of parvalbumin-containing interneurons by VIP-immunopositive interneurons in the primary somatosensory cortex of the adult rat. *Eur. J. Neurosci.* *25*, 2329–2340.

Dimidschstein, J., Chen, Q., Tremblay, R., Rogers, S.L., Saldi, G.-A., Guo, L., Xu, Q., Liu, R., Lu, C., Chu, J., et al. (2016). A viral strategy for targeting and manipulating interneurons across vertebrate species. *Nat. Neurosci.* *19*, 1743–1749.

Dravet, C. (2011). Dravet syndrome history. *Dev. Med. Child Neurol.* *53*, 1–6.

Favero, M., Sotuyo, N.P., Lopez, E., Kearney, J.A., and Goldberg, E.M. (2018). A Transient Developmental Window of Fast-Spiking Interneuron Dysfunction in a Mouse

Model of Dravet Syndrome. *J. Neurosci.* 38, 7912–7927.

Fu, Y., Tucciarone, J.M., Espinosa, J.S., Sheng, N., Darcy, D.P., Nicoll, R.A., Huang, Z.J., and Stryker, M.P. (2014). A Cortical Circuit for Gain Control by Behavioral State. *Cell* 156, 1139–1152.

Fu, Y., Kaneko, M., Tang, Y., Alvarez-Buylla, A., and Stryker, M.P. (2015). A cortical disinhibitory circuit for enhancing adult plasticity. *Elife* 2015, 1–12.

Garrett, M., Manavi, S., Roll, K., Ollerenshaw, D.R., Groblewski, P.A., Ponvert, N.D., Kiggins, J.T., Casal, L., Mace, K., Williford, A., et al. (2020). Experience shapes activity dynamics and stimulus coding of VIP inhibitory cells. *Elife* 9, 1–25.

Gasselin, C., Hohl, B., Vernet, A., Crochet, S., and Petersen, C.C.H. (2021). Cell-type-specific nicotinic input disinhibits mouse barrel cortex during active sensing. *Neuron* 109, 778-787.e3.

Genton, P., Velizarova, R., and Dravet, C. (2011). Dravet syndrome: The long-term outcome. *Epilepsia* 52, 44–49.

Goff, K.M., and Goldberg, E.M. (2019). Vasoactive intestinal peptide-expressing interneurons are impaired in a mouse model of dravet syndrome. *Elife* 8, 1–28.

Gouwens, N.W., Sorensen, S.A., Berg, J., Lee, C., Jarsky, T., Ting, J., Sunkin, S.M., Feng, D., Anastassiou, C., Barkan, E., et al. (2018). Classification of electrophysiological and morphological types in mouse visual cortex. *BioRxiv*.

Gouwens, N.W., Sorensen, S.A., Berg, J., Lee, C., Jarsky, T., Ting, J., Sunkin, S.M., Feng, D., Anastassiou, C.A., Barkan, E., et al. (2019). Classification of electrophysiological and morphological neuron types in the mouse visual cortex. *Nat. Neurosci.* 22, 1182–1195.

Gouwens, N.W., Sorensen, S.A., Baftizadeh, F., Budzillo, A., Lee, B.R., Jarsky, T., Alfiler, L., Baker, K., Barkan, E., Berry, K., et al. (2020). Toward an Integrated

Classification of Cell Types: Morphoelectric and Transcriptomic Characterization of Individual GABAergic Cortical Neurons. *BioRxiv*.

Granger, A.J., Wang, W., Robertson, K., El-Rifai, M., Zanello, A.F., Bistrong, K., Saunders, A., Chow, B.W., Nuñez, V., García, M.T., et al. (2020). Cortical ChAT+ neurons co-transmit acetylcholine and GABA in a target-and brain-region-specific manner. *Elife* 9, 1–29.

Guet-McCreight, A., Skinner, F.K., and Topolnik, L. (2020). Common Principles in Functional Organization of VIP/Calretinin Cell-Driven Disinhibitory Circuits Across Cortical Areas. *Front. Neural Circuits* 14, 1–14.

Guy, J., Hendrich, B., Holmes, M., Martin, J.E., and Bird, A. (2001). A mouse *Mecp2*-null mutation causes neurological symptoms that mimic Rett syndrome. *Nat. Genet.* 27, 322–326.

Hagberg, B., Aicardi, J., Dias, K., and Ramos, O. (1983). A progressive syndrome of autism, dementia, ataxia, and loss of purposeful hand use in girls: Rett's syndrome: Report of 35 cases. *Ann. Neurol.* 14, 471–479.

Hájos, N., Acsády, L., and Freund, T.F. (1996). Target selectivity and neurochemical characteristics of VIP-immunoreactive interneurons in the rat dentate gyrus. *Eur. J. Neurosci.* 8, 1415–1431.

Han, S., Tai, C., Westenbroek, R.E., Yu, F.H., Cheah, C.S., Potter, G.B., Rubenstein, J.L., Scheuer, T., De La Iglesia, H.O., and Catterall, W.A. (2012). Autistic behavior in *Scn1a* +/- mice and rescue by enhanced GABAergic transmission. *Nature* 489, 385–390.

Hattori, R., Kuchibhotla, K. V., Froemke, R.C., and Komiyama, T. (2017). Functions and dysfunctions of neocortical inhibitory neuron subtypes. *Nat. Neurosci.* 20, 1199–1208.

He, M., Tucciarone, J., Lee, S., Nigro, M.J., Kim, Y., Levine, J.M., Kelly, S.M., Krugikov,

I., Wu, P., Chen, Y., et al. (2016). Strategies and Tools for Combinatorial Targeting of GABAergic Neurons in Mouse Cerebral Cortex. *Neuron* 92, 555.

Jackson, J., Ayzenshtat, I., Karnani, M.M., and Yuste, R. (2016). VIP+ interneurons control neocortical activity across brain states. *J. Neurophysiol.* 115, 3008–3017.

Johnson, C., Kretsge, L.N., Yen, W.W., Sriram, B., Jimenez, J.C., Jinadasa, T.J., O’Connor, A., Sky Liu, R., Nguyen, T.P.H., Cho, E.S., et al. (2020). Distinct VIP interneurons in the cingulate cortex encode anxiogenic and social stimuli. *BioRxiv*.

Kamigaki, T., and Dan, Y. (2017). Delay activity of specific prefrontal interneuron subtypes modulates memory-guided behavior. *Nat. Neurosci.* 20, 854–863.

Kaneko, K., Currin, C.B., Goff, K.M., Somarowthu, A., Vogels, T.P., and Goldberg, E.M. (2021). Developmentally-regulated impairment of parvalbumin interneuron synaptic transmission in an experimental model of Dravet syndrome. *BioRxiv*.

Kepecs, A., and Fishell, G. (2014). Interneuron Cell Types: Fit to form and formed to fit. *Nature* 505, 318–326.

Khan, A.G., Poort, J., Chadwick, A., Blot, A., Sahani, M., Mrsic-Flogel, T.D., and Hofer, S.B. (2018). Distinct learning-induced changes in stimulus selectivity and interactions of GABAergic interneuron classes in visual cortex. *Nat. Neurosci.* 21, 851–859.

Koukoulis, F., Rooy, M., Tziotis, D., Sailor, K.A., O’neill, H.C., Levenga, J., Witte, M., Nilges, M., Changeux, J.-P., Hoeffler, C.A., et al. (2017). Nicotine reverses hypofrontality in animal models of addiction and schizophrenia HHS Public Access Author manuscript. *Nat Med* 23, 347–354.

Krabbe, S., Paradiso, E., d’Aquin, S., Bitterman, Y., Courtin, J., Xu, C., Yonehara, K., Markovic, M., Müller, C., Eichlisberger, T., et al. (2019). Adaptive disinhibitory gating by VIP interneurons permits associative learning. *Nat. Neurosci.* 22, 1834–1843.

Lee, A.T., Cunniff, M.M., See, J.Z., Wilke, S.A., Luongo, F.J., Ellwood, I.T., Ponnayolu,



S., and Sohal, V.S. (2019). VIP Interneurons Contribute to Avoidance Behavior by Regulating Information Flow across Hippocampal-Prefrontal Networks. *Neuron* 102, 1223-1234.e4.

Lee, S., Hjerling-leffler, J., Zaghera, E., and Fishell, G. (2010). The largest group of superficial neocortical GABAergic interneurons expresses ionotropic serotonin receptors. *J. Neurosci.* 30, 16796–16808.

Lee, S., Kruglikov, I., Huang, Z.J., Fishell, G., and Rudy, B. (2013). A disinhibitory circuit mediates motor integration in the somatosensory cortex. *Nat. Neurosci.* 16, 1662–1670.

Li, B.-M., Liu, X.-R., Yi, Y.-H., Deng, Y.-H., Su, T., Zou, X., and Liao, W.-P. (2011). Autism in Dravet syndrome: Prevalence, features, and relationship to the clinical characteristics of epilepsy and mental retardation. *Epilepsy Behav.* 21, 291–295.

Luo, X., Guet-McCreight, A., Villette, V., Francavilla, R., Marino, B., Chamberland, S., Skinner, F.K., and Topolnik, L. (2020). Synaptic Mechanisms Underlying the Network State-Dependent Recruitment of VIP-Expressing Interneurons in the CA1 Hippocampus. *Cereb. Cortex* 30, 3667–3685.

McGinley, M.J., Vinck, M., Reimer, J., Batista-Brito, R., Zaghera, E., Cadwell, C.R., Tolias, A.S., Cardin, J.A., and McCormick, D.A. (2015). Waking State: Rapid Variations Modulate Neural and Behavioral Responses. *Neuron* 87, 1143–1161.

Millman, D.J., Ocker, G.K., Caldejon, S., Kato, I., Larkin, J.D., Lee, E.K., Luviano, J., Nayan, C., Nguyen, T. V., North, K., et al. (2020). VIP interneurons in mouse primary visual cortex selectively enhance responses to weak but specific stimuli. *Elife* 9, 1–22.

Mossner, J.M., Batista-Brito, R., Pant, R., and Cardin, J.A. (2020). Developmental loss of MeCP2 from VIP interneurons impairs cortical function and behavior. *Elife* 9, 1–14.

Munoz, W., Tremblay, R., Levenstein, D., and Rudy, B. (2017). Layer-specific modulation of neocortical dendritic inhibition during active wakefulness. *Science* (80-. ).

355, 954–959.

Oakley, J.C., Kalume, F., Yu, F.H., Scheuer, T., and Catterall, W.A. (2009).

Temperature- and age-dependent seizures in a mouse model of severe myoclonic epilepsy in infancy. *Proc. Natl. Acad. Sci. U. S. A.* *106*, 3994–3999.

Obermayer, J., Luchicchi, A., Heistek, T.S., de Kloet, S.F., Terra, H., Bruinsma, B., Mnie-Filali, O., Kortleven, C., Galakhova, A.A., Khalil, A.J., et al. (2019). Prefrontal cortical ChAT-VIP interneurons provide local excitation by cholinergic synaptic transmission and control attention. *Nat. Commun.* *10*, 461723.

Ogiwara, I., Miyamoto, H., Morita, N., Atapour, N., Mazaki, E., Inoue, I., Takeuchi, T., Itohara, S., Yanagawa, Y., Obata, K., et al. (2007). Nav1.1 localizes to axons of parvalbumin-positive inhibitory interneurons: A circuit basis for epileptic seizures in mice carrying an *Scn1a* gene mutation. *J. Neurosci.* *27*, 5903–5914.

Ogiwara, I., Iwasato, T., Miyamoto, H., Iwata, R., Yamagata, T., Mazaki, E., Yanagawa, Y., Tamamaki, N., Hensch, T.K., Itohara, S., et al. (2013). Nav1.1 haploinsufficiency in excitatory neurons ameliorates seizure-associated sudden death in a mouse model of dravet syndrome. *Hum. Mol. Genet.* *22*, 4784–4804.

Owen, M.J., and O'Donovan, M.C. (2017). Schizophrenia and the neurodevelopmental continuum:evidence from genomics. *World Psychiatry* *16*, 227–235.

Paul, A., Crow, M., Raudales, R., He, M., Gillis, J., and Huang, Z.J. (2017).

Transcriptional Architecture of Synaptic Communication Delineates GABAergic Neuron Identity. *Cell* *171*, 522-539.e20.

Pfeffer, C.K., Xue, M., He, M., Huang, Z.J., and Scanziani, M. (2013). Inhibition of inhibition in visual cortex: the logic of connections between molecularly distinct interneurons. *Nat. Neurosci.* *16*, 1068–1076.

Pi, H.J., Hangya, B., Kvitsiani, D., Sanders, J.I., Huang, Z.J., and Kepecs, A. (2013).

Cortical interneurons that specialize in disinhibitory control. *Nature* 503, 521–524.

Porter, J.T., Cauli, B., Staiger, J.F., Lambolez, B., Rossier, J., and Audinat, E. (1998). Properties of bipolar VIPergic interneurons and their excitation by pyramidal neurons in the rat neocortex. *Eur. J. Neurosci.* 10, 3617–3628.

Porter, J.T., Cauli, B., Tsuzuki, K., Lambolez, B., Rossier, J., and Audinat, E. (1999). Selective excitation of subtypes of neocortical interneurons by nicotinic receptors. *J. Neurosci.* 19, 5228–5235.

Prönneke, A., Scheuer, B., Wagener, R.J., Möck, M., Witte, M., and Staiger, J.F. (2015). Characterizing VIP neurons in the barrel cortex of VIP<sup>cre</sup>/tdTomato mice reveals layer-specific differences. *Cereb. Cortex* 25, 4854–4868.

Prönneke, A., Witte, M., Möck, M., and Staiger, J.F. (2020). Neuromodulation leads to a burst-tonic switch in a subset of VIP neurons in mouse primary somatosensory (Barrel) cortex. *Cereb. Cortex* 30, 488–504.

Reimer, J., Froudarakis, E., Cadwell, C.R., Yatsenko, D., Denfield, G.H., and Tolias, A.S. (2014). Pupil Fluctuations Track Fast Switching of Cortical States during Quiet Wakefulness. *Neuron* 84, 355–362.

Richards, K.L., Milligan, C.J., Richardson, R.J., Jancovski, N., Grunnet, M., Jacobson, L.H., Undheim, E.A.B., Mobli, M., Chow, C.Y., Herzig, V., et al. (2018). Selective NaV1.1 activation rescues Dravet syndrome mice from seizures and premature death. *Proc. Natl. Acad. Sci. U. S. A.* 115, E8077–E8085.

Rubinstein, M., Han, S., Tai, C., Westenbroek, R.E., Hunker, A., Scheuer, T., and Catterall, W.A. (2015). Dissecting the phenotypes of Dravet syndrome by gene deletion. *Brain* 138, 2219–2233.

Rudy, B., Fishell, G., Lee, S., and Hjerling-Leffler, J. (2011). Three groups of interneurons account for nearly 100% of neocortical GABAergic neurons. *Dev.*

Neurobiol. 71, 45–61.

De Stasi, A.M., Farisello, P., Marcon, I., Cavallari, S., Forli, A., Vecchia, D., Losi, G., Mantegazza, M., Panzeri, S., Carmignoto, G., et al. (2016). Unaltered Network Activity and Interneuronal Firing during Spontaneous Cortical Dynamics *in vivo* in a Mouse Model of Severe Myoclonic Epilepsy of Infancy. *Cereb. Cortex* 26, 1778–1794.

Sun, Y., Paşca, S.P., Portmann, T., Goold, C., Worringer, K.A., Guan, W., Chan, K.C., Gai, H., Vogt, D., Chen, Y.J.J., et al. (2016). A deleterious Nav1.1 mutation selectively impairs telencephalic inhibitory neurons derived from Dravet Syndrome patients. *Elife* 5, 1–26.

Tai, C., Abe, Y., Westenbroek, R.E., Scheuer, T., and Catterall, W.A. (2014). Impaired excitability of somatostatin- and parvalbumin-expressing cortical interneurons in a mouse model of Dravet syndrome. *Proc. Natl. Acad. Sci. U. S. A.* 111, 3139–3148.

Taniguchi, H., He, M., Wu, P., Kim, S., Paik, R., Sugino, K., Kvitsiani, D., Fu, Y., Lu, J., Lin, Y., et al. (2011). A resource of cre driver lines for genetic targeting of GABAergic neurons in cerebral cortex. *Neuron* 72, 1091.

Tasic, B., Menon, V., Nguyen, T.N., Kim, T.K., Jarsky, T., Yao, Z., Levi, B., Gray, L.T., Sorensen, S.A., Dolbeare, T., et al. (2016). Adult mouse cortical cell taxonomy revealed by single cell transcriptomics. *Nat. Neurosci.* 19, 335–346.

Tatsukawa, T., Ogiwara, I., Mazaki, E., Shimohata, A., and Yamakawa, K. (2018). Impairments in social novelty recognition and spatial memory in mice with conditional deletion of *Scn1a* in parvalbumin-expressing cells. *Neurobiol. Dis.* 112, 24–34.

Turi, G.F., Li, W.K., Chavlis, S., Pandi, I., O'Hare, J., Priestley, J.B., Grosmark, A.D., Liao, Z., Ladow, M., Zhang, J.F., et al. (2019). Vasoactive Intestinal Polypeptide-Expressing Interneurons in the Hippocampus Support Goal-Oriented Spatial Learning. *Neuron* 101, 1150-1165.e8.

Tyan, L., Chamberland, S., Magnin, E., Camire, O., Francavilla, R., David, L.S., Deisseroth, K., and Topolnik, L. (2014). Dendritic Inhibition Provided by Interneuron-Specific Cells Controls the Firing Rate and Timing of the Hippocampal Feedback Inhibitory Circuitry. *J. Neurosci.* *34*, 4534–4547.

Villas, N., Meskis, M.A., and Goodliffe, S. (2017). Dravet syndrome: Characteristics, comorbidities, and caregiver concerns. *Epilepsy Behav.* *74*, 81–86.

de Vries, S.E.J., Lecoq, J.A., Buice, M.A., Groblewski, P.A., Ocker, G.K., Oliver, M., Feng, D., Cain, N., Ledochowitsch, P., Millman, D., et al. (2020). A large-scale standardized physiological survey reveals functional organization of the mouse visual cortex. *Nat. Neurosci.* *23*, 138–151.

Walker, F., Möck, M., Feyerabend, M., Guy, J., Wagener, R.J., Schubert, D., Staiger, J.F., and Witte, M. (2016). Parvalbumin-and vasoactive intestinal polypeptide-expressing neocortical interneurons impose differential inhibition on Martinotti cells. *Nat. Commun.* *7*.

Wilmes, K.A., and Clopath, C. (2019). Inhibitory microcircuits for top-down plasticity of sensory representations. *Nat. Commun.* *10*, 1–10.

Yamagata, T., Ogiwara, I., Mazaki, E., Yanagawa, Y., and Yamakawa, K. (2017). Nav1.2 is expressed in caudal ganglionic eminence-derived disinhibitory interneurons: Mutually exclusive distributions of Nav1.1 and Nav1.2. *Biochem. Biophys. Res. Commun.* *491*, 1070–1076.

Yang, K., Lei, G., Jackson, M.F., and MacDonald, J.F. (2010). The involvement of PACAP/VIP system in the synaptic transmission in the hippocampus. *J. Mol. Neurosci.* *42*, 319–326.

Yao, Z., van Velthoven, C.T.J., Nguyen, T.N., Goldy, J., Seden-Cortes, A.E., Baftizadeh, F., Bertagnolli, D., Casper, T., Chiang, M., Crichton, K., et al. (2021). A

taxonomy of transcriptomic cell types across the isocortex and hippocampal formation.

*Cell* 184, 3222-3241.e26.

Zhang, S., Xu, M., Kamigaki, T., Do, J.P.H., Chang, W.-C., Jenvay, S., Miyamichi, K., Luo, L., and Dan, Y. (2014). Long-Range and Local Circuits for Top-Down Modulation of Visual Cortical Processing. *Science* (80-. ). 345, 660–665.

Zhou, X., Rickmann, M., Hafner, G., and Staiger, J.F. (2017). Subcellular Targeting of VIP Boutons in Mouse Barrel Cortex is Layer-Dependent and not Restricted to Interneurons. *Cereb. Cortex* 27, 5353–5368.

## Chapter 2: VIP interneurons are impaired in a mouse model of Dravet Syndrome

### ABSTRACT

Dravet Syndrome (DS) is a severe neurodevelopmental disorder caused by pathogenic loss of function variants in the gene *SCN1A* which encodes the voltage-gated sodium ( $\text{Na}^+$ ) channel subunit Nav1.1. GABAergic interneurons expressing parvalbumin (PV-INs) and somatostatin (SST-INs) exhibit impaired excitability in DS (*Scn1a*<sup>-/-</sup>) mice.

However, the function of a third major class of interneurons in DS – those expressing vasoactive intestinal peptide (VIP-IN) – is unknown. We recorded VIP-INs in brain slices from *Scn1a*<sup>-/-</sup> mice and wild-type littermate controls and found prominent impairment of irregular spiking (IS), but not continuous adapting (CA) VIP-INs, in *Scn1a*<sup>-/-</sup> mice.

Application of the Nav1.1-specific toxin Hm1a rescued the observed deficits. The IS vs. CA firing pattern is determined by expression of KCNQ channels; IS VIP-INs switched to tonic firing with both pharmacologic blockade of M-current and muscarinic acetylcholine receptor activation. These results show that VIP-INs express Nav1.1 and are dysfunctional in DS, which may contribute to DS pathogenesis.

## INTRODUCTION

Dravet syndrome (DS) is a severe neurodevelopmental disorder characterized by temperature-sensitive and spontaneous seizures in the first year of life followed by progression to intractable epilepsy, intellectual disability with autistic features, and a markedly increased rate of sudden unexpected death (SUDEP) (Genton et al., 2011; Kalume et al., 2013; Oakley et al., 2009; Scheffer, 2012). DS is caused by pathogenic loss of function variants in the gene *SCN1A*, resulting in haploinsufficiency of the voltage-gated sodium ( $\text{Na}^+$ ) channel  $\alpha$  subunit Nav1.1 (Claes et al., 2001). Experimental models of DS, including mice lacking a functional copy of Nav1.1 (*Scn1a*<sup>+/-</sup> mice) (Mistry et al., 2014; Ogiwara et al., 2007; Yu et al., 2006) and neurons generated from induced pluripotent stem (iPS) cells derived from DS patients (Liu et al., 2013; Sun et al., 2016), have provided important insights into the cellular and circuit basis of this disorder. Parvalbumin-immunopositive fast-spiking GABAergic interneurons (PV-INs) and somatostatin (SST)-expressing dendrite-targeting INs (SST-INs) exhibit impaired excitability in *Scn1a*<sup>+/-</sup> mice (Favero et al., 2018; Ogiwara et al., 2007; De Stasi et al., 2016; Tai et al., 2014; Yu et al., 2006). Despite advances in the understanding of underlying disease pathogenesis, DS remains incurable with a poor prognosis. How loss of Nav1.1 leads to the features that define this clinical syndrome is incompletely understood, and identifying new, targetable loci of dysfunction is critically important to developing new treatments.

Nav1.1 is expressed at the axon initial segment (AIS) of PV-INs and, to a lesser extent, SST-INs, and is a major determinant of action potential (AP) generation in these cells (Li et al., 2014; Ogiwara et al., 2007; De Stasi et al., 2016; Tai et al., 2014). Such data have led to the “interneuron hypothesis” of DS, which posits that PV and SST-IN



dysfunction is the predominant driver of both epilepsy and autism (Catterall, 2018; Catterall et al., 2010; Han et al., 2012; Ogiwara et al., 2007; Rubinstein et al., 2015; Yu et al., 2006). However, we recently showed that PV-IN hypoexcitability in *Scn1a*<sup>+/-</sup> mice is restricted to an early and transient developmental window (P11-21), with subsequent normalization of high-frequency action potential discharge by P35 (Favero et al., 2018). This finding encourages a reconsideration of the cellular basis of circuit pathology that underlies chronic epilepsy and epilepsy-associated cognitive abnormalities in DS. The functional status of the rich diversity of interneurons in the cerebral cortex (DeFelipe et al., 2013; Tremblay et al., 2016) has not been fully explored in models of DS. It could be the case that other interneuron classes are also affected and exhibit chronic dysfunction. The impact of constitutive loss of Nav1.1 on the third major class of cortical INs – those expressing vasoactive intestinal peptide (VIP-INs) – remains unknown.

VIP-INs are functionally distinct from SST and PV-INs as they preferentially target other interneurons (particularly SST-INs) rather than pyramidal cells, and thus are considered to exert a disinhibitory influence on cerebral cortical circuits (Acsády et al., 1998; Fu et al., 2014; Krabbe et al., 2018; Lee et al., 2013; Munoz et al., 2017; Pi et al., 2013; Turi et al., 2019; Zhang et al., 2014). VIP-INs also have a role in regulating the response of the cerebral cortex to ascending cholinergic neuromodulatory input from the basal forebrain (Alitto and Dan, 2013; Fu et al., 2015; Kawaguchi, 1997; Porter et al., 1999), and hence are involved in higher-order functions such as attention, memory, and cognitive processing, all of which are impaired in DS (Dravet and Oguni, 2013). Prior work has suggested that VIP-INs do not express Nav1.1 (Yamagata et al., 2017), while recent single cell RNA sequencing studies do suggest expression of Nav1.1 in VIP-INs

(Paul et al., 2017; Tasic et al., 2016). Here, we assessed the functional status of VIP-INs in *Scn1a*<sup>+/-</sup> mice and directly investigated whether VIP-INs express Nav1.1.

To address this question, we performed targeted whole cell recordings from layer 2/3 VIP-INs in acute brain slices of primary somatosensory and visual cortex in male and female *Scn1a*<sup>+/-</sup> mice and age-matched wild-type (WT) littermate controls at two different developmental time points. We found that VIP-INs exhibit impairment of AP generation and repetitive firing and confirmed the presence of Nav1.1 on putative VIP-IN axons using immunohistochemistry and confocal microscopy. However, unlike the transient abnormalities seen in PV-INs (Favero et al., 2018), this VIP-IN deficit persisted at later developmental time points. We further found that VIP-IN dysfunction in *Scn1a*<sup>+/-</sup> mice was restricted to a subset of irregular spiking (IS) VIP-INs, while continuous adapting (CA) VIP-INs were essentially normal. Deficits seen in IS VIP-INs could be reversed by application of the peptide toxin Hm1a, a recently-identified Nav1.1-specific modulator (Osteen et al., 2016). The basis of the IS firing pattern involved M-current mediated by KCNQ channels likely containing Kcnq5. Blockade of M-current with the KCNQ channel inhibitor linopirdine converted IS VIP-INs to a tonic firing mode but had no effect on CA VIP-INs. Also, muscarinic, but not nicotinic cholinergic receptor activation reversibly converted IS VIP-INs to a continuous firing mode. Overall, these results identify a novel cellular locus of dysfunction in DS that may relate to the profound and durable cognitive impairments observed in human patients (Genton et al., 2011; Scheffer, 2012; Villas et al., 2017) and additionally refines our understanding of the diversity of VIP-INs and the molecular determinants of VIP-IN function.

## RESULTS

### Neocortical vasoactive intestinal peptide expressing interneurons exhibit impaired excitability in *Scn1a*<sup>+/-</sup> mice

To assess the function of neocortical VIP-INs in *Scn1a*<sup>+/-</sup> mice, we performed targeted whole cell patch clamp recordings from fluorescently labeled neurons in layer 2/3 of primary somatosensory (“barrel”) cortex in acute brain slices prepared from juvenile and young adult triple transgenic *Scn1a*.VIP-Cre.tdTomato (tdT) mice and age-matched WT.VIP-Cre.tdT littermate controls (see Materials and Methods). VIP-INs from *Scn1a*<sup>+/-</sup> mice demonstrated multiple abnormalities that were consistent with loss of Na<sup>+</sup> current (Figure 1), including a reduced maximal steady-state firing frequency ( $67 \pm 2$  vs.  $48 \pm 3$  Hz;  $p = 3 \times 10^{-6}$ ;  $n = 150/123$  WT/*Scn1a*<sup>+/-</sup>), as well as a marked shift in the current/frequency (*I/f*; input-output) curve. There was notable spike height accommodation (rundown) during repetitive action potential discharge with a progressive depolarization of AP threshold and a decrease in AP peak value during suprathreshold current injections, suggesting enhanced accumulation of Na<sup>+</sup> channel inactivation in VIP-INs from *Scn1a*<sup>+/-</sup> mice. This data supports the conclusion that neocortical VIP-INs are hypoexcitable in *Scn1a*<sup>+/-</sup> mice relative to age-matched WT littermate controls, likely due to absence of one copy of *Scn1a* and a resulting decrease in Na<sup>+</sup> current.

### VIP interneurons express Nav1.1

Nav1.1 is known to be expressed in PV-INs and SST-INs, while a recent study suggested that VIP-INs express Nav1.2 at higher levels (Yamagata et al., 2017). However, several recent large-scale transcriptomics datasets suggest that *Scn1a* mRNA is in fact expressed in VIP-INs, and at levels similar to that seen in SST-INs (Figure S1)

(Paul et al., 2017; Tasic et al., 2016). We performed immunohistochemical analysis to confirm the presence of Nav1.1 protein in VIP-INs.

We identified fine (0.5  $\mu$ m) tdT positive, Nav1.1-immunoreactive processes emanating from the soma (Figure 1Ei-ii) or proximal dendrite (Figure 1Eiii-iv) of labeled neurons in WT.VIP-Cre.tdT mice; these were considered to correspond to the VIP-IN axon based on small caliber and larger branching angle (Prönneke et al., 2015). We identified the axon in 30 VIP-INs and found that 23 of 30 (77%) identified axons expressed Nav1.1 (Figure S2). In order to validate the specificity of this staining, we performed Nav1.1 immunohistochemistry of tissue from *Scn1a*<sup>-/-</sup> null mice and found no immunoreactivity (Figure S3 A-B). As a positive control, we found high expression of Nav1.1 on PV-IN axons (Figure S3 C). This data confirms that Nav1.1 protein is present on the axon of many VIP-INs.

### **Two electrophysiological subgroups of VIP-INs in neocortical layer 2/3**

Results presented thus far indicate that VIP-INs express Nav1.1 and exhibit impaired excitability in *Scn1a*<sup>+/-</sup> mice. In the course of these initial experiments, we observed a subset (~50%) of VIP-INs in *Scn1a*<sup>+/-</sup> mice that only fired a brief train of APs before complete cessation of firing (Figure 1A), which was atypical for VIP-INs from WT mice. This prompted us to explore how our data from *Scn1a*<sup>+/-</sup> mice mapped onto previously described VIP-IN firing patterns. VIP-INs in superficial layers of mouse and rat barrel cortex exhibit spike frequency adaptation with or without irregular spiking and/or initial bursting (variably referred to in the literature as continuous adapting, irregular spiking, bursting, or fast adapting) (He et al., 2016; Prönneke et al., 2015). However, there is no existing standardized or widely agreed upon nomenclature to describe VIP-IN firing patterns.

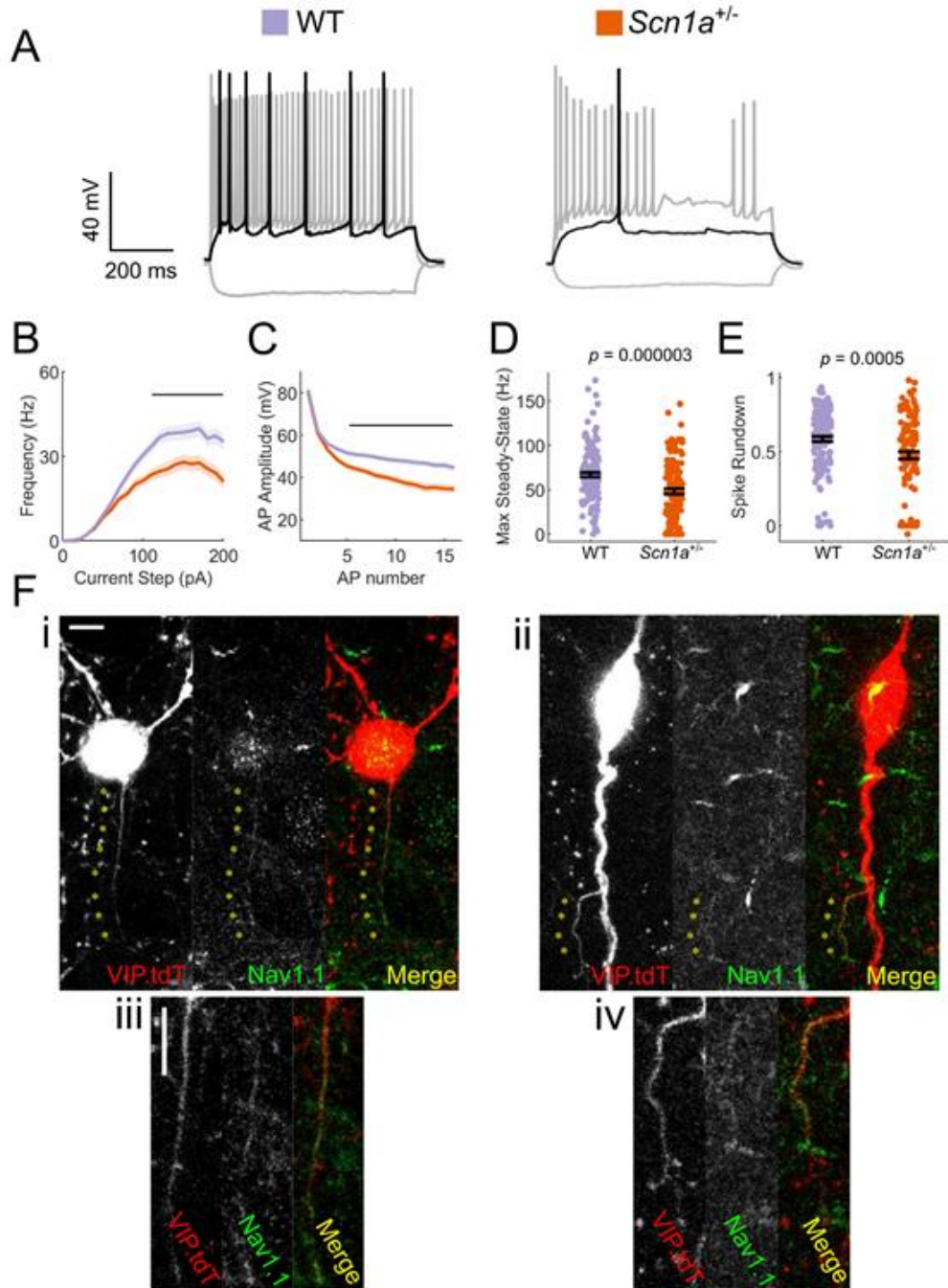


**Figure 1. VIP-INs express Nav1.1 and are hypoexcitable in *Scn1a*<sup>+/-</sup> mice**

A) Representative traces of layer 2/3 VIP-INs from a *Scn1a*<sup>+/-</sup> mouse and age matched WT littermate. Location of scale bar indicates -70 mV. *Black* indicates rheobase current injection, while *gray* indicates response to a -50 pA hyperpolarizing and a 2X rheobase suprathreshold current injection.

- B) Current/frequency (*I-f*) output curve of  $n = 123$  VIP-INs from 24 *Scn1a*<sup>+/-</sup> mice and  $n = 150$  VIP-INs from 38 age matched WT littermates (See Figure S6 for age specific data). Line and shaded area represent mean +/- SEM, and the black bar indicates significance at  $p < 0.01$  by a multivariate ANOVA and post-hoc Bonferroni correction.
- C) Population average of spike amplitude (AP peak – AP threshold) of repeated action potentials measured at 3X rheobase for each cell. Line and shaded area represent mean +/- SEM. The black bar indicates significance at  $p < 0.01$  by a multivariate ANOVA and post-hoc Bonferroni correction.
- D) Bar graphs showing individual cell values (dots) and the population mean +/- SEM for the maximal steady-state firing frequency of each cell (see methods).  $p$  values determined by Mann–Whitney U test.
- E) Bar graphs showing individual cell values (dots) and the population mean +/- SEM for the reduction in spike amplitude of the tenth AP measured in B normalized to the first AP.  $p$  values determined by Mann–Whitney U test. All comparisons consider each cell as  $n = 1$  (see Table S1 for per-animal comparisons).
- F) Example images of WT VIP-INs showing immunohistochemical labeling of Nav1.1 on putative axons originating either from the soma (i, inset iii) or a proximal dendrite (ii, inset iv). Asterisks indicate regions of colocalization between Nav1.1 and tdT expression in VIP-INs. Scale is 5  $\mu\text{m}$ .
- 

We identified a diversity of VIP-IN firing patterns in response to step depolarizations consistent with previously described continuous adapting (CA), irregular spiking (IS), and bursting cells (von Engelhardt et al., 2007; He et al., 2016; Lee et al., 2010; Porter et al., 1998, 1999; Prönneke et al., 2015). However, when we delivered longer (8-10 second) suprathreshold depolarizing pulses, we found that all cells could be separated into two clear groups (Figure 2). Approximately half of all VIP-INs fired continuously, albeit with spike frequency adaptation (here referred to as CA VIP-INs), while the other half instead fired a burst of action potentials prior to switching to an irregular spiking pattern (IS VIP-INs), often with a variable silent period in between the two phases (Figure 2A). We could reliably identify these two groups using k-means clustering of the length of the initial burst of action potentials and the coefficient of variation of the inter-spike interval (ISI CoV), but these groups were not distinguishable when using 600 ms pulses alone (Figure 2C,D). Many cells that fired continuously during 600 ms sweeps were in fact clearly IS based on response to these longer

depolarizations; likewise, cells that might be classified as bursting and which appear to cease firing during 600 ms sweeps eventually switch to an IS mode with longer depolarizations.

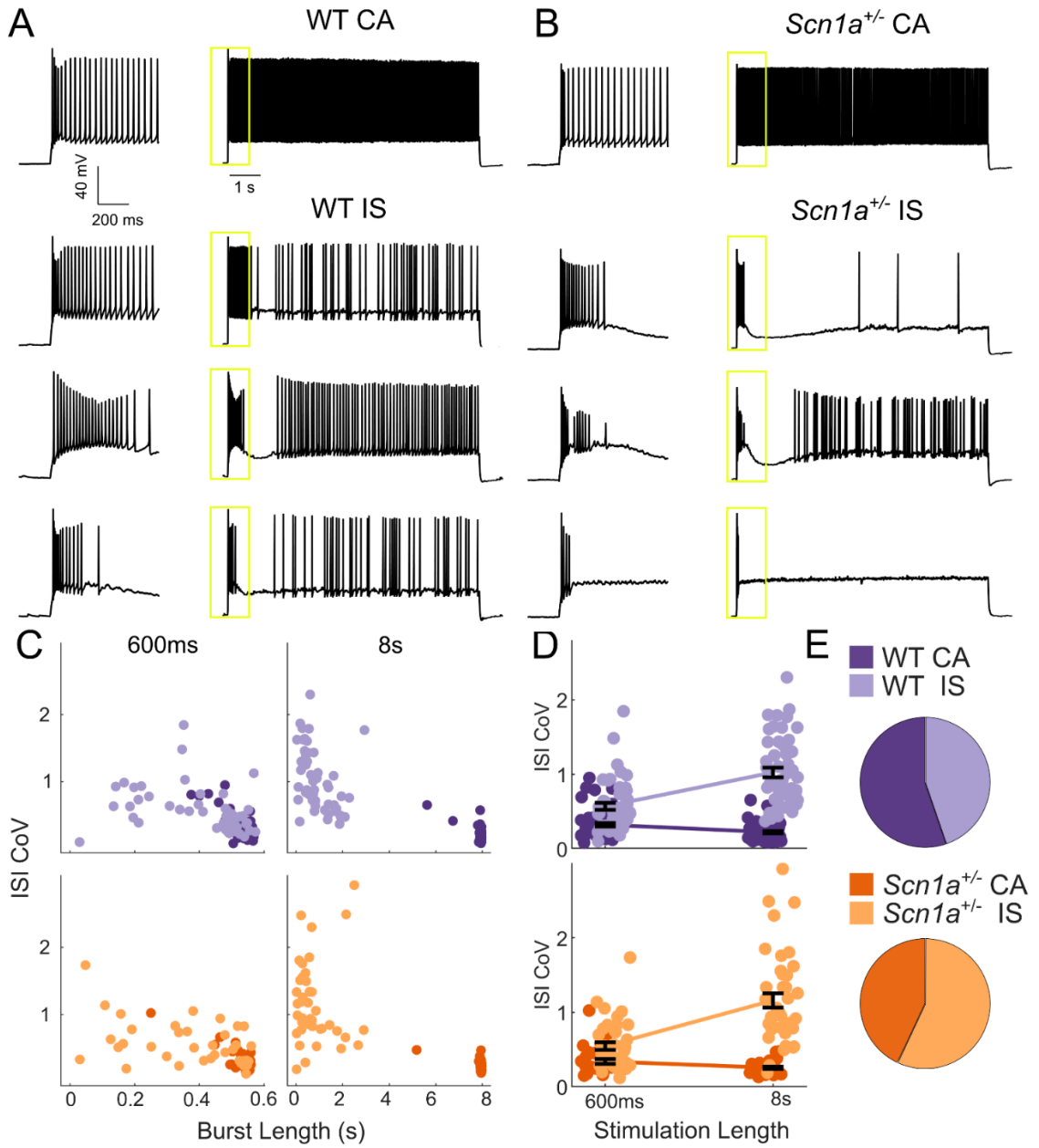


## Figure 2. Two VIP-IN firing patterns revealed with long depolarization

- A) Four representative cells displaying the range of VIP-IN firing patterns. On the left are APs elicited with a standard (600 ms) current injection. On the right are firing patterns recorded with 8 sec long depolarizations using the same current amplitude as on the left (2X rheobase for each cell). CA and IS firing patterns are easily separated with 8-second depolarization, but not distinguishable using only the first 600 ms. These firing patterns were consistent even when we stimulated with higher current injections (see Figure 3Aii-iii).
  - B) Similar CA and IS patterns were observed in VIP-INs from *Scn1a*<sup>+/-</sup> mice, with a deficit in IS VIP-IN firing.
  - C) Characterization of VIP-IN firing patterns using two key measures: the length of the initial burst of action potentials, and the coefficient of variation of the inter-spike interval (ISI CoV). These parameters were measured using either 600 ms or 8-second long rectangular depolarization in cells from both WT and *Scn1a*<sup>+/-</sup> mice; then, k-means clustering of the 8-second data was performed (light/dark colors indicating the results of clustering into 2 groups). Note the clear separation between the two groups in the 8-second data, but large overlap when looking only at data generated from 600 ms current injections.
  - D) The same data as in C, but highlighting the dependence of the measured ISI CoV on the length of the depolarization. With 600 ms sweeps, there is considerable overlap between CA and IS cells in both genotypes; however, with 8 s depolarizations, the two groups separate with minimal overlap.
  - E) Similar proportions of CA and IS cells in WT and *Scn1a*<sup>+/-</sup> mice. For C-E,  $n = 51$  IS and 63 CA from 24 WT mice, and  $n = 41$  IS and 31 CA from 17 *Scn1a*<sup>+/-</sup> mice;  $p = 0.10$  via chi-square test; chi-square statistic = 2.63.
- 
- 

A recent study implicated T-type calcium channels as the mechanism of bursting at rheobase observed in a small subset (~20%) of VIP-INs (Prönneke et al., 2020). We considered whether this group corresponded to the IS VIP-INs described here. A prepulse step depolarization to -55 mV to inactivate T-type channels had no effect on the suprathreshold response of IS-VIPs here (Figure S4 A-B). We were able to clearly identify CA and IS VIP-INs using a slow 8-second ramp current injection to induce inactivation of T-type calcium channels (Figure S4 C-E). Finally, we found that a subset of both CA and IS VIP-INs burst at rheobase, indicating that our IS VIP-IN category does not correspond directly to these previously described bursting VIP-INs (Figure S5). Hence, we concluded that irregular spiking vs. bursting at rheobase are mechanistically distinct features of in VIP-INs.



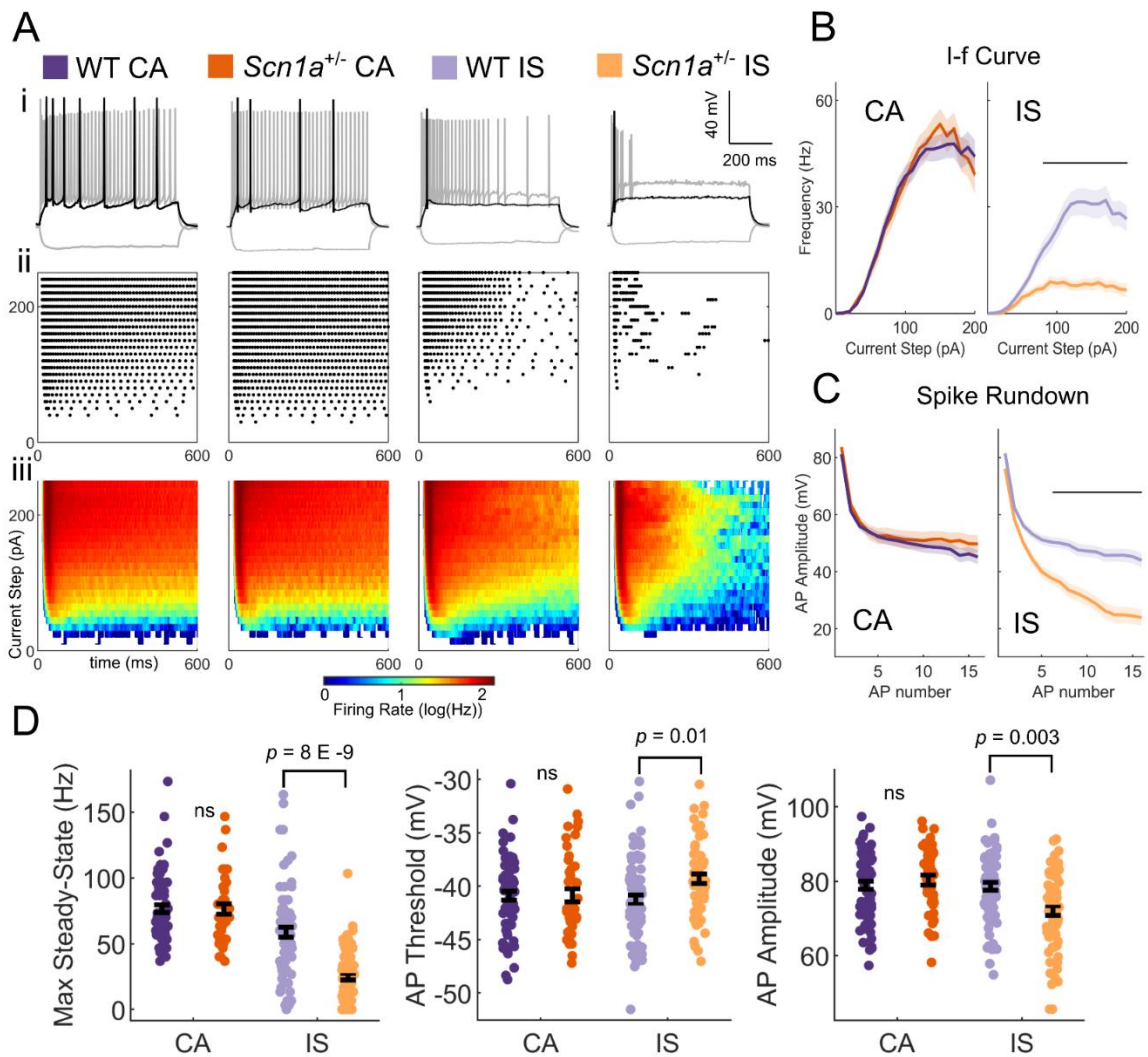


**Figure 3. IS VIP-INs are preferentially impaired in *Scn1a*<sup>+/-</sup> mice**

- A) i. Example traces of CA and IS VIP-INs from WT and *Scn1a*<sup>+/-</sup> mice, showing responses at -50pA hyperpolarizing (gray), rheobase (black), and 2X rheobase current injections (gray; typically ~100-140 pA). ii. Raster plots of all APs elicited with standard 600 ms current steps in 10 pA increments for the cells in i. iii. Population averages of the raster plots in ii, represented as heat maps where the color corresponds to the instantaneous firing rate for each give current step using a 20 ms sliding average.
- B) Current/frequency (IF) plots for groups shown in A. Line and shaded area represent mean  $\pm$  SEM. Bar indicates  $p < 0.001$  by a multivariate ANOVA and post-hoc Bonferroni correction.

- C) Population average of AP amplitude for repeated action potentials elicited at 3X rheobase for each cell. Line and shaded area represent mean  $\pm$  SEM. Bar indicates  $p < 0.001$  by a multivariate ANOVA and post-hoc Bonferroni correction.
- D) Bar graphs showing individual cell values (dots) and the population mean  $\pm$  SEM for several markers of VIP-IN excitability.  $p$  values determined by Kruskal-Wallis with post-hoc Dunn's test. For simplicity, differences between CA and IS cells are not shown (see Table S1). For B-D,  $n = 71$  IS and 78 CA cells from 32 WT mice, and  $n = 66$  IS and 43 CA cells from 22 *Scn1a*<sup>+/-</sup> mice were included. All groups were determined using 8-second square (Figure 2) or ramp depolarizations (Figure 5-Figure supplement 1) or, for a subset of IS VIP-INs for which we did not record 8 second depolarizations, if their definitive firing pattern was clear with a 600 ms depolarization (as in Ai).
- 

### **IS VIP-INs are specifically impaired in *Scn1a*<sup>+/-</sup> mice**

While VIP-INs exhibit decreased excitability in *Scn1a*<sup>+/-</sup> mice, dividing the data set into CA and IS VIP-INs revealed that IS VIP-INs are particularly impaired while CA VIP-INs are relatively spared. We determined that CA and IS VIP-INs are present in *Scn1a*<sup>+/-</sup> and WT mice in similar proportions as determined by our unbiased classification (Figure 2B,E). IS VIP-INs displayed more severe deficits compared to the pooled dataset (Figure 1), with a depolarized AP threshold (WT vs. *Scn1a*<sup>+/-</sup> mice:  $-41.3 \pm 0.5$  vs.  $-39.3 \pm 0.4$ ;  $p = 0.01$ ), decreased AP amplitude ( $79 \pm 1.0$  vs.  $72 \pm 1.3$  mV;  $p = 0.003$ ) and steady-state firing ( $59 \pm 4$  vs.  $25 \pm 3$  Hz;  $p = 8 \times 10^{-9}$ ), a clear difference in the *I*-*f* curve, and notable spike rundown with repetitive discharge (Figure 3). These differences remained significant when we treated each animal (rather than a cell) as an  $n$  (Table S1). CA VIP-INs from *Scn1a*<sup>+/-</sup> mice showed no statistical differences compared to CA VIP-INs from age-matched WT littermate controls across a range of additional measures of intrinsic excitability, properties of individual action potentials, and features of repetitive firing (Table S1). Additionally, subtype differences between CA and IS VIP-INs were consistent between WT and *Scn1a*<sup>+/-</sup> mice, including presence of increased voltage sag in response to hyperpolarizing current injection and shorter (faster) AP half-width and rise-time, with IS VIP-INs more likely to burst at rheobase (Figure S5, Table S1).

As prior work showed that the electrophysiological abnormalities identified in PV-INs in *Scn1a*<sup>+/-</sup> mice are limited to a narrow developmental window between P11-21 (Favero et al., 2018), we subdivided our analysis based on age and found nearly identical results at P18-21 and P30-55 for both IS and CA VIP-INs (Figure S6). To assess whether impairment of IS VIP-INs was a general phenomenon or restricted to primary somatosensory neocortex, we additionally performed a set of recordings in layer 2/3 primary visual cortex, again finding a similar proportion of IS vs. CA VIP-INs and replicating our central finding that IS VIP-INs were selectively hypoexcitable in *Scn1a*<sup>+/-</sup> mice (Figure S7).

#### **Modulation of Nav1.1 rescues IS VIP-IN function in *Scn1a*<sup>+/-</sup> mice**

To further support our hypothesis that VIP-INs are impaired in *Scn1a*<sup>+/-</sup> mice due to decreased expression of Nav1.1, we attempted to rescue VIP-IN function by directly targeting Nav1.1 pharmacologically. Hm1a is a recently described spider toxin that enhances Nav1.1 current via inhibiting fast and slow inactivation (Osteen et al., 2016, 2017). In acute brain slices prepared from *Scn1a*<sup>+/-</sup> mice, bath application of 1  $\mu$ M Hm1a led to markedly increased steady-state firing in IS VIP-INs (control,  $33 \pm 2$  Hz; Hm1a,  $97 \pm 5$  Hz;  $p = 0.001$ ) and attenuation of spike rundown (Figure 4A-C). We did observe an effect in CA VIP-INs at this concentration, with a small increase in steady-state firing frequency (control,  $58 \pm 4$  Hz; Hm1a,  $68 \pm 5$  Hz;  $p = 0.05$ ) and attenuated spike height accommodation. As a positive control, Hm1a increased the maximum steady-state firing rate of PV-INs in *Scn1a*<sup>+/-</sup> mice at P18-21 (control,  $229 \pm 2$  Hz; Hm1a,  $292 \pm 6$  Hz;  $p = 0.004$ ), although this effect was proportionally smaller than what we observed in IS VIP-INs (mean difference of 295% in IS VIP-INs compared to 28% in PV-INs). In contrast,

Hm1a had no measurable effect on the firing of layer 2/3 neocortical pyramidal neurons in WT mice, supporting the specificity of this toxin to Nav1.1 and the smaller role of Nav1.1 in the regulation of pyramidal cell excitability relative to interneurons. We repeated this rescue experiment of IS VIP-IN excitability using 50 nM Hm1a, which is highly selective for Nav1.1 over other non-Nav1.1 Nav1.X subunits (Osteen et al., 2016; Richards et al., 2018), and obtained identical results (Figure S8). Importantly, although Hm1a causes a dramatic increase in steady-state firing of IS VIP-INs, these cells still retain a distinct irregular firing pattern in the presence of Hm1a in response to longer depolarizations (Figure S8).

#### **Hm1a modulates Na<sup>+</sup> current inactivation in VIP-INs**

The mechanism of action of Hm1a involves destabilizing the inactive state of Nav1.1, which increases the availability of Nav1.1 channels at depolarized potentials by shifting more channels to the closed vs. inactive state. If VIP-INs indeed express Nav1.1, then Hm1a could lead to a rescue of IS VIP-IN function by preventing an accumulation of Na<sup>+</sup> channel inactivation during repetitive firing. To test this possibility, we directly measured the effect of Hm1a on Na<sup>+</sup> current in VIP-INs using whole cell voltage clamp recordings of genetically labelled VIP-INs isolated from acutely dissociated cortex of P18 WT.VIP-Cre.tdT mice (Figure 4D-F). Hm1a slowed the time constant of inactivation and increased slowly-inactivating/persistent current in VIP-INs, with no effect on the peak current density. This further supports the presence of Nav1.1 in VIP-INs and indicates that Hm1a has a similar effect on inactivation of endogenous Na<sup>+</sup> current in VIP-INs as compared to previously published data on Nav1.1 expressed in heterologous systems.

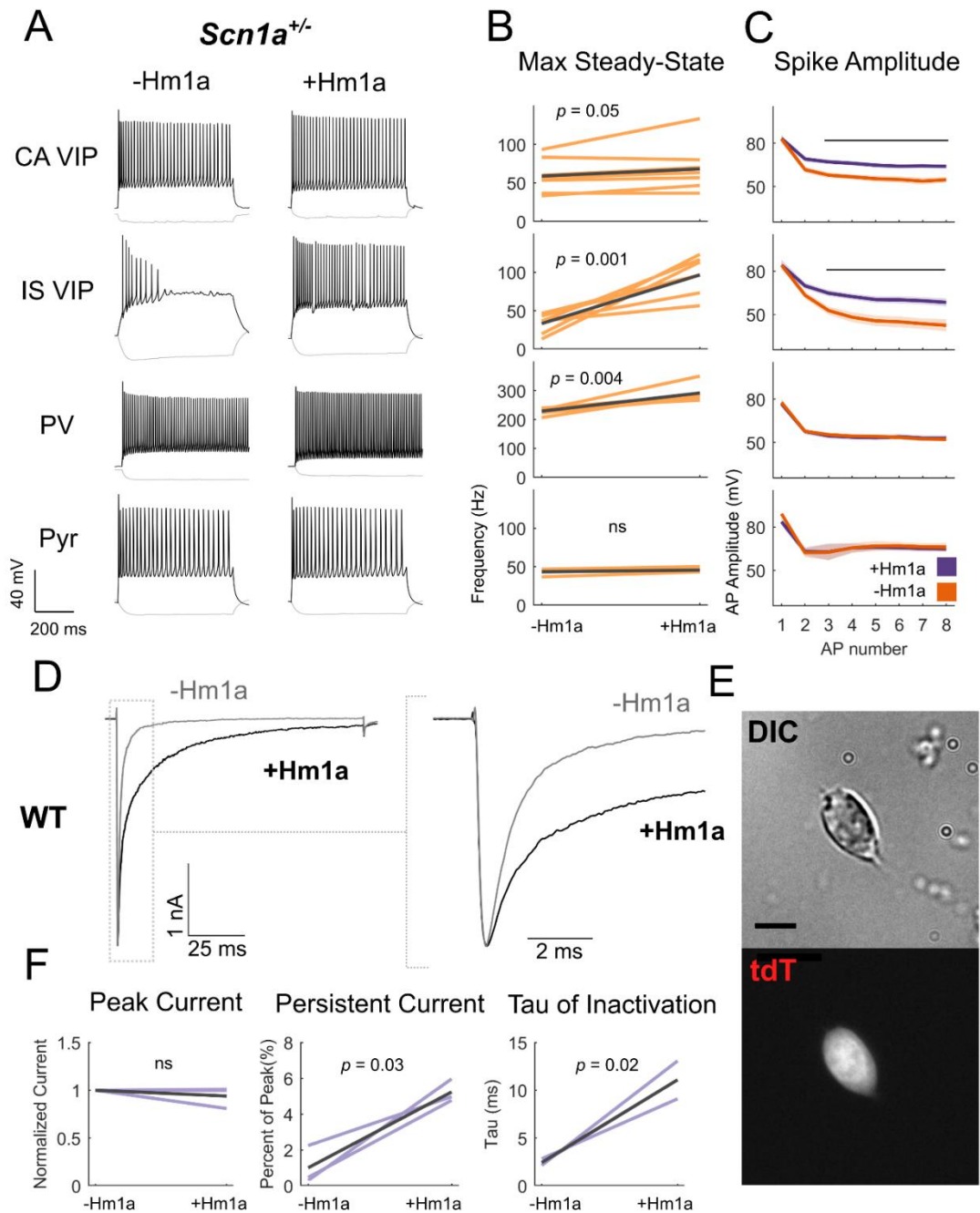


**Figure 4. Hm1a application modulates Na<sup>+</sup> channels containing Nav1.1 subunits in VIP-INs and recovers IS VIP-IN hypofunction in *Scn1a*<sup>+/-</sup> mice**

A) Example traces from recordings of representative CA and IS VIP-INs from *Scn1a.VIP-Cre.tdT* mice, as well as a PV-IN and pyramidal neuron from a *Scn1a.PV-*

- Cre.tdT mouse, before and after bath application of 1  $\mu$ M Hm1a at a 3X rheobase (near maximal) current injection for each cell. Note that the horizontal scale for the PV-IN is 100 ms instead of 200 ms, to facilitate visualization of individual APs.
- B) Change in the max steady state firing frequency of  $n = 9$  CA VIP-INs, 7 IS VIP-INs, 6 PV-INs, and 3 pyramidal neurons from a total of 5 *Scn1a*.VIP-Cre.tdT and 2 *Scn1a*.PV-Cre.tdT P18-21 mice, with  $p$  values and significance determined using a paired students' t-test.
  - C) Spike amplitude of successive APs elicited at 3X rheobase for each cell. Line and shaded area represent mean  $\pm$  SEM, and bar indicates significance at  $p < 0.01$  via a multivariate ANOVA and post-hoc Bonferroni correction.
  - D) Example traces from voltage clamp recordings of VIP-INs from acutely dissociated cortex of P18 WT.VIP-Cre.tdT mice. *Light gray* shows the initial transient  $\text{Na}^+$  current recorded with a single voltage command step from -80 mV to 0 mV. *Black* shows the response following bath application of 500 nM Hm1a. The dashed line indicates the inset (shown on the *right*). There is no change in the peak amplitude, but clear slowing of inactivation.
  - E) Example differential interference contrast image of a dissociated VIP-IN, as well as the tdT signal imaged with epifluorescence. VIP-INs had small bipolar or rounded shapes. Scale = 5  $\mu$ M.
  - F) Quantification of the effects of Hm1a on  $n = 3$  VIP-INs from 2 P18 WT.VIP-Cre.tdT mice. Purple lines represent the change of each individual cell, with  $p$  values determined by a paired students' t-test.
- 

### **Irregular spiking is not correlated with VIP-IN molecular markers**

The rescue of IS VIP-IN excitability with Hm1a supports our conclusion that IS VIP-INs are particularly impaired in *Scn1a*<sup>+/-</sup> mice. To attempt to understand how the specific dysfunction of IS VIP-INs is involved in DS pathogenesis, we investigated whether the IS and CA firing patterns identified here map onto previously described morphological and molecularly defined VIP-IN subgroups. Intersectional Cre/Flp labeling of VIP/cholecystokinin (VIP/CCK) or VIP/calretinin (VIP/CR) double positive INs defines two minimally-overlapping subsets of VIP-INs (He et al., 2016; Porter et al., 1998). In these mice, VIP/CR-INs have a bipolar morphology, while VIP/CCK INs tend to be multipolar. We used whole cell recording with morphological analysis to compare our electrophysiological classification scheme with the subtypes labeled via this intersectional strategy (Figure 5). We filled cells with Alexa-488 during whole-cell recording, generated 2P image stacks, and quantified the dendritic arborization pattern

of each cell. VIP/CR-INs were more often bipolar, or “vertically biased,” compared to VIP/CCK-INs (Figure 5A), as shown previously (He et al. , 2016), but CR and CCK did not reliably define electrophysiological subtypes of VIP-INs (Figure 5A-B), nor were there any differences in morphology between the CA and IS VIP-INs within a given genotype (Figure 5C). This data argues that IS and CA firing patterns do not coincide with previously described VIP-IN subgroups.

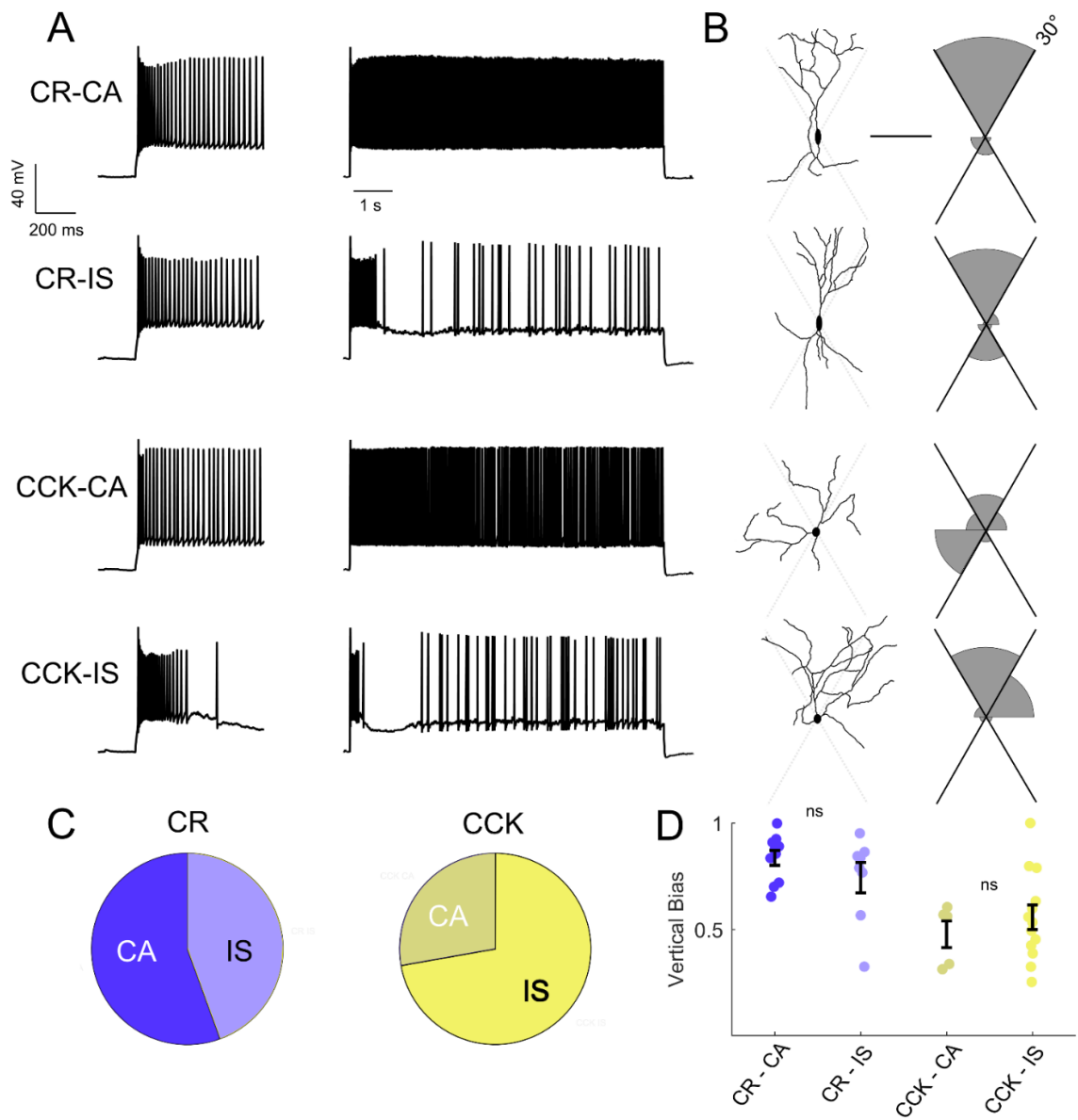


**Figure 5. Intersectional expression of CR and CCK labels anatomical subsets of VIP-INs but does not correlate with IS vs. CA firing patterns.**

- A) Example traces from layer 2/3 VIP-INs in barrel cortex of adult CR-Cre/VIP-Flp and CCK-Cre/VIP-Flp mice. Both CA and IS firing patterns were observed in each intersectional population of VIP-INs. Insets on the left show the first 600ms of each 8-second depolarization.
  - B) Morphological reconstruction of the proximal dendrites of the cells in A to illustrate dendritic orientation. Scale is 100  $\mu$ m. The adjoining histogram quantifies the proportion of total dendrite that lies within or outside of 30° from vertical (perpendicular to the pial surface). Black axes indicate the length of histogram corresponding to 100%.
  - C) Proportion of CR and CCK VIP-INs that are CA vs. IS ( $n = 17$  total VIP-INs from 3 CR-Cre/VIP-Flp mice and  $n = 19$  VIP-INs from CCK-Cre/VIP-Flp mice);  $p > 0.1$  by Chi-square test.
  - D) Individual cells (*dots*) and population mean  $\pm$  SEM for the vertical bias of each cell calculated from the morphological reconstructions in B. Vertical bias is the percent of dendrite within 30° of the line perpendicular to the pial surface, with a value of 1 corresponding to a perfectly bipolar shape. CA and IS VIP-INs in CR-Cre/VIP-Flp mice are mostly bipolar, with high vertical bias; CA and IS VIP-INs from CCK-Cre/VIP-Flp mice are multipolar, with vertical bias of  $\sim 0.5$ . Traditional Scholl analysis did not clearly illustrate this key difference between VIP-INs.
- 

**Irregular spiking of VIP-INs is determined by M-current**

Despite the negative finding above, we were interested in the molecular determinants of the IS discharge pattern to better understand why IS VIP-INs are selectively impaired in *Scn1a*<sup>+/-</sup> mice. The firing pattern of IS VIP-INs could suggest the presence of a slowly activating potassium conductance in these cells. M-current, mediated by KCNQ channels, is known to possess such properties and has been hypothesized to regulate mode switching between tonic and bursting/irregular firing (Drion et al., 2010; Stiefel et al., 2013). Single-cell transcriptomics data suggests relatively high expression of the KCNQ subunit Kcnq5 in a subset of VIP-INs, including approximately half of all VIP/CR and VIP/CCK-INs, with minimal expression in either PV or SST-INs. KCNQ subfamily member Kcnq2 is more broadly expressed across all INs, while Kcnq1/3/4 show very limited cortical expression (Figure S9, Paul et al., 2017; Tasic et al., 2016). We confirmed these data using immunohistochemistry for Kcnq5 and



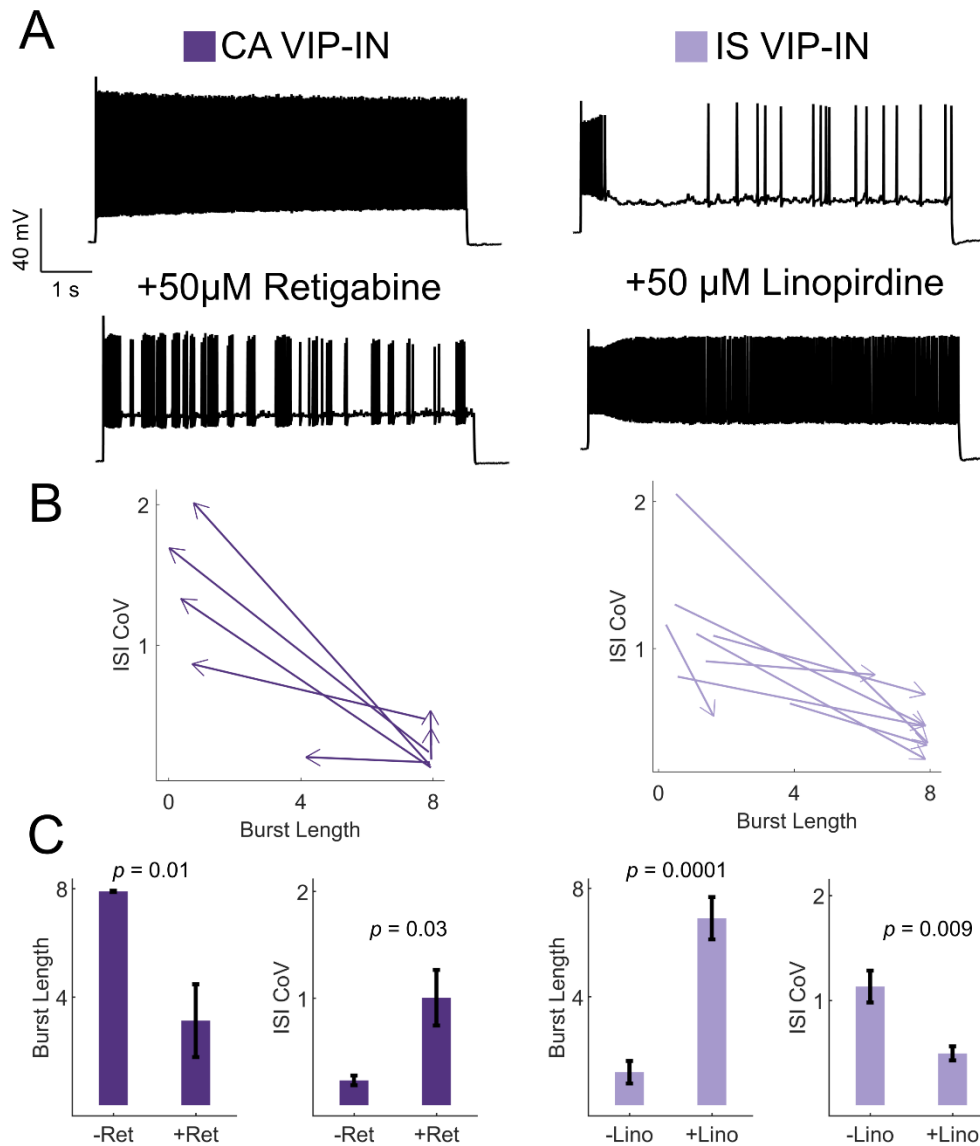


**Figure 6. KCNQ channels regulate VIP-IN firing patterns**

- A) Example traces from representative CA and IS VIP-INs in response to 8-second depolarization at 2X rheobase before and after bath application of either the KCNQ activator retigabine (*left*) or inhibitor linopirdine (*right*), respectively.
- B) The response of  $n = 7$  CA and  $n = 8$  IS cells from 4 WT.VIP-Cre.tdT mice to the above drug application. Arrows indicate the direction of change in ISI CoV value and burst length (as in Figure 2C) after drug application, with the base of the arrow corresponding to the initial measurement, and the arrowhead corresponding to the values measured after drug application.
- C) Mean  $\pm$  SEM of each value in B before and after drug application, with  $p$ -values and significance determined by a paired students t-test.

Kcnq3. Kcnq5 was expressed in ~40% of layer 2/3 VIP-INs and essentially no SST-INs (but was expressed in many presumptive pyramidal cells), while Kcnq3 showed very limited immunoreactivity in the superficial cortex overall and was not found on VIP-INs (Figure S10).

Based on this data, we hypothesized that M-current mediated by Kcnq5-containing KCNQ channels underlies irregular spiking in IS VIP-INs, while CA VIP-INs do not rely on M-current for their firing properties. Using KCNQ channel-specific pharmacology, we were able to bidirectionally modulate the firing patterns of IS and CA VIP-INs, interconverting firing patterns by either blocking or activating M-current with the KCNQ channel inhibitor linopirdine or the KCNQ channel activator retigabine, respectively (Figure 6). IS VIP-INs showed a marked increase in sustained firing with the addition of linopirdine and resembled CA VIP-INs in terms of burst length and ISI CoV. Conversely, some CA VIP-INs became “IS-like” upon application of retigabine. However, linopirdine had essentially no effect on CA VIP-IN excitability or intrinsic properties (Figure S11) indicating that whatever M-current is present in these cells is not a major regulator of cellular excitability. Such data indicates that M-current expression is a critical but selective determinant of the electrical excitability of IS VIP-INs. However, M-current does not seem to correlate with expression of VIP-IN markers such as CR and CCK, or with VIP-IN morphology.

### **Cholinergic switching from irregular to continuous firing in VIP-INs**

VIP-INs are strongly recruited by ascending cholinergic modulation *in vivo* (Fu et al., 2014), and M-current is characteristically inhibited by muscarinic receptor activation (Brown and Passmore, 2009). Therefore, we hypothesized that acetylcholine would activate IS VIP-INs and induce switching to a continuous firing mode. Bath application of

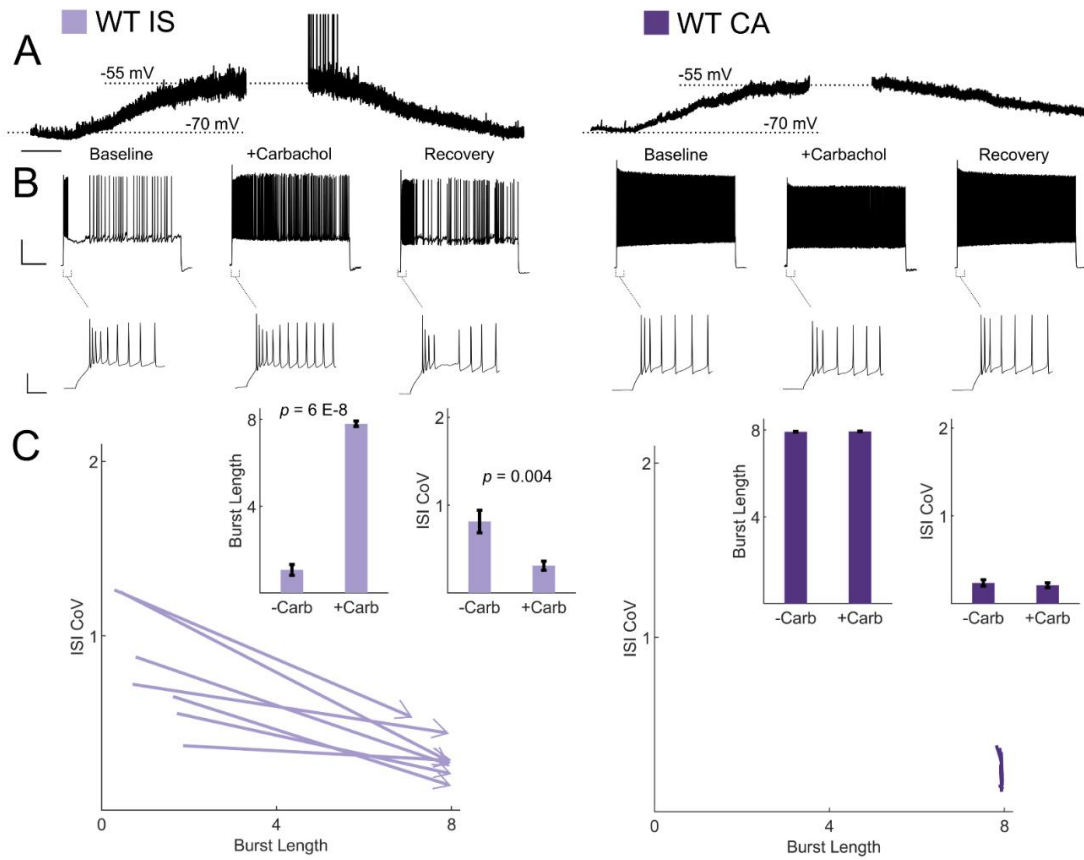


**Figure 7. Cholinergic modulation induces switching from irregular to continuous firing in IS VIP-INs**

- A) Depolarization in resting membrane potential of IS and CA VIP-INs with bath application of 5  $\mu$ M Carbachol. Horizontal scale bar, 1 minute. In addition to membrane depolarization, there was a notable increase in synaptic activity, and in some cases spontaneous firing. Population mean  $\pm$  SEM of the change in membrane potential was  $13 \pm 5$  and  $10 \pm 5$  mV for IS and CA VIP-INs respectively ( $p > 0.05$ ).
- B) Action potential trains elicited with 8-second long square depolarizations at 2X rheobase current injections before, during, and after washout of 5  $\mu$ M carbachol. In each case, the membrane potential was offset to -70 mV by direct current injection. Scale bars, 40 mV and 1 second. Insets showing no change in the initial bursting characteristics at suprathreshold current injections with the application of carbachol. Scale bars, 40 mV and 50 ms.
- C) Quantification of changes in firing patterns of  $n = 7$  IS and  $n = 8$  CA VIP-INs from 3 WT.VIP-Cre.tdT mice in response to carbachol. All IS cells showed a qualitative switch to a continuous firing mode represented by increased burst length and decreased ISI CoV (indicated by arrowheads as in Figure 6);  $p$ -values determined by paired students' t-test. There were no apparent changes in CA VIP-IN firing patterns with carbachol application (arrowheads omitted for clarity).

the cholinomimetic carbachol (5  $\mu$ M) produced a 10-15 mV depolarization in both CA and IS VIP-INs (Figure 7A). However, the suprathreshold firing properties of IS VIP-INs again converted to a “CA-like” pattern, firing for a full 8-second depolarizing pulse with decreased irregularity. There was essentially no effect on the firing pattern of CA VIP-INs, nor was there any effect on the initial bursting characteristics of either IS or CA VIP-INs (Figure 7B,C). The effect of carbachol closely resembled the effect of linopirdine on IS VIP-INs. Similarly, we found that muscarinic, but not nicotinic stimulation, induced tonic firing in IS VIP-INs, while both types of cholinergic stimulation independently produced membrane potential depolarization of similar magnitude ( $4.24 \pm 0.7$  mV for muscarinic vs.  $5.48 \pm 1.4$  mV for nicotinic;  $p > 0.05$ ; Figure S12). Hence, M-current inhibition via activation of muscarinic acetylcholine receptors represents a novel mechanism of neuromodulation in VIP-INs that is separate from the recently described tonic depolarization caused by nicotinic acetylcholine receptor activation (Askew et al., 2019).

### **A single compartment model recapitulates the interaction between M-current and $\text{Na}^+$ current density in the determination of VIP-IN discharge pattern**

Taken together, evidence for a broad distribution of *Scn1a* across INs from RNA sequencing data, our own immunohistochemistry showing Nav1.1 protein on the axon of most VIP-INs, as well as the response of both IS and CA VIP-INs to Hm1a, suggests that Nav1.1 is likely present in both IS and CA VIP-INs, but that action potential generation in IS VIP-INs is more affected by heterozygous loss of Nav1.1. This could be due to a combination of lower non-Nav1.1-mediated  $\text{Na}^+$  current in IS VIP-INs (such that these cells are more reliant on Nav1.1 for spike generation and repetitive firing), combined with relatively higher expression of M-current mediated by Kcnq5-containing

KCNQ channels. To explore this question, we constructed a classic Hodgkin-Huxley (H-H) single compartment model, adding a slowly activating potassium current (gKS) to simulate the influence of M-like current (Stiefel et al., 2013) in VIP-INs (Figure 8).

After setting the standard H-H parameters to approximate the firing pattern of a typical WT CA VIP-IN (see Materials and Methods), we increased M-current density to produce a response qualitatively similar to WT IS VIP-INs. Then, we performed a parameter sweep, varying both the M-current and Na<sup>+</sup> current density to simulate the effect of loss of one copy of *Scn1a* in the presence or absence of M-current. Reducing Na<sup>+</sup> current by up to 50% in models with little or no M-current had only minor effects on excitability (Figure 8), similar to our recordings from CA VIP-INs in *Scn1a*<sup>+/-</sup> mice. However, in models with increasing amounts of M-current, reducing Na<sup>+</sup> current density had a progressively more dramatic effect, leading to action potential failure after only a few action potentials (Figure 8), similar to what we observed experimentally in *Scn1a*<sup>+/-</sup> IS VIP-INs. Therefore, both the CA and IS-VIP firing patterns that characterize VIP-IN diversity, as well as the effect of loss of one copy of *Scn1a*, are captured in a simple model with continuous distributions of both Na<sup>+</sup> and M-current. This supports our conclusion that most or all VIP-INs express Nav1.1, and that IS VIP-INs – which have a prominent M-current mediated by Kcnq5-containing KCNQ channels – are selectively dysfunctional in *Scn1a*<sup>+/-</sup> mice.

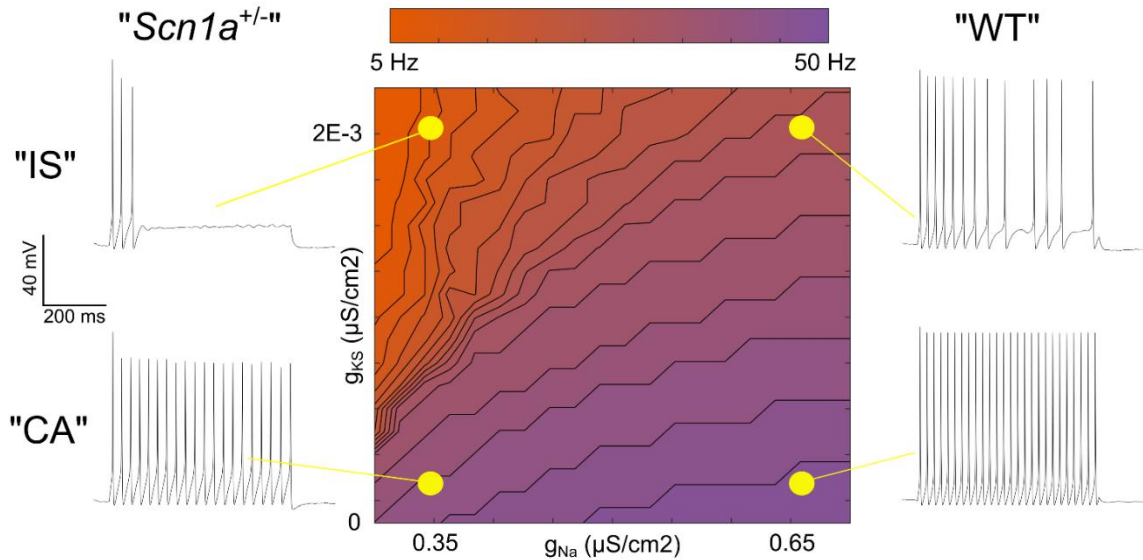


**Figure 8. Single compartment model of a VIP-IN illustrates the interaction between M-current and Na<sup>+</sup> current**

A single compartment Hodgkin-Huxley style conductance-based model using standard differential equations. Heat map indicates firing frequencies elicited with a 600 ms X 100 pA test pulse on a linear scale. The model was initially modified to approximate the intrinsic properties and firing rate of a typical WT CA VIP-IN observed experimentally. A slowly activating K<sup>+</sup> current with a fixed time constant (gKS) was then added to approximate the presence of M-current; in the presence of Gaussian distributed noise, this induced irregular spiking similar to that seen in IS VIP-INS (*top right*). Then, the amount of total Na<sup>+</sup> current density (gNa) in the model was varied. Models with low gNa and little or no gKS showed minimal impairment with a ~10-20% decrease in spike height and firing frequency. Models with low gNa and medium to high levels of gKS showed much more profound impairment, with complete collapse of repetitive action potential generation.

## DISCUSSION

### VIP-INs express Nav1.1 and are hypoexcitable in *Scn1a*<sup>+/-</sup> mice

VIP-INs exhibited impaired action potential generation in *Scn1a*<sup>+/-</sup> mice consistent with decreased Na<sup>+</sup> channel expression, and this deficit could be rescued with the Nav1.1-specific modulator Hm1a, supporting the presence of Nav1.1 subunit-containing Na<sup>+</sup> channels in VIP-INs. We found that these deficits were localized to a large subset of VIP-INs that exhibited irregular spiking (IS). This basic finding was consistent across cortical areas, and, importantly, was seen at early developmental time points (P18-21) as well as in juvenile/young adult mice (P30-55). Interestingly, Hm1a had a larger effect on IS VIP-INs than on PV-INs, consistent with the observation that IS VIP-INs may be more profoundly impaired than PV-INs in *Scn1a*<sup>+/-</sup> mice. This persistent VIP-IN dysfunction in *Scn1a*<sup>+/-</sup> mice is distinct from the time course of PV-IN dysfunction, which we previously found is transient and delimited to an early developmental period when assessed via the same approach (Favero et al, 2018). Such a time course is consistent with the known natural history of Dravet syndrome in human patients: it is well established that seizure frequency typically decreases during early childhood, while cognitive deficits remain, with moderate to severe intellectual disability and features, or a formal diagnosis of, autism spectrum disorder (Berkvens et al., 2015; Genton et al., 2011; Han et al., 2012; Li et al., 2011). As VIP-INs are considered to have a role as disinhibitory elements in cortical circuits, it might seem counterintuitive that such cells might be dysfunctional in an epilepsy syndrome; however, it may be the case that early epilepsy is driven by transient PV-IN abnormalities while cognitive impairment persists in part due to ongoing VIP-IN hypofunction.

## Two distinct firing patterns of VIP-INs revealed by response to long depolarization

Previous studies have demonstrated a diversity of VIP-IN electrophysiological properties that do not clearly correlate with other molecular and anatomical markers of VIP-INs (von Engelhardt et al., 2007; He et al., 2016; Kawaguchi and Kubota, 1997; Porter et al., 1998; Prönneke et al., 2015). We also observed a seemingly diverse range of firing patterns in VIP-INs that did not clearly correlate with anatomy or proposed VIP-IN molecular markers CR and CCK (Figure 5). Using the response to longer (8-10 sec) depolarizations, k-means clustering facilitated clear division into two electrophysiological groups, which we refer to as IS and CA VIP-INs (Figure 2; Porter et al., 1999), each of which comprise approximately 50% of VIP-INs in layer 2/3 in both barrel cortex and V1 at both P18-21 and P0-55. IS and CA firing patterns were robust to a variety of stimulation protocols, including a slow ramp current injection and prepulse step depolarization to inactivate T-type calcium currents that underlie burst firing in a subset of VIP-INs (Prönneke et al., 2020) (Figure 5-Figure supplement 1). Therefore, irregular spiking is distinct from, yet partially overlaps with, bursting. However, our data clearly indicated that brief current pulses on the order of hundreds of milliseconds (such as are standard in slice physiology experiments) cannot establish whether a VIP-IN is IS or CA, as many IS VIP-INs fire continuously for 600 ms or more prior to transition to an IS pattern. This distinction may be relevant for ongoing efforts to create a comprehensive classification of VIP-INs (Gouwens et al., 2018; He et al., 2016; Prönneke et al., 2015, 2020). It will be important to investigate the physiological relevance of differences in firing patterns identified in acute brain slice experiments and how this relates to the *in vivo* activity of VIP-INs. While the stimuli used here are very different than naturalistic stimuli in the intact organism, such experiments reveal details related to the complement



of ion channels expressed by VIP-INs as well as modulation by neurotransmitters that may be highly relevant *in vivo*.

### **M-current mediated by Kcnq5-containing K<sup>+</sup> channels regulates VIP-IN excitability and mediates response to cholinergic neuromodulation**

We divided VIP-INs into IS and CA cells based on the presence of an initial period of regular firing followed by a suppression of firing and subsequent irregular spiking (as defined by a high ISI coefficient of variation). This pattern suggested the expression of a slowly-activating potassium current such as M-current (Brown and Passmore, 2009). Transcriptomics data supports our finding that most VIP-INs express Nav1.1 and suggests that a subset of VIP-INs express the KCNQ channel subunit Kcnq5 (Paul et al., 2017; Tasic et al., 2016), which we confirmed with immunohistochemistry (Figure 6- Figure supplement 2). We hypothesized that M-current in IS VIP-INs drives this distinctive firing pattern, with CA VIP-INs express low levels of M-current that is insufficient to induce irregular firing. We were able to bidirectionally modulate VIP-IN firing patterns by pharmacologically blocking or enhancing M-current in IS and CA VIP-INs respectively, supporting this hypothesis. However, the level of M-current in CA VIP-INs appears to be small enough such that blocking M-current in these cells has no effect on their firing properties (Figure S11). Even though our classification highlighted prominent differences in excitability, most or all VIP-INs do appear to express some level of both Nav1.1 and Kcnq2/5. It is possible that the electrophysiological properties of VIP-INs defined here do not constitute clearly delimited 'subtypes' per se, but rather exist along a continuum of active properties which only partially overlap with molecular markers (such as CR and CCK) and morphology. Nevertheless, an irregular firing

pattern that can be modulated by cholinergic suppression of M-current appears to be a durable feature of ~50% of VIP-INs.

If Kcnq5 and Nav1.1 in VIP-INs have overlapping distributions of expression, how does *Scn1a* haploinsufficiency lead to selective dysfunction of IS VIP-INs? To address this, we constructed a single compartment model with a voltage-gated Na<sup>+</sup> conductance and M-type K<sup>+</sup> conductance to simulate the influence of superimposed M-current on neuronal excitability in the context of varied Na<sup>+</sup> current density. This modelling recapitulated several important characteristics of our data, including the diversity of VIP-IN firing patterns, the role of M-current in this diversity, and the interaction between Na<sup>+</sup> current and M-current. The model illustrates how loss of Nav1.1 could have drastically different effects in IS vs. CA VIP-INs based on electrophysiological context, such as the overall level of M-current and the degree of reliance on Nav1.1.

VIP-INs are recruited during shifts in attentional state, and their activity is important for the cortical state transition that occurs in response to cholinergic neuromodulation (Batista-Brito et al., 2017; Fu et al., 2014; Reimer et al., 2014; Walker et al., 2016). Our data suggests that cholinergic input may enhance VIP-IN excitability during cortical state transitions by inhibiting M-current. We found that, while application of carbachol depolarized both IS and CA VIP-INs, this manipulation selectively modulates IS VIP-IN excitability by inducing a switch from IS to tonic firing mode through muscarinic acetylcholine receptor activation. This effect may be important during shifts in attentional state, which are known to recruit VIP-IN activity. Our data also implies that IS VIP-IN dysfunction in *Scn1a*<sup>+/-</sup> mice may play a particularly important role in the activity of IS VIP-INs during such state changes. Overall, our findings identify a novel cellular

locus of dysfunction in Dravet Syndrome which may be relevant to both the epilepsy and the severe cognitive impairments characteristic of this disease.

## MATERIALS AND METHODS

<b>Table 1. Key Resources</b>				
Reagent type (species) or resource	Designation	Source or reference	Identifiers	Additional information
Genetic reagent ( <i>M. musculus</i> )	129S- <i>Scn1atm1Kea/Mmja</i> x	Jax	RRID:M MRRC_0 37107- JAX	Dr. Jennifer A. Kearney, Northwestern University
Genetic reagent ( <i>M. musculus</i> )	<i>Viptm1(cre)Zjh/J</i>	Jax	RRID:IM SR_JAX: 010908	
Genetic reagent ( <i>M. musculus</i> )	B6;129P2- <i>Pvalbtm1(cre)Arbr/J</i>	Jax	RRID:IM SR_JAX: 008069	
Genetic reagent ( <i>M. musculus</i> )	B6J.Cg- <i>Ssttm2.1(cre)Zjh/Mw</i> arJ	Jax	RRID:IM SR_JAX: 028864	
Genetic reagent ( <i>M. musculus</i> )	<i>Rosa- CAG-LSL- tdTomato</i>	Jax	RRID:IM SR_JAX: 007914	

Genetic reagent ( <i>M. musculus</i> )	129S6.SvEvTac	Taconic Biosciences	RRID:IM SR_TAC: 129sve	
Genetic reagent ( <i>M. musculus</i> )	C57BL/6J	Jax	RRID:IM SR_JAX: 000664	
Genetic reagent ( <i>M. musculus</i> )	Ccktm1.1(cre)Zjh/J	Jax	RRID:IM SR_JAX: 012706	Drs. Bernardo Rudy and Robert Machold, NYU
Genetic reagent ( <i>M. musculus</i> )	B6(Cg)-Calb2tm1(cre)Zjh/J	Jax	RRID:IM SR_JAX: 010774	Drs. Bernardo Rudy and Robert Machold, NYU
Genetic reagent ( <i>M. musculus</i> )	Viptm2.1(flpo)Zjh/J	Jax	RRID:IM SR_JAX: 028578	Drs. Bernardo Rudy and Robert Machold, NYU
Genetic reagent ( <i>M. musculus</i> )	B6.Cg-Gt(ROSA)26Sortm8 0.1(CAGCOP4*L132 C/EYFP)Hze/J	Jax	RRID:IM SR_JAX: 025109	Drs. Bernardo Rudy and Robert Machold, NYU
recombinant DNA reagent	AAV.CAG.Flex.tdTomato	Penn Vector Core	AV-9-ALL864	2XE+13 GC/mL

peptide, recombinant protein	Hm1a	Alomone	STH-601	1 $\mu$ M / 50 nM
chemical compound, drug	Biocytin conjugated to Alexa Fluor 488	Invitrogen	A12924	0.5%
chemical compound, drug	Linopirdine	Sigma	L134	50 $\mu$ M
chemical compound, drug	Retigabine	Alomone	D-23129	50 $\mu$ M
chemical compound, drug	Carbamoylcholine chloride	Sigma	C4382	5 $\mu$ M
chemical compound, drug	Muscarine	Sigma	M6532	5 $\mu$ M
chemical compound, drug	4-Acetyl-1,1- dimethylpiperaziniu m iodide	Tocris	0352	1 $\mu$ M

software, algorithm	Pclamp 10	Clampfit		V10.0
software, algorithm	Matlab	Mathworks		2019a
software, algorithm	Gramm	doi.org/10.2 1105/joss.0 0568		Data visualization for Matlab
Antibody	Anti-Nav1.1 sodium channel, clone K74/71	NeuroMab	75-023	1:500, IF
Antibody	KCNQ5 Polyclonal Antibody	Invitrogen	PA5- 77651	1:500, IF
Antibody	Anti-KCNQ3 Antibody	Alomone labs	APC-051	1:200, IF
Antibody	Goat anti-Mouse IgG1 Cross- Adsorbed Secondary Antibody, Alexa Fluor 488	Invitrogen	A-21121	1:1000, IF
Antibody	Goat anti-Rabbit IgG (H+L) Cross-	Invitrogen	A-11008	1:1000, IF

	Adsorbed Secondary Antibody, Alexa Fluor 488			
--	--	--	--	--



### *Experimental animals*

All procedures and experiments were approved by the Institutional Animal Care and Use Committee at the Children's Hospital of Philadelphia and were conducted in accordance with the ethical guidelines of the National Institutes of Health. Both male and female mice were used in equal proportions. After weaning at P21, mice were group-housed with up to 5 mice per cage and maintained on a 12-hour light/dark cycle with *ad libitum* access to food and water.

Mouse strains used in this study included: *Scn1a*<sup>+/-</sup> mice on a 129S6.SvEvTac background (RRID:MMRRC\_037107-JAX) generated by a targeted deletion of exon 1 of the *Scn1a* gene, VIP-Cre mice (Viptm1(cre)Zjh/J; RRID:IMSR\_JAX:010908 on a mixed C57BL/6;129S4 background), PV-Cre mice (B6;129P2-Pvalbtm1(cre)Arbr/J; RRID:IMSR\_JAX:008069), SST-Cre mice (B6J.Cg-Ssttm2.1(cre)Zjh/MwarJ; RRID:IMSR\_JAX: 028864), tdTomato reporter/Ai14 mice (Rosa- CAG-LSL-tdTomato; RRID:IMSR\_JAX:007914; on a C57BL/6J background), wild-type 129S6.SvEvTac (Taconic Biosciences model #129SVE; RRID:IMSR\_TAC: 129sve), and wild-type C57BL/6J (RRID:IMSR\_JAX:000664).

Homozygous VIP-Cre mice were crossed to homozygous Ai14 mice to generate VIP-Cre.tdT double heterozygotes on a predominantly C57BL/6J background. Female VIP-Cre.tdT double heterozygotes were then crossed to male 129S6.*Scn1a*<sup>+/-</sup> mice to generate *Scn1a*.VIP-Cre.tdT mice and WT.VIP-Cre.tdT littermate controls. The genotype of all mice was determined via PCR of tail snips obtained at P7 and was re-confirmed for each mouse after they were sacrificed for slice preparation. The same breeding scheme was used to generate *Scn1a*.PV-Cre.tdT (as in Favero et al, 2018). All mice used for

experiments were on a near 50:50 129S6:B6J background, and *Scn1a*<sup>+/-</sup> mice on this background have been shown to replicate the core phenotype of Dravet Syndrome (Miller et al., 2014; Mistry et al., 2014). We observed similar rates of spontaneous death (17/52, or 32%, of *Scn1a.VIP-Cre.tdT* mice not used for experiments by P55; Favero et al., 2018) and were able to thermally induce seizures in 100% (9/9) of P21-50 *Scn1a.VIP-Cre.tdT* mice at or below 42°C core body temperature, supporting the validity of using these mice as a tool to study VIP-IN function in Dravet Syndrome.

We used an intersectional genetic approach (He et al., 2016; Taniguchi et al., 2011) to target CCK and CR expressing VIP-INs. These mice were a cross between either CCK-Cre (*Ccktm1.1(cre)Zjh/J*; RRID: IMSR\_JAX:012706) or CR-Cre (*B6(Cg)-Calb2tm1(cre)Zjh/J*; RRID: IMSR\_JAX:010774) crossed to a VIP-Flp (*Viptm2.1(flpo)Zjh/J*; RRID: IMSR\_JAX:028578) and fluorescent reporter Ai80 (*B6.Cg-Gt(ROSA)26Sortm80.1(CAG-COP4\*L132C/EYFP)Hze/J*; RRID: IMSR\_JAX:025109).

#### *Stereotaxic injections*

In a subset of experiments at the P35-50 age, VIP-INs from double transgenic *Scn1a.VIP-Cre* and *WT.VIP-Cre* littermates from the cross described above were labeled via stereotaxic injection of AAV.CAG.Flex.tdTomato (Penn Vector Core, AV-9-ALL864) at approximately P25. Briefly, P25 mice were anesthetized with isoflurane (induction, 3-4%; maintenance, 1-1.5%) and body temperature and breathing were continuously monitored. A small craniotomy approximately 1 mm posterior and 3 mm lateral to bregma was made to allow insertion of a 50-75 µm tip diameter glass pipette driven by a Nanoject III (Drummond Scientific). 100 nL of 2XE+13 GC/mL of AAV9 diluted in sterile PBS was injected at 20 nL/min. The pipette was held in place for 10 min

to allow the virus to spread, and was then slowly removed; the scalp was sutured closed, and the mouse allowed to recover.

#### *Acute slice preparation*

Mice were anesthetized with isoflurane and transcardially perfused with ice cold artificial cerebral spinal fluid (ACSF) containing (in mM): NaCl, 87; sucrose, 75; KCl, 2.5; CaCl<sub>2</sub>, 1.0; MgSO<sub>4</sub>, 6.0; NaHCO<sub>3</sub>, 26; NaH<sub>2</sub>PO<sub>4</sub>, 1.25; glucose, 10, and equilibrated with 95% O<sub>2</sub> and 5% CO<sub>2</sub>. The brain was removed to cold ACSF, then mounted on a holder of the Leica VT-1200S vibratome and sliced at 300-350 µm thickness. Slices were allowed to recover for 30 minutes in ACSF warmed to 30°C, then maintained at room temperature for up to 6 hours before recording. Slices were transferred to a recording chamber on the stage of a BX-61 upright microscope and continuously perfused with recording solution at 30-32° C and 3 mL/min that contained, in mM: NaCl, 125; KCl, 2.5; CaCl<sub>2</sub>, 2.0; MgSO<sub>4</sub>, 1.0; NaHCO<sub>3</sub>, 26; NaH<sub>2</sub>PO<sub>4</sub>, 1.25; glucose, 10.

#### *Slice recordings*

VIP-INs and PV-INs were identified by tdT expression visualized with epifluorescence. Pyramidal cells were identified by morphology under infrared differential interference contrast (IR-DIC) and the presence of a regular-spiking firing pattern. Whole-cell recordings were obtained from superficial (layer 2/3) primary somatosensory cortex (S1; “barrel”) and visual cortex (V1) with between 1 – 4 (usually 1 or 2) cells recorded from each slice in either single or paired configuration. Patch pipettes were pulled from borosilicate glass using a P-97 puller (Sutter Instruments) and filled with intracellular solution containing (in mM): K-gluconate, 130; KCl, 6.3; EGTA, 0.5; MgCl<sub>2</sub>, 1.0; HEPES, 10; Mg-ATP, 4.0; Na-GTP, 0.3; pH was adjusted to 7.30 with KOH, and

osmolarity adjusted to 285 mOsm with 30% sucrose. Where indicated, intracellular solution also contained 0.5% biocytin conjugated to Alexa Fluor 488 (Invitrogen) for 2P imaging. Pipettes had a resistance of 4-6 M $\Omega$  when filled and placed in recording solution. Voltage was sampled at 50 kHz with a MultiClamp 700B amplifier (Molecular Devices), filtered at 10 kHz, digitized using a DigiData 1550A, and acquired using pClamp10 software. Recordings were discarded if the cell had an unstable resting membrane potential and/or a membrane potential greater than -50 mV, or if access resistance increased by > 20% during the recording. We did not correct for liquid junction potential.

#### *Electrophysiology data analysis*

All analysis was performed blind to genotype using custom written Matlab (Mathworks) code with quality control using manual confirmation in Clampfit (pCLAMP). Resting membrane potential ( $V_m$ ) was calculated using the average value of a 1 s sweep with no direct current injection. Input resistance ( $R_m$ ) was calculated using the average response to small hyperpolarizing current injections near rest using  $R_m = \Delta V/I$  for each sweep. AP threshold was calculated as the value at which the derivative of the voltage ( $dV/dt$ ) first reached 10 mV/ms. Spike height refers to the absolute maximum voltage value of an individual AP, while spike amplitude was calculated as the difference between spike height and AP threshold for a given AP. AP rise time is the time from AP threshold to the peak of the AP. AP half-width (AP 1/2-width) is defined as the width of the AP (in ms) at half-maximal amplitude (half the voltage difference between the AP threshold and peak). AP afterhyperpolarization (AHP) amplitude is calculated as the depth of the afterhyperpolarization (in mV) relative to AP threshold. Unless indicated, all

quantification of single spike properties was done using the first AP elicited at rheobase (below).

Rheobase was determined as the minimum current injection that elicited APs using a 600 ms sweep at 10 pA intervals. Maximal instantaneous firing was calculated using the smallest interspike interval (ISI) elicited at near-maximal current injection. Maximal steady-state firing was defined as the maximal mean firing frequency during the last 300 ms of a suprathreshold 600 ms current injection, with a minimum requirement for a spike being an amplitude of 40 mV with a clear AP threshold (above) and height overshooting at least -10 mV. We found the combination of these two measures to best describe VIP-IN firing rates, as some cells fired a very brief burst of APs at high frequency, while others fired continuously with little or no initial bursting. All *I*-*f* plots were created using the steady-state firing calculated for each current step, counting failures as 0 for subsequent current steps. Population raster plots were constructed by taking a 20 ms sliding average of the instantaneous firing rate for each current step and averaged over each group of cells.

#### *Firing pattern classification*

We used a longer depolarizing current injection (generally, 8-10 s) which was found to highlight features of VIP-IN firing that were not apparent with briefer, 600 ms current injections. The coefficient of variation of the ISI (ISI CoV) was used to quantify irregularity of repetitive AP discharge, and was defined as the standard deviation divided by the mean of all ISI's from a single 8 s or 600 ms sweep at 2-times rheobase current injection. The burst length of a cell was defined by taking the time of the last spike occurs prior to an abrupt cessation of firing lasting > 150 ms. This value was determined

in an unbiased way by taking the mean + 2-times standard deviation of all ISI values from our data set. We used the same cutoff to calculate an “apparent” burst length when using data from 600 ms sweeps. We used k-means clustering with  $n = 2$  groups to cluster VIP-INs from both WT and *Scn1a<sup>+/-</sup>* mice using the variables of ISI CoV and burst length from 8 s current injections at 2-times rheobase. Clustering was validated with > 95% agreement with blind manual classification when dividing cells based on the provided description of continuous firing with spike frequency adaptation (“CA”) versus initial burst followed by irregular spiking (“IS”). It was not possible to use 600 ms sweeps alone to replicate these two groups, either with k-means clustering of electrophysiological properties or manual classification.

#### *Voltage clamp recordings of acutely dissociated cells*

We performed voltage clamp recordings from acutely dissociated cells prepared from neocortex of P18 WT.VIP-Cre.tdT mice. Briefly, the mouse brain was extracted into ice cold ACSF as described above. Then, 400  $\mu\text{m}$  slices were cut on a vibratome, and the neocortex was manually separated from the underlying white matter using a scalpel. All neocortical sections were simultaneously place in dissociation media (Earl’s balanced salt solution (EBSS)) with (in mM): NaCl, 117; KCl, 5.0;  $\text{NaHCO}_3$ , 26;  $\text{NaH}_2\text{PO}_4$ , 1.0;  $\text{CaCl}_2$ , 1.0;  $\text{MgSO}_4$ , 4.0; HEPES, 20; glucose, 10, equilibrated with 95%  $\text{O}_2$ :5%  $\text{CO}_2$ , and pH adjusted to 7.4 with NaOH. This was supplemented with 0.1% trypsin (Sigma), 1 mg/mL collagenase (Sigma), 100 U/mL DNase1 (Sigma), and incubated for 10 min at 35° C. Dissociation was quenched by pouring the contents into a large volume of room temperature ACSF, and the neocortical sections were maintained for up to 4 hours. Prior to recording, individual sections were manually dissociated by triturating with a series of fire-polished glass pipettes decreasing in size, then immediately plated on a glass

coverslip coated in poly-D lysine (Sigma). Cells were allowed to settle and adhere for 10 min, then the ACSF was exchanged for recording solution containing (in mM): NaCl, 135; KCl, 4; CaCl<sub>2</sub>, 2; MgCl<sub>2</sub>, 2; HEPES, 10; Glucose, 10; TEA-Cl, 10; CdCl<sub>2</sub>, 0.1; with pH adjusted to 7.4 with NaOH. VIP-INs were identified with epifluorescence. Cells were recorded with patch pipettes with a resistance measured at 2.5-3.0 MΩ containing (in mM): NaF, 10 CsF, 110; CsCl, 20; EGTA, 2; HEPES, 10; with pH adjusted to 7.4 with KOH. Na<sup>+</sup> currents were recorded in cells that were stable and had an access resistance < 10 MΩ for 5 minutes after break in using a series of 100 ms voltage steps from -80 to 50 mV. Peak current was calculated as the max absolute value of the current response. Persistent current was calculated as a percentage of transient current using the mean current during the period between 80 and 100 ms after the initial voltage step. The time constant of inactivation (tau) was calculated by fitting a double exponential to the decay of the Na<sup>+</sup> current, reporting the value for the dominant term. All values in Figure 4 were calculated using the current elicited at 0 mV.

### *Immunohistochemistry*

To facilitate staining of Nav1.1 at the AES, we used very mild fixation (1% paraformaldehyde with 0.5% MeOH in PBS) described previously (Alshammari et al., 2016). Briefly, isoflurane-anesthetized mice were transcardially perfused; brains were removed and post-fixed in perfusate at RT for 1 hour. We then immediately cut 50 μm sections on a Leica VT-1200S vibratome, and then blocked and permeabilized the slices with 0.5% Triton X-100 (Sigma) and 10% normal goat serum in PBS for one hour at RT. We stained overnight at 4° C with a primary antibody directed against Nav1.1 (NeuroMab K74/71) in PBS with 3% bovine serum albumin (BSA, Sigma) and 0.5% Triton X-100. The following day, the slices were washed with PBS and stained with a

secondary antibody, Alexa Fluor 488-conjugated goat anti-mouse IgG1 (Molecular Probes), in PBS, with 3% BSA and 0.5% Triton X-100. After washing, slides were coverslipped and sealed before imaging on a Leica TCS SP8 confocal microscope. We examined VIP-INs under 80X magnification and detected Nav1.1 signal on very fine (0.5  $\mu\text{m}$ ) processes emanating from either the cell body or proximal dendrite. We used a cutoff of mean + 2-times the standard deviation of the Nav1.1 signal measured using repeated line scans on at least 5  $\mu\text{m}$  (consecutive) of tdT-positive VIP-IN processes to define a “positive” VIP-IN axon. For verification of Nav1.1 antibody specificity, we generated several *Scn1a*<sup>-/-</sup> mice by breeding two *Scn1a*<sup>+/-</sup> mice. For Kcnq3/5 staining, we used standard 4% paraformaldehyde, then performed staining as described above.

#### *Allen Brain data access*

Data was accessed directly from: © 2015 Allen Institute for Brain Science. Allen Cell Types Database. Available from: [celltypes.brain-map.org/rnaseq](http://celltypes.brain-map.org/rnaseq). This data represents over 20,000 cells pooled from primary mouse visual cortex (V1) and anterior lateral motor cortex (ALM). The provided RNA-Seq Data Navigator was used to restrict data selection to pyramidal cells and VIP-INs from layer 2/3 to match our experimental data. SST and PV-INs from all layers were also included as a reference. *ScnXa*, *KcnqX*, *Cck*, and *Calb2* expression levels were downloaded in February 2019 from the indicated cell types for offline analysis and plotting using Matlab.

#### *Slice pharmacology*

We used several pharmacological agents including Hm1a (Alomone Labs STH-601), linopirdine (Sigma L134), retigabine (Alomone D-23129), the cholinomimetic carbamoylcholine chloride (carbachol; Sigma C4382), muscarine (Sigma M6532), and



the nicotinic agonist 4-Acetyl-1,1-dimethylpiperazinium iodide (Tocris 0352). Hm1a, muscarine, and 4-Acetyl-1,1-dimethylpiperazinium iodide were dissolved in deionized water, aliquoted, and frozen at -20° C. Carbachol was stored as a powder at RT, and both linopirdine and Retigabine were stored as 100 mM stock solutions in DMSO (Sigma) aliquoted in -20°C. For pharmacological experiments in which drug was dissolved in DMSO, the same concentration of DMSO was present in control external solution. After a baseline recording, drugs were perfused in at 3 mL/min while continuously recording membrane potential; repeat measurements were performed 10 minutes after wash-in. A subset of cells were recorded for up to 1 hour following washout of each drug, as needed in some cases to observe complete or near-complete washout. For experiments using carbachol, repeat measurements were made 5 minutes after wash-in.

### *2-P imaging and morphological reconstruction*

Where indicated, internal solution contained 0.5% biocytin conjugated to Alexa Fluor 488, or, in some cases, 50 mM Alexa Fluor alone. After obtaining the whole cell configuration, the cell was dialyzed for at least 20 minutes; then, the pipette was slowly removed to allow for the cell to reseal. Two-photon (2P) imaging was performed using a customized Bruker 2P microscope system with a MaiTai DeepSee Ti:Sapphire pulsed infrared laser (SpectraPhysics) directed through a modified Olympus BX-61 base equipped with a GaAsP photodetector (Hamamatsu). 3D image stacks were reconstructed using the built in ImageJ plugin Simple Neurite Tracer and compressed to a 2D trace which was analyzed using Matlab. We used “vertical bias” as a summary statistic to capture the difference between bipolar and multipolar morphologies. We quantified the total length of dendrite that fell within 30° of vertical (i.e., a line

perpendicular to the pial surface), and then normalized to the total length of dendrite.

Using this method, bipolar cells had a vertical bias close to 1, while multipolar cells with processes extending in all directions had vertical bias ranging from near-zero to close to 0.5.

### *Hodgkin-Huxley VIP-IN model*

All simulations were done using custom Matlab code available upon request. We used classic Hodgkin-Huxley equations with the single addition of a slow K<sup>+</sup> conductance,  $g_{KS}$ , as in Stiefel et al. (2013). Here, we are using the additional slowly activating  $g_{KS}$  to model in a generic fashion the effects of M-current mediated irregular spiking in VIP-INs. The equations for our model are

$$\frac{c_m dV}{dt} = g_{leak}(E_l - V) + m^3 h g_{Na}(E_{Na} - V) + n^3 g_{KDR}(E_K - V) + s g_{KS}(E_K - V) + I_{inj} + I_{noise}$$

where  $V$  is the membrane voltage,  $m$  and  $h$  are the activation and inactivation states of the voltage-gated Na<sup>+</sup> conductance,  $n$  is the activation variable of the delayed-rectifier K<sup>+</sup> conductance, and  $s$  is the activation variable of the slow K<sup>+</sup> conductance. These variables are determined by the set of differential equations:

$$\frac{\tau_m dm}{dt} = m_{inf} - m$$

$$\tau_m = 1/(\alpha + \beta)$$

$$m_{inf} = \alpha/(\alpha + \beta)$$

The equations for  $h$ ,  $n$ , and  $s$  all have the same form. For  $m$ , the expressions for  $\alpha$  and  $\beta$  are given by

$$\alpha = 0.1(V + 38)/(1 - \exp(-(V + 38)/10))$$

$$\beta = 4 \exp(-(V + 65)/17)$$

For  $h$ , the expressions for  $\alpha$  and  $\beta$  are given by

$$\alpha = 0.05 \exp(-(V + 55)/20)$$

$$\beta = 1/((\exp(-(V + 35)/10) + 1)$$

For  $n$ , the expressions for  $\alpha$  and  $\beta$  are given by

$$\alpha = 0.01(V + 55)/(1 - \exp(-(V + 55)/10))$$

$$\beta = 0.125 \exp(-(V + 65)/80)$$

The expressions for  $s$  have a fixed  $\tau_s = 300$  ms and

$$s_{\text{inf}} = 1/(1 + \exp(-(V + 35)/5))$$

We manually fit the parameters of this model to resemble some of the key characteristics of VIP-INs, including a high input resistance (small  $g_{\text{leak}}$ ) and small size (small  $c_m$ ), as well as the approximate  $I$ - $f$  curves generated by simulated current injections ( $I_{\text{inj}}$ ). The conductances used were  $g_{\text{leak}} = 0.03 \text{ mS} \cdot \text{cm}^{-2}$ ,  $g_{\text{KDR}} = 5 \text{ mS} \cdot \text{cm}^{-2}$ ,  $g_{\text{Na}} = 65 \text{ mS} \cdot \text{cm}^{-2}$ ,  $g_{\text{KS}} = 2 \text{ mS} \cdot \text{cm}^{-2}$  where we varied  $g_{\text{Na}}$  and  $g_{\text{KS}}$  as described in Figure 8. The reversal potentials were  $E_{\text{Cl}} = -70$ ,  $E_{\text{K}} = -70$ , and  $E_{\text{Na}} = 50$ . Numerical integration was performed using the forward Euler method. We injected  $I_{\text{noise}}$  throughout the simulation as a Gaussian white distribution with a max amplitude of 10 pA.

#### *Statistics and experimental design*

Data from 62 total mice were used in this study for comparing intrinsic properties between WT and *Scn1a*<sup>+/-</sup> mice. A total of  $n = 57$  VIP-INs from P18-21 and  $n = 86$  VIP-INs from P30-55 WT mice, and  $n = 41$  VIP-INs from P18-21 and  $n = 61$  VIP-INs from P30-55 *Scn1a*<sup>+/-</sup> mice were included. We validated our core findings in a subset of experiments in primary visual cortex, with a total of  $n = 28$  VIP-INs from 4 WT.VIP-Cre.tdT mice and  $n = 28$  VIP-INs from 6 *Scn1a*.VIP-Cre.tdT mice age P18-21. All data were tested for normal distribution by performing a Shapiro-Wilk test and variances were estimated using Levene's test. Generally, intrinsic properties from WT and *Scn1a* VIP-INs had equal variances but occasional non-normal distributions. Thus, electrophysiological data were compared with Mann-Whitney U test for comparisons between two groups and Kruskal-Wallis test with a post hoc Dunn's test when comparing more than two groups. We observed no statistical difference between intrinsic properties of P18-21 and P30-55 WT VIP-INs and thus did not incorporate a model to account for changes in development (as in Favero et al., 2018). Therefore, we combined ages for

most of our analysis. Between 3-10 cells were recorded per mouse. For most comparisons, each cell as treated as an  $n$ , but we confirmed all main findings via reanalysis with each animal as an  $n$  (Figure 3 – Figure supplement1). For active properties that involved repeated measures, such as current/frequency plots and spike rundown with repeated APs, we used a multivariate ANOVA to compare between two groups, with post hoc Bonferroni correction to estimate  $p$  values for each measurement. For pharmacology experiments, a paired student's t-test was used to test for the effect of a drug within a single group. All statistical analysis was performed using custom written Matlab scripts. Data was visualized using built in Matlab functions, or using the gramm suite (Morel, 2018).

## SUPPLEMENTAL FIGURES

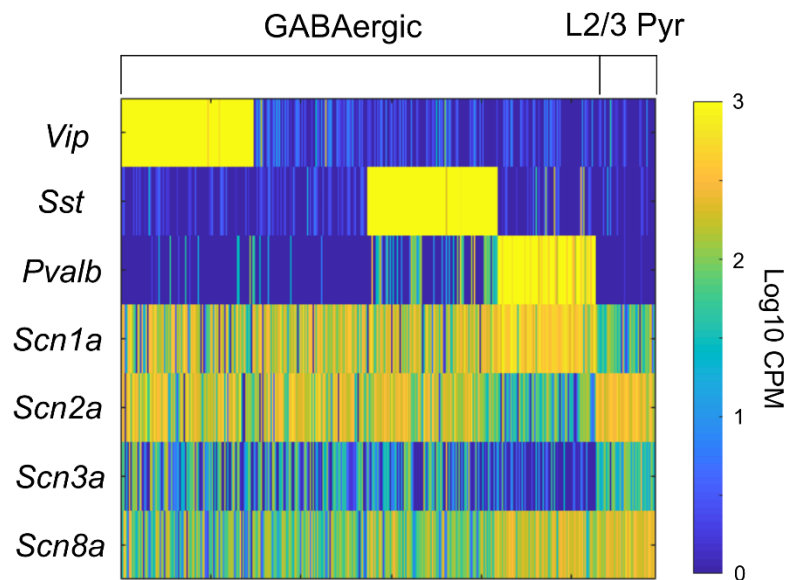


### Figure S1. *Scn1a* expression in VIP-INS

A) Data from the Allen cell types database, [celltypes.brain-map.org/rnaseq](http://celltypes.brain-map.org/rnaseq) which includes 14,249 cells from the primary visual cortex and 9,573 cells from the anterior lateral motor cortex (see Methods). Heat map indicating *ScnXa* RNA transcript levels in counts per million (CPM) for *all* GABAergic neurons and excitatory pyramidal cells in layer 2/3. Each vertical bar represents a single cell. Data was sorted based on expression of *Vip*, *Sst*, and *Pvalb* (PV). *Scn1a* is expressed in all GABAergic INs, including VIP-INS, with highest expression in PV-INS. PV-INS also express *Scn8a* at higher levels than *Scn2a*, while other INs preferentially express *Scn2a* in addition to *Scn1a*. Pyramidal neurons show highest expression of *Scn2a* and *Scn8a*, with relatively limited expression of *Scn1a* and *Scn3a*.

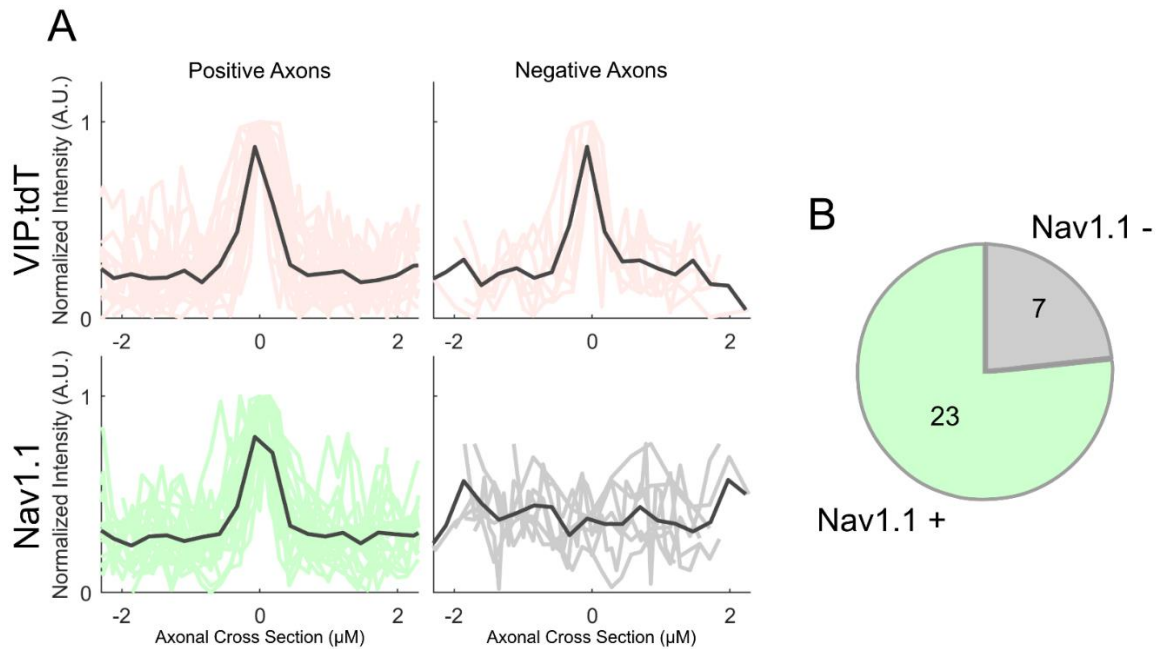


**Figure S2. Localization of Nav1.1 on VIP-IN axons.**

- A) tdT and Nav1.1 signals were measured through a cross sectional line-scan of 30 VIP-IN axons from  $n = 3$  adult WT.VIP-Cre.tdT mice, and divided into positive and negative axons based on a cutoff of the mean + 2 SD of the Nav1.1 signal level. Each signal is normalized individually to the max fluorescent intensity within each line scan. Axons were determined by morphological criteria, having a thin ( $0.5 \mu\text{M}$ ) profile and large branching angles.
- B) Proportions of VIP-INS that had positive (23/30; 77%) and negative (7/30; 23%) Nav1.1 expression on an identifiable axon. All “negative” VIP-INS are from the same field of view as at least one “positive” VIP-IN.

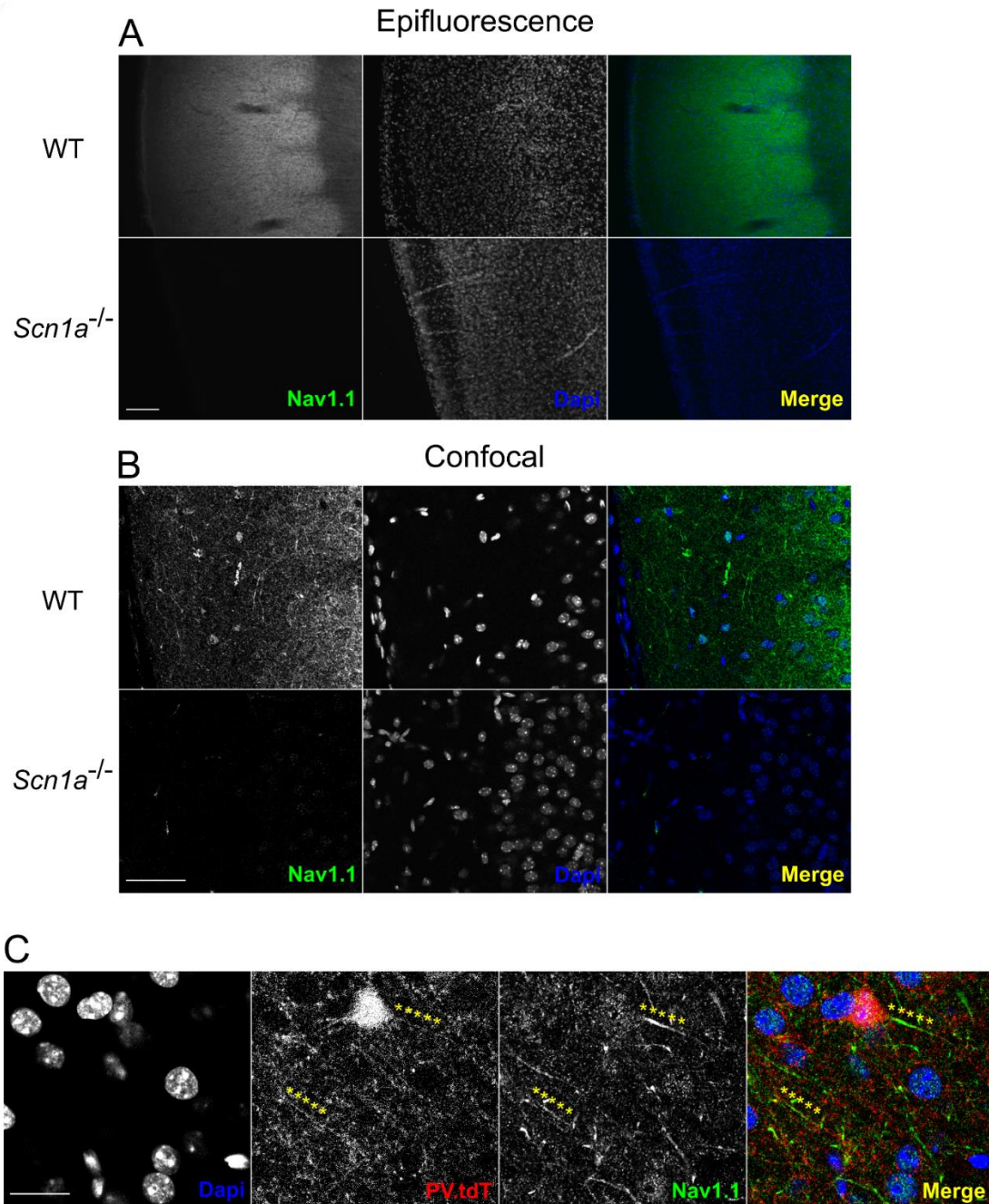


**Figure S3. Validation of Nav1.1 staining.**

A) Epifluorescence photomicrographs depicting Nav1.1 immunohistochemistry in a representative adult WT and P13 *Scn1a*<sup>-/-</sup> mouse. Nav1.1 signal is most intense in layer 4 of the barrel cortex. There is no detectable signal in *Scn1a* mice using



- identical conditions. Note the apparent difference in Dapi staining is due to the age difference between WT and *Scn1a*<sup>+/-</sup> samples. Scale bar = 100 μM.
- B) Confocal microscopy of the same experiment as in A. Nav1.1 signal in layer 2/3 is more sparse than in layer 4, but many individual processes can be resolved. Essentially no signal is present in the *Scn1a*<sup>-/-</sup> sample. Scale = 50 μM. For A and B, images are representative of  $n = 3$  mice for each group with at least two technical replicates for each animal.
- C) Nav1.1 immunohistochemistry in a WT.PV-Cre.tdT mouse showing co-labeling of Nav1.1 on a layer 4 PV-IN axon initial segment, as well as at a distal (presumptively nodal) portion of a PV-IN axon. Scale = 10 μM.

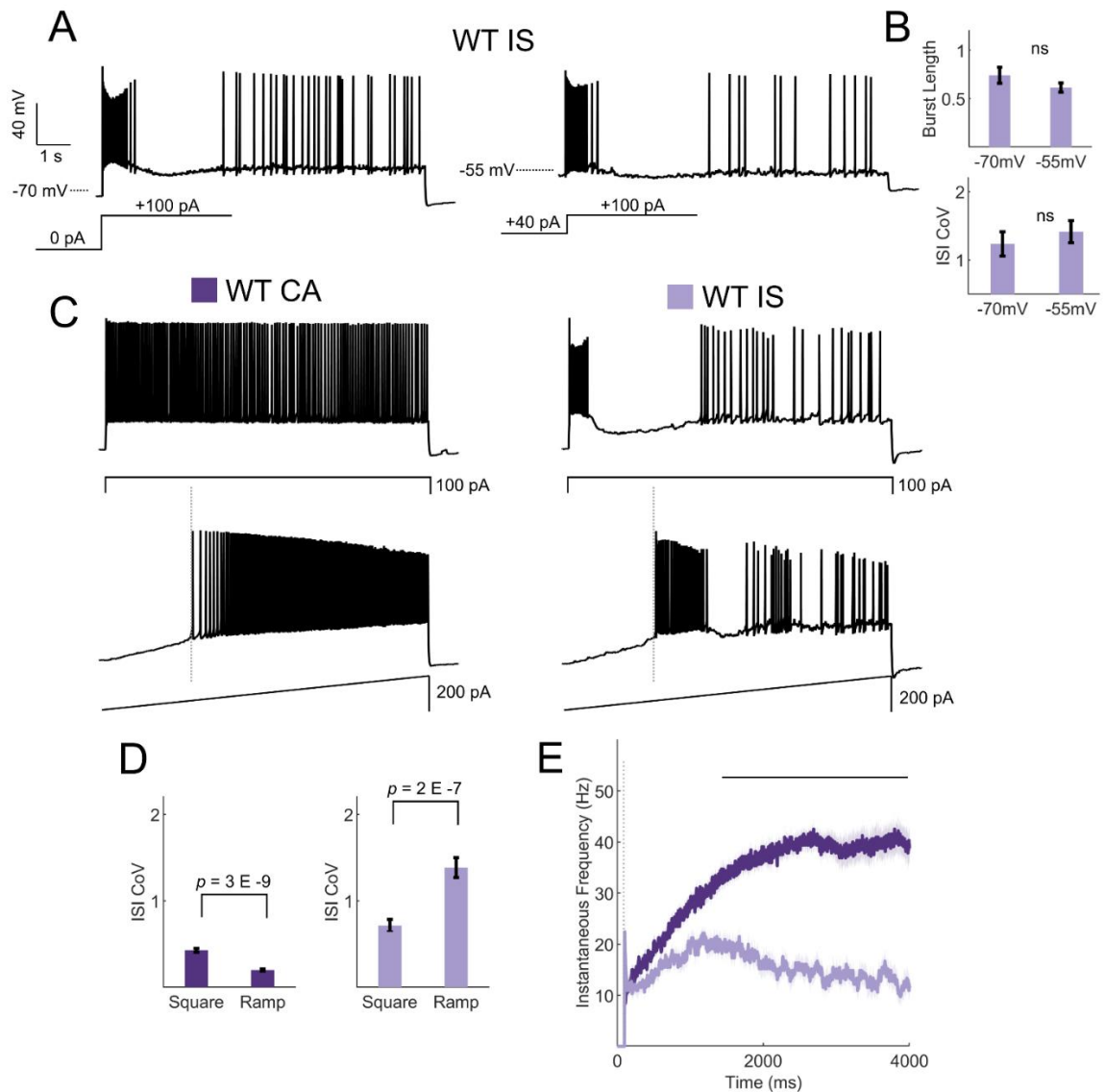


**Figure S4. IS VIP-IN firing patterns are robust to a variety of stimulation methods**

A) Shown is the firing pattern elicited in response to an 8-second square depolarization from an IS VIP-IN. When the resting membrane potential is depolarized with a DC offset (to -55 mV), IS VIP-INS show nearly identical firing patterns to that seen in response to suprathreshold stimulation from rest.

- B) Quantification of firing patterns of  $n = 16$  WT IS VIP-INs from 8 mice shows no change in either the initial burst length or the ISI CoV in response to prepulse depolarization.
- C) Example traces from a CA VIP-IN and IS VIP-IN in response to either a square 8-second current injection or a slow ramp injection with max amplitude of 200 pA. IS VIP-INs were equally distinguishable using ramp current injections.
- D) Quantification of the measured ISI CoV using either a square or ramp current injection. CA VIP-INs had a smaller ISI CoV (more regular) with ramp currents, while IS VIP-INs fired with an even more irregular pattern;  $p$ -values determined by paired student's  $t$ -test.  $n = 33$  IS VIP-INs from 13 mice and  $n = 32$  CA VIP-INs from 11 mice.
- E) Quantification of the instantaneous firing frequency during ramp current injections to 200 pA calculated with a 20 ms sliding average and aligned to the onset of firing for each cell (dashed line in C and E). CA VIP-INs show a typical saturating input/output relationship, while IS VIP-INs show highly non-linear responses, often with initial bursting. Line and shaded area represent mean  $\pm$  SEM, and bar indicates significance at  $p < 0.001$  by a multivariate ANOVA and post hoc Bonferroni test.

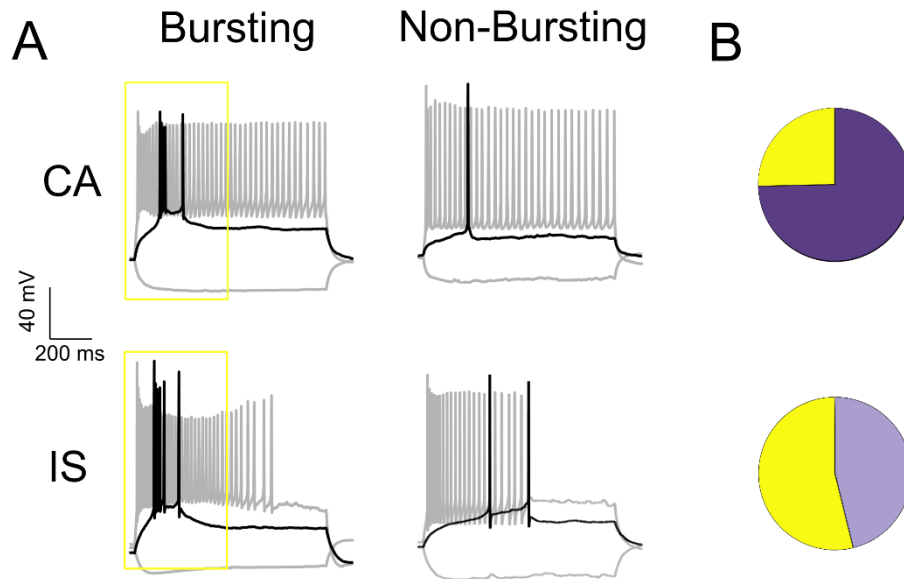


**Figure S5. A subset of both CA and IS VIP-INs show bursting at rheobase**

- A) Examples of CA and IS VIP-INs with and without bursting at rheobase with an intra-burst frequency > 100 Hz. Black trace indicates response to a rheobase current injection, and gray to a 3X rheobase suprathreshold current injection.
- B) Relative proportions of CA (18/71) and IS (42/78) VIP-INs in WT.VIP-Cre.tdT mice that are bursting at rheobase (*yellow* = bursting,  $p < 0.001$  via chi-square test).

Subtype	CA		IS		p- value (group)
	WT	Scn1a <sup>+/-</sup>	WT	Scn1a <sup>+/-</sup>	
n mice (cells)	30(71)	20(43)	32(78)	22(66)	
Age (days)	33.7 ±1.9	33.5 ±2.6	33.4 ±2.0	34.0 ±2.4	0.8
V <sub>m</sub> (mV)	-66.3 ±1.0	-65.2 ±1.0	-65.6 ±0.8	-64.0 ±0.6	0.3
R <sub>m</sub> (MΩ)	355 ±16	391 ±21	344 ±17	314 ±11	0.2
Time Constant (ms)	9.17 ±0.9	9.98 ±1.0	10.7 ±1.5	10.1 ±0.9	0.2
Rheobase (pA)	48.3 ±3.2	45.4 ±4.1	53.5 ±3.6	57.7 ±4.2	0.2
AP Threshold (mV)	-41.8 ±0.5	-41.5 ±0.5	-41.2 ±0.5 *	-39.1 ±0.4	0.01
AP Rise Time (ms)	0.45 ±0.01	0.46 ±0.01	0.44 ±0.01	0.44 ±0.01	0.1
Max Rise Slope (mV/ms)	418 ±14	417 ±13	427 ±17	371 ±15	0.1
AP Halfwidth (ms)	0.55 ±0.02	0.54 ±0.02 †	0.50 ±0.02	0.49 ±0.02	0.04
AP Amplitude (mV)	79 ±1.3	80 ±1.2	78 ±1.6 *	71 ±1.8	0.004
AHP Amplitude (mV)	10.0 ±0.63	10.9 ±0.55	10.6 ±0.55	11.0 ±0.43	0.6
AHP time (ms)	1.75 ±0.16	1.76 ±0.21	1.51 ±0.14	1.41 ±0.11	0.09
Sag (percent)	14.4 ±1.3	16.3 ±1.5 †	23.5 ±2.6	28.0 ±2.0	8 E -5
APs at Rheobase	1.38 ±0.1	1.32 ±0.1 †	2.41 ±0.3	2.01 ±0.2	7 E -5
Instantaneous (Hz)	237 ±11	235 ±13	245 ±10	209 ±11	0.1
Steady-State (Hz)	81 ±4	81 ±4 †	55 ±4 **	25 ±3	2 E -12
ISI CoV	0.30 ±0.02	0.31 ±0.02 †	0.61 ±0.03	0.69 ±0.04	4 E -13

\* p <0.05 vs. age and subtype matched wild-type; \*\* p <0.01; \*\*\* p <0.001.

† p <0.05 between CA and IS subtypes (consistent between WT and Scn1a<sup>+/-</sup>)

Listed p- values indicate result of a Kruskal Wallis test.

Pairwise comparisons are with Dunn's test.

All comparisons are made considering the average of each mouse as n =1.

**Table 2 (S1). Properties of VIP-INs from Scn1a<sup>+/-</sup> and WT littermates**

## Barrel Cortex

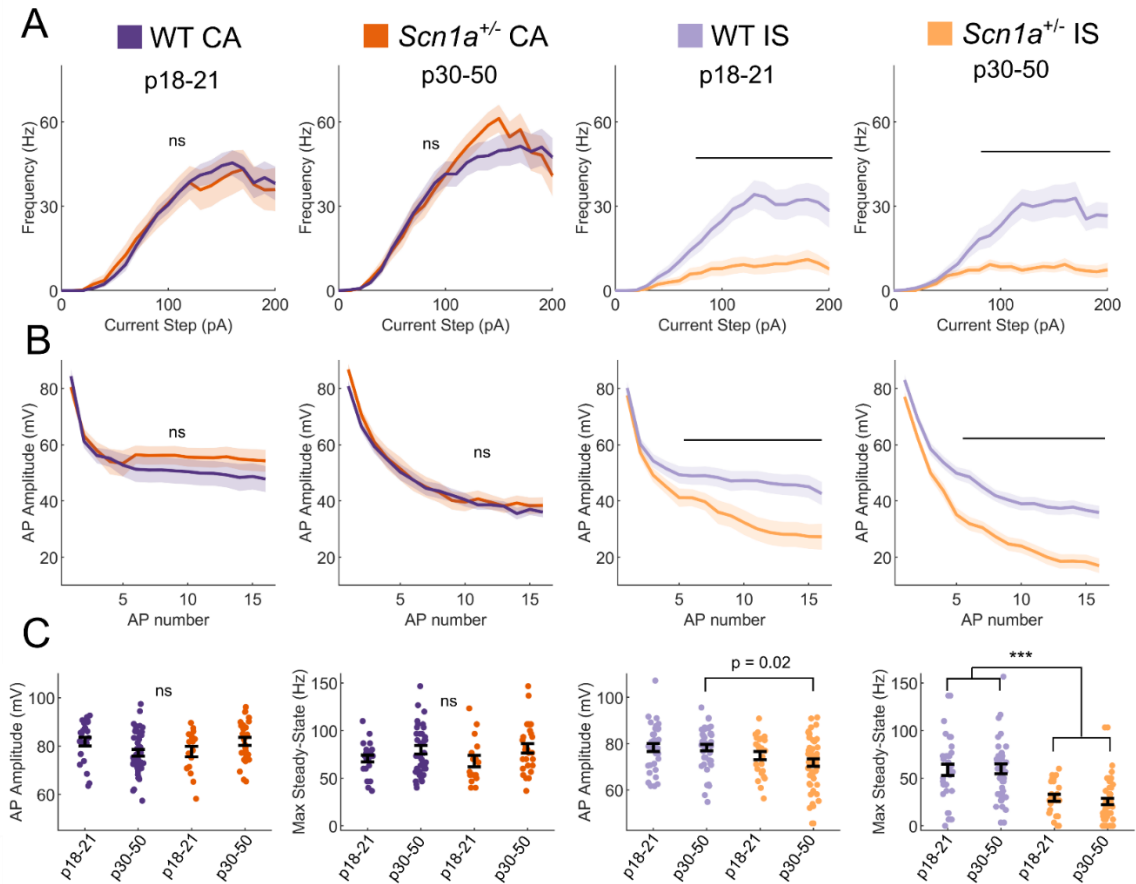


**Figure S6. IS VIP-IN deficits in *Scn1a*<sup>+/-</sup> mice are consistent across development.**

A) IF curves of CA and IS VIP-INs in the two indicated age ranges. Line and area represent mean  $\pm$  SEM, and bar indicates  $p < 0.01$  by a multivariate ANOVA and post hoc Bonferroni test.

B) Spike amplitude rundown of the same groups in A. Amplitude of repeated action potentials was measured at 3X rheobase for each cell. Line and area represent mean  $\pm$  SEM, and bar indicates  $p < 0.01$  by a multivariate ANOVA and post hoc Bonferroni test.

C) Individual cells (*dots*) and population mean  $\pm$  SEM (error bar);  $p$  values determined by a Kruskal-Wallis with post hoc Dunn's test; \*\*\*,  $p < 0.001$ . For A-C,  $n = 23|42$

(P18|P30) CA and 34|44 (P18|P30) IS cells from 32 WT mice, and  $n = 17|27$  (P18|P30) CA and  $n = 24|50$  (P18|P30) IS cells from 23 *Scn1a*<sup>+/-</sup> mice, were included.

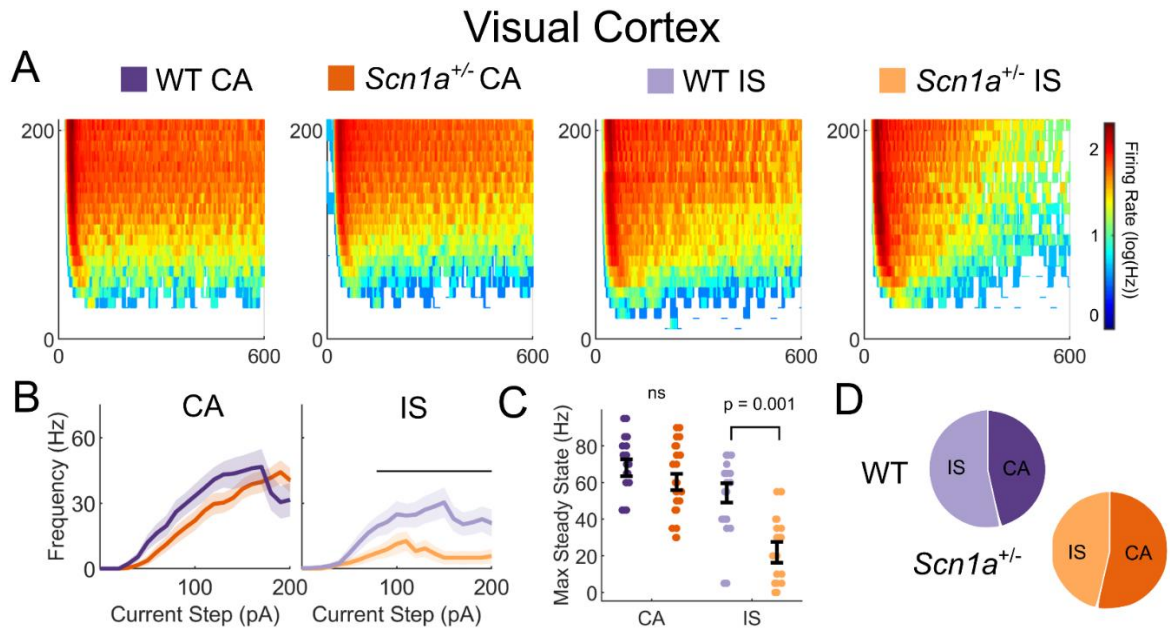


**Figure S7. IS VIP-IN deficits in *Scn1a*<sup>+/-</sup> mice are consistent across cortical areas**

- A) Heat maps of VIP-IN from primary visual cortex (V1) firing in response to 600 ms test pulses at 10 pA increments (compare to Figure 3Aiii).
- B) IF curves of CA and IS VIP-INs from V1 showing near identical results to barrel cortex. Line and area represent mean ± SEM, and bar indicates significance at  $p < 0.05$  by a multivariate ANOVA and post hoc Bonferroni test.
- C) Individual cells (dots) and population mean ± SEM (error bar); p values determined by a Kruskal-Wallis with post hoc Dunn's test.
- D) Relative proportions of CA and IS cells in V1 (compare to Figure 2E). A total of  $n = 13$  CA and 15 IS VIP-INs from 4 WT.VIP-Cre.tdT mice and  $n = 15$  CA and 13 IS VIP-INs from 6 *Scn1a*.VIP-Cre.tdT mice were included



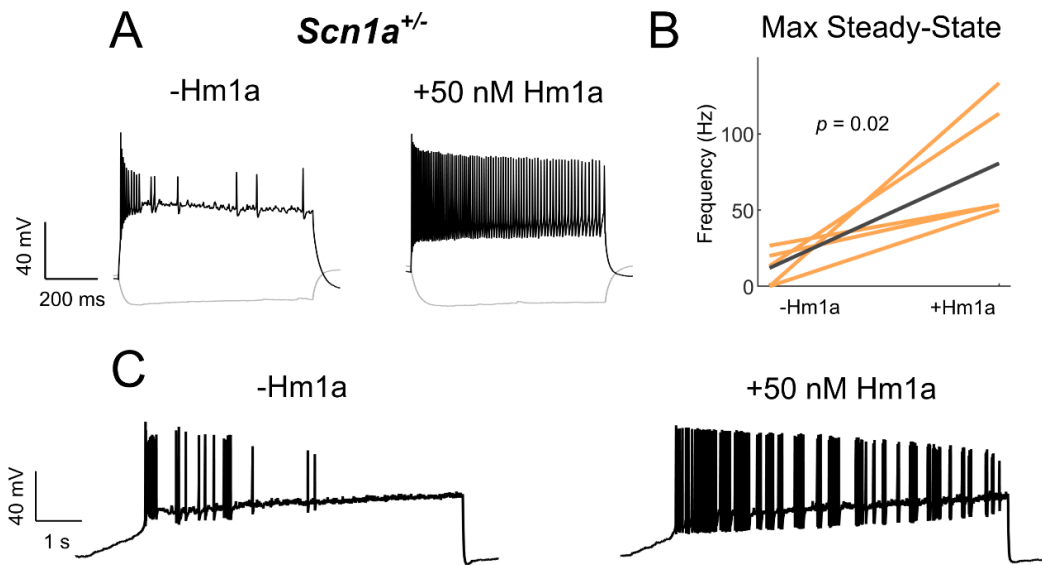


**Figure S8. Effects of low concentration Hm1a on IS VIP-IN firing**

- A) Example traces from recordings of a representative IS VIP-IN from an *Scn1a*.VIP-Cre.tdT mouse before and after bath application of 50 nM Hm1a at a 3X rheobase current injection.
- B) Summary data showing an increase in maximal steady-state firing frequency with application of 50 nM Hm1a.  $n = 5$  VIP-INS from three *Scn1a*.VIP-Cre.tdT mice;  $p$  values determined by a paired student's t-test.
- C) 8-second ramp depolarization with an amplitude of 200pA of the IS VIP-IN from panel A. While Hm1a greatly increases firing frequency, IS VIP-INS retain a distinct irregular spiking firing pattern.

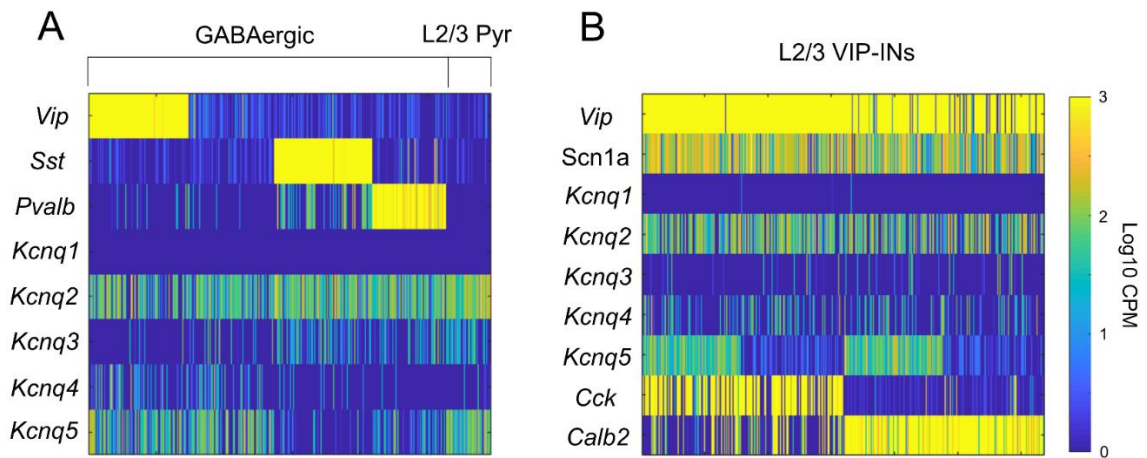


**Figure S9. *Kcnq5* is selectively expressed in a subset of VIP-INs**

A) Data from the Allen Cell Types Database, [celltypes.brain-map.org/rnaseq](http://celltypes.brain-map.org/rnaseq) (as in

Figure S1). Each bar represents RNA-Seq reads in counts per million (CPM)

from a single cell. *Kcnq2* is broadly expressed in most GABAergic INs, while

*Kcnq5* is generally restricted to VIP-INs, as well as other non-PV/SST INs and

layer 2/3 pyramidal cells. There is very limited expression of *Kcnq1,3, and 4* in

any of these populations.

B) As in A, focusing on expression in VIP-INs in layer 2/3 grouped based on

expression of *Cck* and *Calb2* (aka CR). *Scn1a* is expressed in most VIP-INs with

no preference for *Cck* or *Calb2* expressing VIP-INs. *Kcnq5* is also expressed

equally in both *Cck* and *Calb2* containing VIP-INs, although only approximately

50% of both populations express significant levels of *Kcnq5*. Cells were sorted by

*Kcnq5* expression to clearly show the relatively equal proportions of *Kcnq5*

expression in both *Cck* and *Calb2* populations.

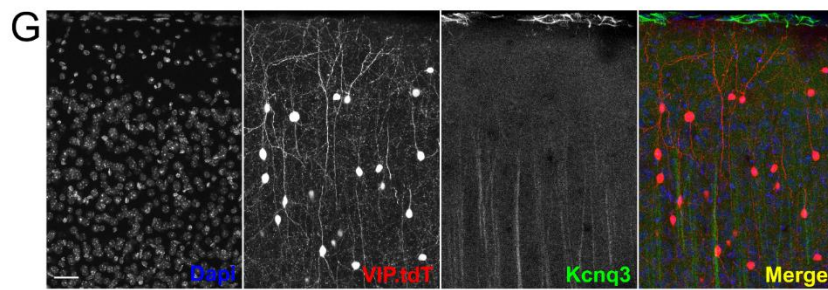
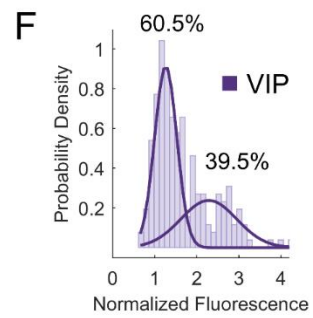
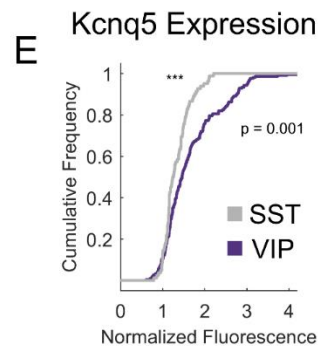
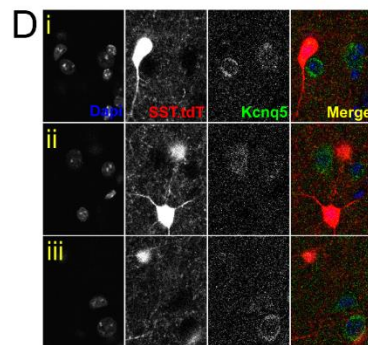
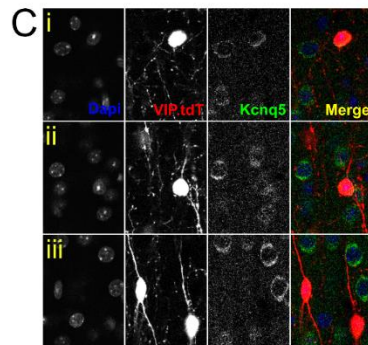
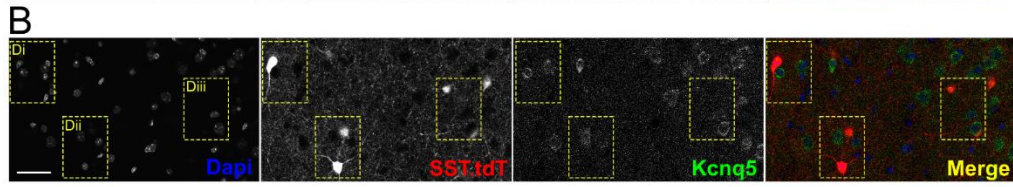
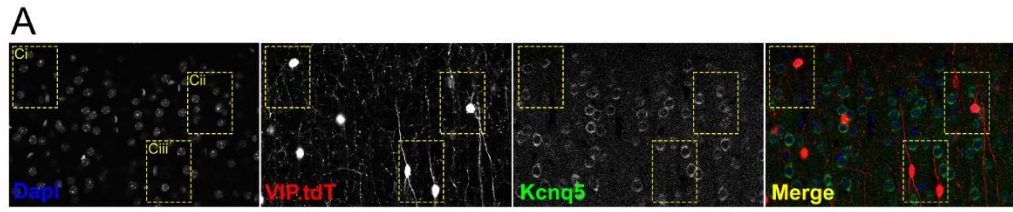


**Figure S10. Kcnq5 but not Kcnq3 is expressed in VIP-INs**

- A) Confocal micrographs of Kcnq5 staining in layer 2/3 of an adult WT.VIP-Cre.tdT mouse. Kcnq5 localizes to the soma of many pyramidal neurons as well as a population (Ci and Cii) of VIP-INs.
- B) Same as in A, but in layer 5 of an adult WT.SST-Cre.tdT mouse. Layer 5 pyramidal neurons, but not SST-INs, stain positive for Kcnq5. Scale = 50  $\mu$ M for A and B.
- C) Enlarged VIP-INs (*yellow boxes*) from A.
- D) Enlarged SST-INs (*yellow boxes*) from B.
- E) Quantification of Kcnq5 staining in VIP and SST-INs. The mean fluorescence of the Kcnq5 signal in each cell is normalized to the background fluorescence of neuropil. VIP-INs show a non-normal distribution ( $p = 1 \text{ E } -112$ , one sample KS test) and have a significantly different distribution than SST-INs ( $p$  value indicated, two sample KS test).  $n = 293$  VIP-INs from 3 WT.VIP-Cre.tdT mice, and  $n = 117$  SST-INs from one WT.SST-Cre.tdT mouse.
- F) Histogram of the distribution of VIP-IN Kcnq5 labelling. The probability density of the data was fit with a mixture of two normal distributions using maximum likelihood estimation yielding a mixing parameter of 0.605 with mean and standard deviations of  $1.2 \pm 0.2$  and  $2.3 \pm 0.6$  (corresponding to 60.5% “negative” and 39.5% “positive” VIP-INs).
- G) Confocal micrographs of Kcnq3 staining in layer 2/3 of an adult WT.VIP-Cre.tdT mouse. Kcnq3 shows very sparse labelling in cortex, mostly limited to presumptive ascending apical dendrites, and is not found on VIP-INs. Scale = 50  $\mu$ M. Images are representative of  $n = 3$  mice with two technical replicates each.

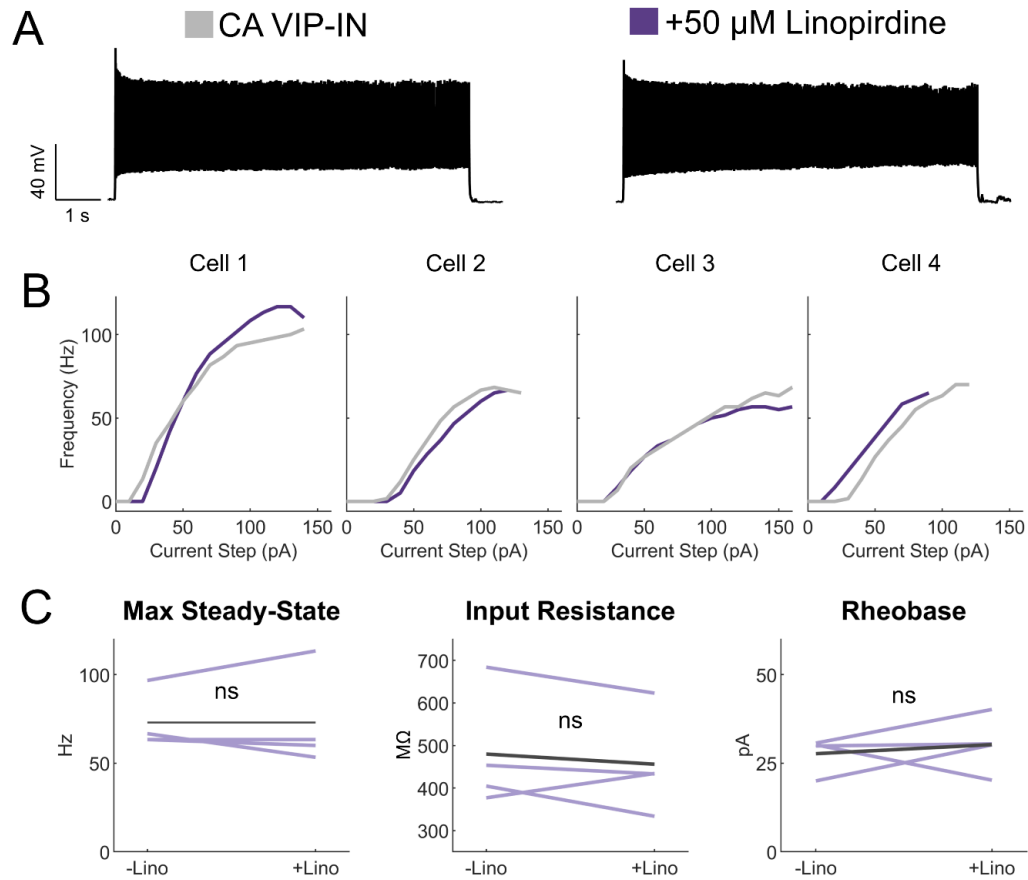


**Figure S11. Linopirdine has no effect on CA VIP-IN excitability**

- A) Representative 8-second square depolarization at 2X rheobase of a WT CA VIP-IN showing no change in firing pattern.
- B) Individual *I*-*f* curves for  $n = 4$  cells from 2 WT.VIP-Cre.tdT mice before (*gray*) and after (*purple*) addition of linopirdine.
- C) Summary of intrinsic and excitability parameters from the cells in B showing no change with the addition on linopirdine.

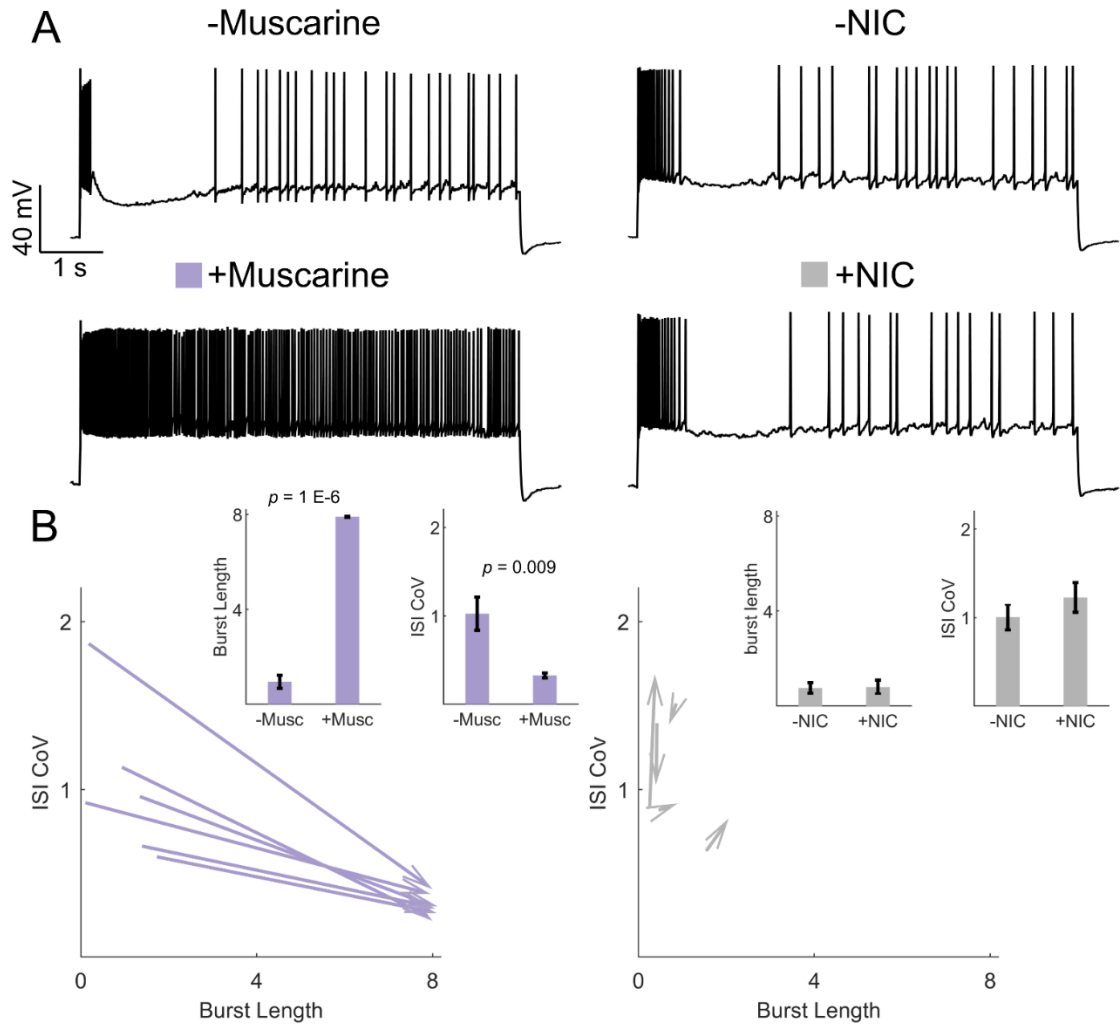


**Figure S12. Muscarinic but not nicotinic receptor activation is sufficient to induce irregular-tonic switching in IS VIP-INs**

- A) Example of the response to an 8-second square depolarization of two IS VIP-INs from adult WT.VIP-Cre.tdT mice before (*top*) and after (*bottom*) application of either 5  $\mu\text{M}$  muscarine or 1  $\mu\text{M}$  of the nicotinic agonist (NIC) 4-Acetyl-1,1-dimethylpiperazinium iodide. Scale is 40mV and 1 second.
- B) Quantification of changes in firing patterns of IS VIP-INs in response to muscarine ( $n = 6$  cells; 3 mice) or NIC ( $n = 5$  cells; 2 mice). Muscarine caused a switch to a continuous firing mode represented by increased burst length and decreased ISI

CoV (indicated by arrowheads as in Figure 6);  $p$ -values determined by paired students' t-test. There were no apparent changes in IS VIP-IN firing patterns with NIC application.

## REFERENCES

- Acsády, L., Kamondi, A., Sík, A., Freund, T., and Buzsáki, G. (1998). GABAergic cells are the major postsynaptic targets of mossy fibers in the rat hippocampus. *J. Neurosci.* *18*, 3386–3403.
- Alitto, H.J., and Dan, Y. (2013). Cell-type-specific modulation of neocortical activity by basal forebrain input. *Front. Syst. Neurosci.* *6*, 79.
- Alshammari, M.A., Alshammari, T.K., and Laezza, F. (2016). Improved methods for fluorescence microscopy detection of macromolecules at the axon initial segment. *Front. Cell. Neurosci.* *10*, 1–20.
- Askew, C.E., Lopez, A.J., Wood, M.A., and Metherate, R. (2019). Nicotine excites VIP interneurons to disinhibit pyramidal neurons in auditory cortex. *Synapse* *73*, 1–12.
- Batista-Brito, R., Vinck, M., Ferguson, K.A., Chang, J.T., Laubender, D., Lur, G., Mossner, J.M., Hernandez, V.G., Ramakrishnan, C., Deisseroth, K., et al. (2017). Developmental Dysfunction of VIP Interneurons Impairs Cortical Circuits. *Neuron* *95*, 884-895.e9.
- Berkvens, J.J.L., Veugen, I., Veendrick-Meekes, M.J.B.M., Snoeijen-Schouwenaars, F.M., Schelhaas, H.J., Willemsen, M.H., Tan, I.Y., and Aldenkamp, A.P. (2015). Autism and behavior in adult patients with Dravet syndrome (DS). *Epilepsy Behav.* *47*, 11–16.
- Brown, D.A., and Passmore, G.M. (2009). Neural KCNQ (Kv7) channels. *Br. J. Pharmacol.* *156*, 1185–1195.



Catterall, W.A. (2018). Dravet syndrome: a sodium channel interneuronopathy. *Curr. Opin. Physiol.* 2, 42–50.

Catterall, W.A., Kalume, F., and Oakley, J.C. (2010). Na<sub>v</sub> 1.1 channels and epilepsy. *J. Physiol.* 588, 1849–1859.

Claes, L., Del-Favero, J., Ceulemans, B., Lagae, L., Van Broeckhoven, C., and De Jonghe, P. (2001). De novo mutations in the sodium-channel gene *SCN1A* cause severe myoclonic epilepsy of infancy. *Am. J. Hum. Genet.* 68, 1327–1332.

Defelipe, J., López-Cruz, P.L., Benavides-Piccione, R., Bielza, C., Larrañaga, P., Anderson, S., Burkhalter, A., Cauli, B., Fairén, A., Feldmeyer, D., et al. (2013). New insights into the classification and nomenclature of cortical GABAergic interneurons. *Nat. Rev. Neurosci.*

Dravet, C., and Oguni, H. (2013). Dravet syndrome (severe myoclonic epilepsy in infancy) (Elsevier B.V.).

Drion, G., Bonjean, M., Waroux, O., Scuvée-Moreau, J., Liégeois, J.-F., Sejnowski, T.J., Sepulchre, R., and Seutin, V. (2010). M-type channels selectively control bursting in rat dopaminergic neurons. *Eur. J. Neurosci.* 31, 827–835.

von Engelhardt, J., Eliava, M., Meyer, A.H., Rozov, A., and Monyer, H. (2007). Functional Characterization of Intrinsic Cholinergic Interneurons in the Cortex. *J. Neurosci.* 27, 5633–5642.

Favero, M., Sotuyo, N.P., Lopez, E., Kearney, J.A., and Goldberg, E.M. (2018). A Transient Developmental Window of Fast-Spiking Interneuron Dysfunction in a Mouse Model of Dravet Syndrome. *J. Neurosci.* 38, 7912–7927.

Fu, Y., Tucciarone, J.M., Espinosa, J.S., Sheng, N., Darcy, D.P., Nicoll, R.A., Huang, Z.J., and Stryker, M.P. (2014). A Cortical Circuit for Gain Control by Behavioral State. *Cell* 156, 1139–1152.

Fu, Y., Kaneko, M., Tang, Y., Alvarez-Buylla, A., and Stryker, M.P. (2015). A cortical disinhibitory circuit for enhancing adult plasticity. *Elife* 2015, 1–12.

Genton, P., Velizarova, R., and Dravet, C. (2011). Dravet syndrome: The long-term outcome. *Epilepsia* 52, 44–49.

Gouwens, N.W., Sorensen, S.A., Berg, J., Lee, C., Jarsky, T., Ting, J., Sunkin, S.M., Feng, D., Anastassiou, C., Barkan, E., et al. (2018). Classification of electrophysiological and morphological types in mouse visual cortex. *BioRxiv*.

Han, S., Tai, C., Westenbroek, R.E., Yu, F.H., Cheah, C.S., Potter, G.B., Rubenstein, J.L., Scheuer, T., de la Iglesia, H.O., and Catterall, W.A. (2012). Autistic-like behaviour in *Scn1a* +/- mice and rescue by enhanced GABA-mediated neurotransmission. *Nature* 489, 385–390.

He, M., Tucciarone, J., Lee, S., Nigro, M.J., Kim, Y., Levine, J.M., Kelly, S.M., Krugikov, I., Wu, P., Chen, Y., et al. (2016). Strategies and Tools for Combinatorial Targeting of GABAergic Neurons in Mouse Cerebral Cortex. *Neuron* 92, 555.

Kalume, F., Westenbroek, R.E., Cheah, C.S., Yu, F.H., Oakley, J.C., Scheuer, T., and Catterall, W.A. (2013). Sudden unexpected death in a mouse model of Dravet syndrome. *J. Clin. Invest.* 123, 1798–1808.

Kawaguchi, Y. (1997). Selective cholinergic modulation of cortical GABAergic cell subtypes. *J. Neurophysiol.* 78, 1743–1747.

Kawaguchi, Y., and Kubota, Y. (1997). GABAergic cell subtypes and their synaptic connections in rat frontal cortex. *Cereb. Cortex* 7, 476–486.

Krabbe, S., Paradiso, E., d'Aquin, S., Bitterman, Y., Xu, C., Yonehara, K., Markovic, M., Gruendemann, J., Ferraguti, F., and Luthi, A. (2018). Adaptive disinhibitory gating by VIP interneurons permits associative learning. *BioRxiv* 443614.

Lee, S., Hjerling-leffler, J., Zaghera, E., and Fishell, G. (2010). The largest group of superficial neocortical GABAergic interneurons expresses ionotropic serotonin receptors. *J. Neurosci.* 30, 16796–16808.

Lee, S., Kruglikov, I., Huang, Z.J., Fishell, G., and Rudy, B. (2013). A disinhibitory circuit mediates motor integration in the somatosensory cortex. *Nat. Neurosci.* 16, 1662–1670.

Li, B.-M., Liu, X.-R., Yi, Y.-H., Deng, Y.-H., Su, T., Zou, X., and Liao, W.-P. (2011). Autism in Dravet syndrome: Prevalence, features, and relationship to the clinical characteristics of epilepsy and mental retardation. *Epilepsy Behav.* 21, 291–295.

Li, T., Tian, C., Scalmani, P., Frassoni, C., Mantegazza, M., Wang, Y., Yang, M., Wu, S., and Shu, Y. (2014). Action Potential Initiation in Neocortical Inhibitory Interneurons. *PLoS Biol.* 12.

Liu, Y., Lopez-Santiago, L.F., Yuan, Y., Jones, J.M., Zhang, H., O'Malley, H.A., Patino, G.A., O'Brien, J.E., Rusconi, R., Gupta, A., et al. (2013). Dravet syndrome patient-derived neurons suggest a novel epilepsy mechanism. *Ann. Neurol.* 74, 128–139.

Miller, A.R., Hawkins, N.A., McCollom, C.E., and Kearney, J.A. (2014). Mapping genetic modifiers of survival in a mouse model of Dravet syndrome. *Genes, Brain Behav.* 13, 163–172.

- Mistry, A.M., Thompson, C.H., Miller, A.R., Vanoye, C.G., George, A.L., and Kearney, J.A. (2014). Strain- and age-dependent hippocampal neuron sodium currents correlate with epilepsy severity in Dravet syndrome mice. *Neurobiol. Dis.* 65, 1–11.
- Morel, P. (2018). Gramm: grammar of graphics plotting in Matlab. *J. Open Source Softw.* 3, 568.
- Munoz, W., Tremblay, R., Levenstein, D., and Rudy, B. (2017). Layer-specific modulation of neocortical dendritic inhibition during active wakefulness. *Science* (80-. ). 355, 954–959.
- Oakley, J.C., Kalume, F., Yu, F.H., Scheuer, T., and Catterall, W.A. (2009). Temperature- and age-dependent seizures in a mouse model of severe myoclonic epilepsy in infancy. *Proc. Natl. Acad. Sci. U. S. A.* 106, 3994–3999.
- Ogiwara, I., Miyamoto, H., Morita, N., Atapour, N., Mazaki, E., Inoue, I., Takeuchi, T., Itohara, S., Yanagawa, Y., Obata, K., et al. (2007). Nav1.1 localizes to axons of parvalbumin-positive inhibitory interneurons: A circuit basis for epileptic seizures in mice carrying an *Scn1a* gene mutation. *J. Neurosci.* 27, 5903–5914.
- Osteen, J.D., Herzig, V., Gilchrist, J., Emrick, J.J., Zhang, C., Wang, X., Castro, J., Garcia-Caraballo, S., Grundy, L., Rychkov, G.Y., et al. (2016). Selective spider toxins reveal a role for the Nav1.1 channel in mechanical pain. *Nature* 534, 494–499.
- Osteen, J.D., Sampson, K., Iyer, V., Julius, D., and Bosmans, F. (2017). Pharmacology of the Nav1.1 domain IV voltage sensor reveals coupling between inactivation gating processes. *Proc. Natl. Acad. Sci. U. S. A.* 114, 6836–6841.
- Paul, A., Crow, M., Raudales, R., He, M., Gillis, J., and Huang, Z.J. (2017).

Transcriptional Architecture of Synaptic Communication Delineates GABAergic Neuron Identity. *Cell* 171, 522-539.e20.

Pi, H.J., Hangya, B., Kvitsiani, D., Sanders, J.I., Huang, Z.J., and Kepecs, A. (2013). Cortical interneurons that specialize in disinhibitory control. *Nature* 503, 521–524.

Porter, J.T., Cauli, B., Staiger, J.F., Lambolez, B., Rossier, J., and Audinat, E. (1998). Properties of bipolar VIPergic interneurons and their excitation by pyramidal neurons in the rat neocortex. *Eur. J. Neurosci.* 10, 3617–3628.

Porter, J.T., Cauli, B., Tsuzuki, K., Lambolez, B., Rossier, J., and Audinat, E. (1999). Selective excitation of subtypes of neocortical interneurons by nicotinic receptors. *J. Neurosci.* 19, 5228–5235.

Prönneke, A., Scheuer, B., Wagener, R.J., Möck, M., Witte, M., and Staiger, J.F. (2015). Characterizing VIP neurons in the barrel cortex of VIPcre/tdTomato mice reveals layer-specific differences. *Cereb. Cortex* 25, 4854–4868.

Prönneke, A., Witte, M., Möck, M., and Staiger, J.F. (2020). Neuromodulation leads to a burst-tonic switch in a subset of VIP neurons in mouse primary somatosensory (Barrel) cortex. *Cereb. Cortex* 30, 488–504.

Reimer, J., Froudarakis, E., Cadwell, C.R., Yatsenko, D., Denfield, G.H., and Tolias, A.S. (2014). Pupil Fluctuations Track Fast Switching of Cortical States during Quiet Wakefulness. *Neuron* 84, 355–362.

Rubinstein, M., Han, S., Tai, C., Westenbroek, R.E., Hunker, A., Scheuer, T., and Catterall, W.A. (2015). Dissecting the phenotypes of Dravet syndrome by gene deletion. *Brain* 138, 2219–2233.

Scheffer, I.E. (2012). Diagnosis and long-term course of Dravet syndrome. *Eur. J. Paediatr. Neurol.* 16, S5--S8.

De Stasi, A.M., Farisello, P., Marcon, I., Cavallari, S., Forli, A., Vecchia, D., Losi, G., Mantegazza, M., Panzeri, S., Carmignoto, G., et al. (2016). Unaltered Network Activity and Interneuronal Firing during Spontaneous Cortical Dynamics *in vivo* in a Mouse Model of Severe Myoclonic Epilepsy of Infancy. *Cereb. Cortex* 26, 1778–1794.

Stiefel, K.M., Englitz, B., and Sejnowski, T.J. (2013). Origin of intrinsic irregular firing in cortical interneurons. *Proc. Natl. Acad. Sci. U. S. A.* 110, 7886–7891.

Sun, Y., Paşca, S.P., Portmann, T., Goold, C., Worringer, K.A., Guan, W., Chan, K.C., Gai, H., Vogt, D., Chen, Y.J.J., et al. (2016). A deleterious Nav1.1 mutation selectively impairs telencephalic inhibitory neurons derived from Dravet Syndrome patients. *Elife* 5, 1–26.

Tai, C., Abe, Y., Westenbroek, R.E., Scheuer, T., and Catterall, W.A. (2014). Impaired excitability of somatostatin- and parvalbumin-expressing cortical interneurons in a mouse model of Dravet syndrome. *Proc. Natl. Acad. Sci. U. S. A.* 111, 3139–3148.

Taniguchi, H., He, M., Wu, P., Kim, S., Paik, R., Sugino, K., Kvitsiani, D., Fu, Y., Lu, J., Lin, Y., et al. (2011). A resource of cre driver lines for genetic targeting of GABAergic neurons in cerebral cortex. *Neuron* 72, 1091.

Tasic, B., Menon, V., Nguyen, T.N., Kim, T.K., Jarsky, T., Yao, Z., Levi, B., Gray, L.T., Sorensen, S.A., Dolbeare, T., et al. (2016). Adult mouse cortical cell taxonomy revealed by single cell transcriptomics. *Nat. Neurosci.* 19, 335–346.

Tremblay, R., Lee, S., and Rudy, B. (2016). GABAergic Interneurons in the Neocortex:

From Cellular Properties to Circuits. *Neuron* 91, 260–292.

Turi, G.F., Li, W.K., Chavlis, S., Pandi, I., O'Hare, J., Priestley, J.B., Grosmark, A.D., Liao, Z., Ladow, M., Zhang, J.F., et al. (2019). Vasoactive Intestinal Polypeptide-Expressing Interneurons in the Hippocampus Support Goal-Oriented Spatial Learning. *Neuron* 101, 1150-1165.e8.

Villas, N., Meskis, M.A., and Goodliffe, S. (2017). Dravet syndrome: Characteristics, comorbidities, and caregiver concerns. *Epilepsy Behav.* 74, 81–86.

Walker, F., Möck, M., Feyerabend, M., Guy, J., Wagener, R.J., Schubert, D., Staiger, J.F., and Witte, M. (2016). Parvalbumin-and vasoactive intestinal polypeptide-expressing neocortical interneurons impose differential inhibition on Martinotti cells. *Nat. Commun.* 7.

Yamagata, T., Ogiwara, I., Mazaki, E., Yanagawa, Y., and Yamakawa, K. (2017). Nav1.2 is expressed in caudal ganglionic eminence-derived disinhibitory interneurons: Mutually exclusive distributions of Nav1.1 and Nav1.2. *Biochem. Biophys. Res. Commun.* 491, 1070–1076.

Yu, F.H., Mantegazza, M., Westenbroek, R.E., Robbins, C.A., Kalume, F., Burton, K.A., Spain, W.J., McKnight, G.S., Scheuer, T., and Catterall, W.A. (2006). Reduced sodium current in GABAergic interneurons in a mouse model of severe myoclonic epilepsy in infancy. *Nat. Neurosci.* 9, 1142–1149.

Zhang, S., Xu, M., Kamigaki, T., Do, J.P.H., Chang, W.-C., Jenvay, S., Miyamichi, K., Luo, L., and Dan, Y. (2014). Long-Range and Local Circuits for Top-Down Modulation of Visual Cortical Processing. *Science* (80-. ). 345, 660–665.

# Chapter 3: VIP interneuron dysfunction underlies abnormal neocortical state transitions and behavior in a severe neurodevelopmental disorder

## ABSTRACT

Dravet Syndrome (DS) is a severe neurodevelopmental disorder caused by loss of function variants in the gene *SCN1A* which encodes the voltage-gated sodium ( $\text{Na}^+$ ) channel subunit Nav1.1. Nav1.1-containing  $\text{Na}^+$  channels support action potential generation and propagation in GABAergic interneurons (INs), with loss of Nav1.1 leading to impaired interneuron IN excitability. We recently showed that Vasoactive Intestinal Peptide interneurons (VIP-INs) express Nav1.1 and are impaired in *Scn1a*<sup>+/-</sup> mice. We hypothesize that VIP-IN mediated disinhibitory circuits are also impaired in *Scn1a*<sup>+/-</sup> mice *in vivo*, potentially underlying the non-epilepsy features of autism spectrum disorder (ASD) and intellectual disability (ID) characteristic of DS. To test this, we performed 2-photon calcium imaging of genetically identified VIP-INs and excitatory pyramidal neurons in neocortex in freely behaving *Scn1a*<sup>+/-</sup> and WT mice along with pupil diameter and locomotion speed. We found that VIP-IN mediated cortical state transitions that accompany behavioral transitions from quiet wakefulness to active running are suppressed in *Scn1a*<sup>+/-</sup> mice. Carbachol exacerbated VIP-IN dysfunction in acute brain slice from *Scn1a*<sup>+/-</sup> mice via downregulation of  $\text{Na}^+$  current, while optogenetic activation of VIP-INs during locomotion bouts rescued cortical state transitions in *Scn1a*<sup>+/-</sup> mice. We observed similar cortical dysfunction with VIP-IN selective *Scn1a* deletion (VIP-Cre.*Scn1a*<sup>+fl</sup>). VIP-Cre.*Scn1a*<sup>+fl</sup> also recapitulated core behavioral features of the global DS model, but without seizures or sudden death (SUDEP). Our data indicate that VIP-IN



mediated circuits are impaired in DS and selectively contribute to the severe ASD and ID features of DS.

## INTRODUCTION

Interneurons (INs) form a diverse array of microcircuits in the neocortex, embedded across brain regions based on defined cell types and patterns of connectivity (Guet-McCreight et al., 2020; Jiang et al., 2015; Kepecs & Fishell, 2014; Pfeffer, 2013; Yao et al., 2021). These circuits endow the cortex with flexible computational power, yet also create a vulnerability to neurological disorders caused by disrupted IN function. Epilepsy and autism spectrum disorder (ASD) are both associated with impaired IN function (Goff & Goldberg, 2021; Goldberg & Coulter, 2013; Jacob, 2016; Lunden et al., 2019). However, it is unclear how impairment of specific IN types can lead to both disorders defined by either state dependent paroxysmal events such as seizures, or as durable impairments in cognitive function such as ASD and intellectual disability (ID). Dravet Syndrome (DS) is a severe neurodevelopmental disorder defined by treatment-resistant epilepsy, prominent features of ASD, developmental delay, ID, and sudden unexplained death (SUDEP). (Dravet, 2011; Dravet & Oguni, 2013). Nearly all cases are caused by heterozygous loss of function variants in *SCN1A* encoding the sodium ( $\text{Na}^+$ ) channel  $\alpha$  subunit Nav1.1 (Catterall, 2017; Claes et al., 2001; Meisler et al., 2021). Despite this clearly defined genetic etiology, there are currently no disease modifying therapies for the associated non-epilepsy comorbidities of ASD and ID (Genton et al., 2011; Takayama et al., 2014).

At the cellular and circuit level, data from *Scn1a*<sup>+/-</sup> mice and neurons generated from patient derived stem cells demonstrates that Nav1.1 is preferentially expressed in INs. The three largest classes of cerebral cortical INs, those expressing parvalbumin (PV), somatostatin (SST), and vasoactive intestinal peptide (VIP-INs) (Rudy et al., 2011), are hypoexcitable in acute slice preparations from young/developing *Scn1a*<sup>+/-</sup>

mice (De Stasi et al., 2016; Favero et al., 2018; Goff & Goldberg, 2019; Tai et al., 2014). Likewise, knocking out *Scn1a* in INs but not glutamatergic neurons recapitulates the global phenotype of seizures and behavioral abnormalities (Oakley et al., 2009; Ogiwara et al., 2013; Rubinstein et al., 2015; Tatsukawa et al., 2018). Nevertheless, the hypothesized IN dysfunction is not clearly reflected *in vivo* in the *Scn1a*<sup>+/-</sup> model. PV and SST-INs fire at similar frequencies in *Scn1a*<sup>+/-</sup> mice compared to WT *in vivo*, and there are only relatively mild changes in global electrophysiological measures such as EEG that is not consistent with underlying impairments of IN function. (De Stasi et al., 2016; Jansen et al., 2021; Tran et al., 2020). Identifying the circuit impact of subtype-specific interneuronopathies remains elusive.

There are two contributing factors which may have obscured *in vivo* studies of INs in *Scn1a*<sup>+/-</sup> mice. The first is that loss of Nav1.1 in PV, SST, and VIP-INs causes distinct developmental patterns of dysfunction. Specifically, PV-INs show the greatest impairment near the developmental onset of seizures but regain essentially normal excitability as *Scn1a*<sup>+/-</sup> mice age (Favero et al., 2018; Kaneko et al., 2021). In the hippocampus, SST-INs show a similar pattern of impairment with the most severe deficit found around the onset of seizures (~P20) followed by partial stabilization at later time points (Almog et al., 2021). The second contributing factor is that cellular dysfunction may be state dependent, which is not well modeled in acute brain slices. For instance, many ionic conductances including Na<sup>+</sup> current respond to changes in neuromodulatory state producing different firing modes in INs (Cantrell et al., 1996; Cantrell & Catterall, 2001; Goff & Goldberg, 2019; Prönneke et al., 2020). Hence, loss of Nav1.1 may cause state-dependent IN dysfunction. For instance, *Scn1a*<sup>+/-</sup> mice appear to have EEG abnormalities that depend on their sleep and arousal states (Jansen et al., 2021).

Recording spontaneous IN activity in anesthetized mice, or even in awake mice without monitoring activity across changes in cortical states may conceal the impact of IN dysfunction in *Scn1a*<sup>+/-</sup> mice.

VIP-INs are also hypoexcitable in acute brain slices from *Scn1a*<sup>+/-</sup> mice, but, unlike PV-INs, this dysfunction persists through development (Goff & Goldberg, 2019). VIP-INs selectively target other INs, particularly SST-INs, exerting a primarily disinhibitory effect on local circuits (Acsády et al., 1996; Fu et al., 2014; A. T. Lee et al., 2019; S. Lee et al., 2013; Munoz et al., 2017; Pi et al., 2013; Turi et al., 2019). Depending on the cortical area, VIP-IN disinhibitory microcircuits shape sensory processing, cortical plasticity, and development, influencing behaviors ranging from simple stimulus detection to more complex cognitive operations such as memory tasks and social interaction (Mossner et al., 2020; Newmyer et al., 2019). Therefore, VIP-INs may be particularly important for the persistent ASD and ID phenotypes of DS. The disinhibitory role of VIP-INs is reliably linked to cortical state transitions (CSTs) in sensory and associative cortices which may be critical for stimulus gain control, learning, and hippocampal and neo-cortical plasticity (Fu et al., 2015; Garcia-Junco-Clemente et al., 2017; Garrett et al., 2020; Harris & Thiele, 2011; Reimer et al., 2014; Turi et al., 2019). Such transitions are driven largely by ascending cholinergic neuromodulation, activating VIP-INs and driving a broad increase in layer 2/3 pyramidal neuron activity during active behavioral states (McGinley et al., 2015; Reimer et al., 2014). We hypothesize that the circuit functions of VIP-INs are disrupted in *Scn1a*<sup>+/-</sup> mice and may underlie features of ASD in this model and in human patients.

Using 2-photon (2P) calcium imaging, we found that VIP-INs were dysfunctional, and CSTs were impaired *in vivo* in young adult *Scn1a<sup>+/-</sup>* mice. VIP-INs were unresponsive to cholinergic neuromodulation *in vitro* as stimulating VIP-INs with carbachol led to Na<sup>+</sup> current down regulation that compounded existing VIP-IN dysfunction in *Scn1a<sup>+/-</sup>* mice. Conversely, boosting VIP-IN function in *Scn1a<sup>+/-</sup>* mice using closed-loop optogenetics rescued network activity during CSTs *in vivo*. Similar results were obtained in mice with VIP-IN specific *Scn1a* deletion (VIP-Cre.*Scn1a<sup>fl/+</sup>*). Furthermore, VIP-Cre.*Scn1a<sup>fl/+</sup>* mice recapitulated core ASD endophenotypes of the DS model, yet without epilepsy or SUDEP. Together, these data indicate that loss of *Scn1a* in VIP-INs disrupts cortical state dynamics and causes behavioral abnormalities linked to ASD and ID in DS.

## RESULTS

### Abnormal Cortical State Transitions in *Scn1a*<sup>+/-</sup> mice

Our previous work demonstrated that VIP-INs are dysfunctional in *Scn1a*<sup>+/-</sup> mice *in vitro* (Goff & Goldberg, 2019). Importantly, this dysfunction was nearly identical when recording from either pre-weanling or young adult mice. Based on these results, we hypothesized that *in vivo* circuits relying on recruitment of VIP-INs might be impaired in *Scn1a*<sup>+/-</sup> mice. VIP-INs are critical for increased cortical activity in primary sensory areas during active or aroused behavioral states. These CSTs are largely driven by ascending cholinergic and noradrenergic inputs, which drive the activity of VIP-INs and promote disinhibition of superficial cortical layers. Using 2P calcium imaging of GCaMP7s expressed in VIP-INs and non-VIP cells in primary visual cortex (V1), we recorded network activity in head-fixed WT and *Scn1a*<sup>+/-</sup> mice and compared activity across behavioral states with simultaneous pupillometry and locomotion tracking (Figure 1A).

VIP-IN activity as well as local network activity was reduced during locomotion bouts in *Scn1a*<sup>+/-</sup> mice compared to age-matched WT littermates (Figure 2 C-E, VIP-INs: modulation index, MI effect size,  $-0.11 \pm 0.04$ ;  $p = 0.01$ . non-VIP neurons:  $-0.16 \pm 0.05$ ;  $p = 0.005$ ). Fewer VIP-INs were positively correlated with pupil diameter (effect size,  $-0.15$ ; error,  $0.07$ ;  $p = 0.037$ ), and overall network activity was shifted with increased anticorrelation ( $+0.16 \pm 0.06$ ;  $p = 0.008$ ) and decreased correlation ( $-0.19 \pm 0.07$ ;  $p = 0.01$ ) with pupil diameter in *Scn1a*<sup>+/-</sup> mice (Figure 2 F). We found that under these conditions WT and *Scn1a*<sup>+/-</sup> mice had a similar number of running bouts, ran at similar speeds, and had identical degrees of pupil dilation associated with locomotion (Figure S1). Therefore, blunted CSTs in *Scn1a*<sup>+/-</sup> mice are likely independent of differences in

arousal or behavioral states between genotypes. As an independent readout of network activity, we examined the background neuropil signal and found a reduced locomotion MI and reduced correlation with pupil diameter in *Scn1a*<sup>+/-</sup> mice (Figure S2).

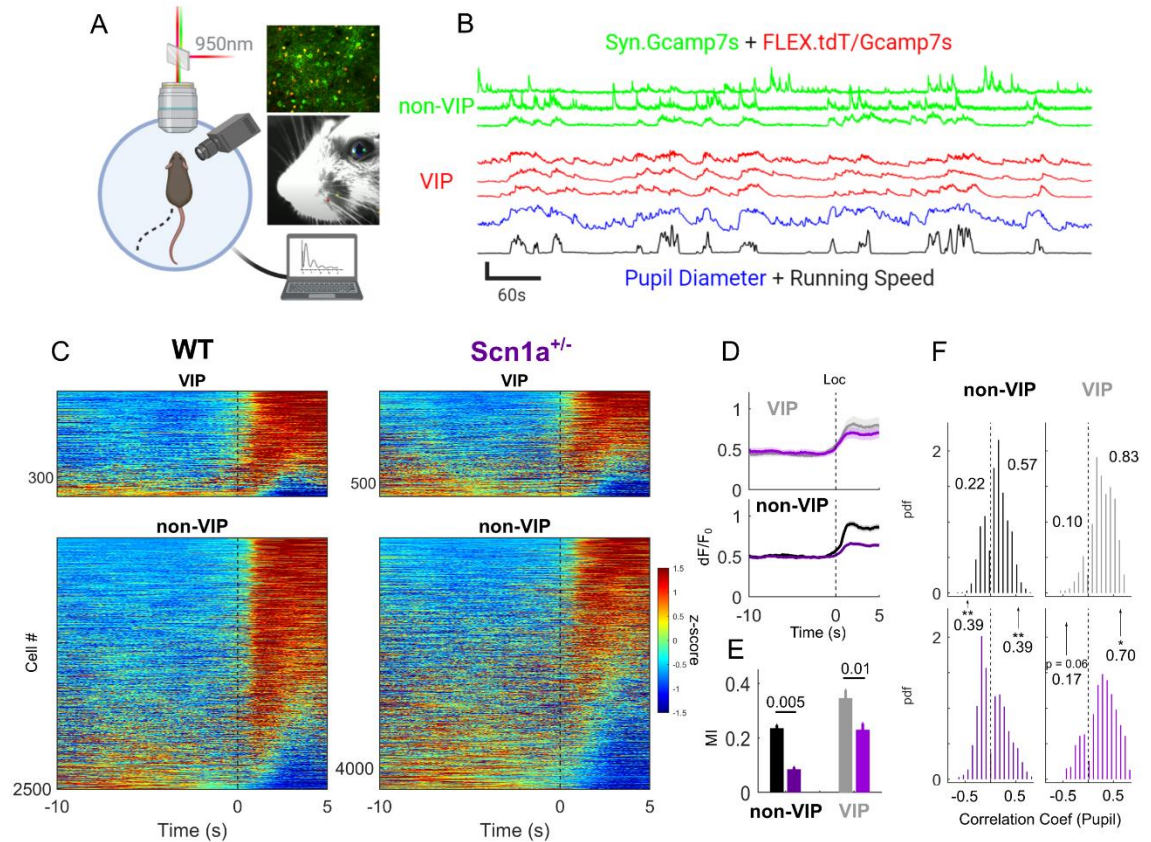


**Figure 1. Altered *in vivo* VIP-IN activity and CSTs in *Scn1a*<sup>+/-</sup> mice.** A) Schematic of experimental design. Adult WT and *Scn1a*<sup>+/-</sup> mice implanted with cranial windows over V1 were head-fixed and allowed to run freely on a floating disk. 2P imaging was synchronized to locomotion speed and a video feed of the mouse's pupil and whisker. Pupil diameter was extracted post-hoc using deeplabcut (DLC). B) 950nm light was used for simultaneous GCaMP7s imaging and tracking of VIP-IN identity with the red indicator tdT. Calcium transients, calculated as dF/F<sub>0</sub>, of non-VIP neurons (tdT<sup>-</sup>) and VIP-INs (tdT<sup>+</sup>) were extracted from each field of view and aligned to behavioral data. Traces of 3 individual non-VIP cells and VIP-INs are shown, along with pupil diameter and running speed. All traces are z-scored for visual clarity (vertical scale = 4, z-score). C) Heat map showing calcium transient activity for each cell at the onset of >5s locomotion bouts, averaged from multiple running bouts and z-scored within each cell. D) Average dF/F<sub>0</sub> at

the onset of locomotion across all VIP-INs and non-VIP neurons (mean and 95% CI). Black dotted line in C-D represents the onset of locomotion. E) Modulation of  $dF/F_0$  during periods of locomotion measured as an index value. F) Histograms of the time-zero correlation coefficient between individual cells' activity and pupil diameter normalized as a probability density where the area of each bar represents the proportion of cells that have a value in that bin. Only cells with significant positive or negative correlation are shown, and the percentages of each are indicated above each histogram. The percent of positive and negative correlated VIP and non-VIP neurons were compared across genotype and significant differences are indicated. \*,  $p < 0.05$ ; \*\*,  $p < 0.01$  (see Materials and Methods for information on statistical testing).  $n = 2511$  tdT- and 368 VIP-INs from  $N = 5$  WT mice,  $n = 4378$  tdT- and 577 VIP-INs from  $N = 6$  *Scn1a*<sup>+/-</sup> mice.

---

Our method of labelling VIP-INs with tdT is powerful because it allows the simultaneous imaging of VIP-INs and many hundreds of cells in the local network, but it does not explicitly distinguish between pyramidal neurons and other non-VIP-INs (both of which express GCaMP7s but are tdT negative). When we limited our analysis to cells with very high skew calcium traces, representing almost exclusively pyramidal neurons (Dipoppa et al., 2018), we found nearly identical results (Figure S3). In fact, an even larger percentage of *Scn1a*<sup>+/-</sup> pyramidal neurons were found to be anticorrelated with pupil diameter, and on average were negatively modulated by locomotion in *Scn1a*<sup>+/-</sup> mice. Finally, we measured the correlation between VIP-IN activity and non-VIP INs and found that during stationary periods, there was decreased correlation between the activity of VIP-INs and the local network in *Scn1a*<sup>+/-</sup> mice (Figure S4). This is despite the fact that baseline activity levels during stationary behaviors was similar between genotype based on analysis of the deconvolved event trains of VIP-INs and non-VIP neurons (Figure S5).

### **Cholinergic Modulation Exacerbates VIP-IN dysfunction in *Scn1a*<sup>+/-</sup> mice**

VIP-IN activity is largely driven by ascending cholinergic and noradrenergic neuromodulation during locomotion and pupil dilation. In addition to direct nicotinic



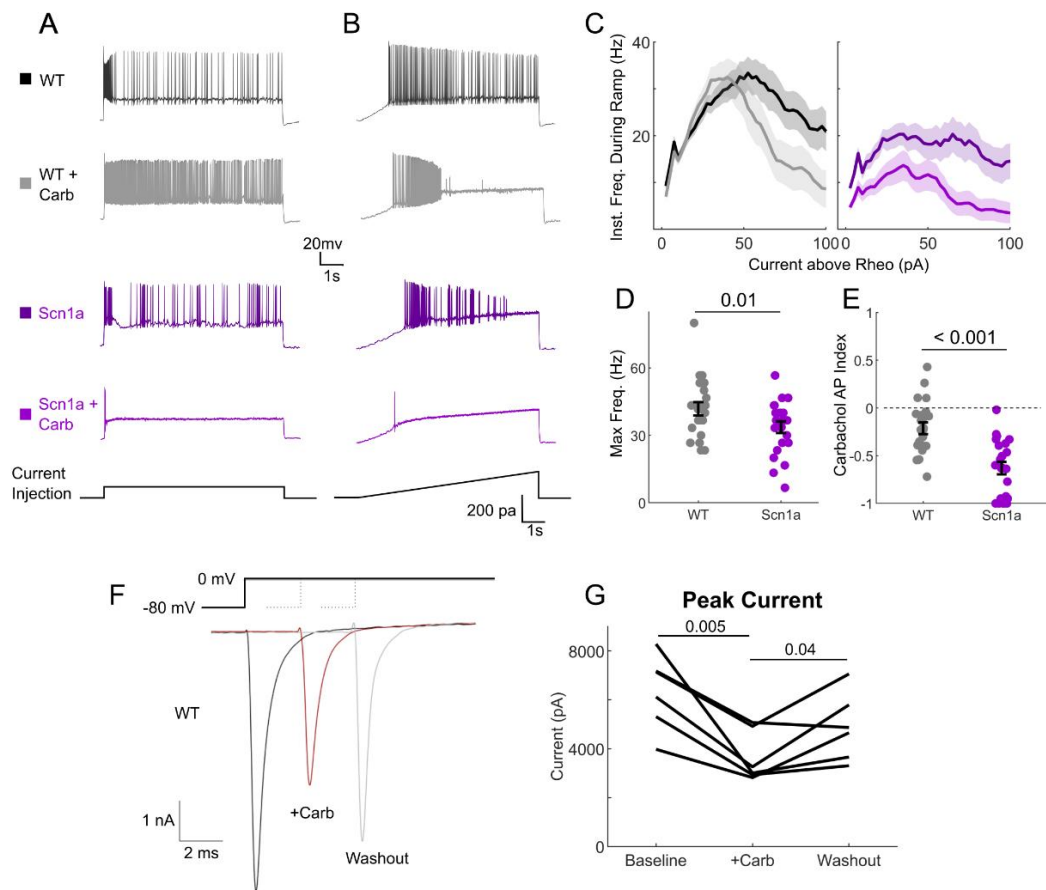


**Figure 2. Effect of cholinergic modulation on VIP-IN cellular excitability and  $\text{Na}^+$  current.** A-B) Examples of voltage responses of VIP-INs in acute slices of either WT or *Scn1a*<sup>+/-</sup> mice. Cells were stimulated with either A) a square 8s long pulse at 2X rheobase current or B) a slow 8s ramping current with a max of 200pA. The same cells are then recorded again after bath application of 5 $\mu$ M Carbachol. C) Current-frequency relationships for WT and *Scn1a*<sup>+/-</sup> VIP-INs elicited from 8s ramping depolarizations. Data was aligned to the Rheobase current for each cell, and instantaneous firing frequency was calculated using a 300ms sliding window. Solid lines and shaded areas represent mean  $\pm$  SEM. D) The maximum firing frequency for each WT and *Scn1a*<sup>+/-</sup> VIP-IN during the 8s ramp at baseline and the E) effect of carbachol on the total number of spikes generated during an 8s ramp depolarization calculated as an index value. F) Inward  $\text{Na}^+$  currents recorded in voltage clamp from WT VIP-INs in acute slices from a single depolarizing step from -80 to 0 mV. Individual sweeps are shown for each condition. Peak current was measured, repeated during bath application of 5 $\mu$ M carbachol, and a full or partial washout was observed in the majority of cells. G) Summary of data from the experiment in F, where connected lines show individual cells (n = 6 VIP-INs from 5 WT mice). Comparisons and p-values were calculated using a

paired student's t-test. There was no difference between Baseline and Washout conditions. P-values in D-E were determined by the Whitney Mann-U test. Dots represent individual data points (WT, n = 22 cells; *Scn1a*<sup>+/-</sup>, n = 22 cells).

---

depolarization, we recently showed that carbachol, a stable pan-cholinergic agonist, and muscarine both enhance WT VIP-IN excitability by modulating firing patterns via downregulating M-type potassium current. Interestingly, cholinergic second messenger signaling can also downregulate Na<sup>+</sup> current, so we hypothesized that stimulation of VIP-INs with carbachol would worsen their function in *Scn1a*<sup>+/-</sup> mice. Bath application of 5 μM carbachol both depolarized and modulated the firing pattern of WT VIP-INs as we showed previously (Figure 2 A). However, stimulating VIP-INs with slow depolarizing ramps before and after carbachol application also revealed that the dynamic range of VIP-INs was shortened as they more readily entered depolarization block (Figure 1 B), consistent with Na<sup>+</sup> channel downregulation. VIP-INs from *Scn1a*<sup>+/-</sup> mice, however, fired at lower frequencies before application of carbachol (42 ± 2.9 vs. 34 ± 2.5 Hz, WT vs. *Scn1a*<sup>+/-</sup>, p = 0.04), and cholinergic modulation caused a massive decrease in their excitability. In fact, many VIP-INs from *Scn1a*<sup>+/-</sup> mice made a near-immediate transition to depolarization firing only 1-2 APs in response to slow depolarizing ramps (Figure 2 B-E, carbachol AP index, -0.21 ± 0.06 vs. -0.63 ± 0.06, WT vs. *Scn1a*<sup>+/-</sup>, p = 0.00003). This was true for all VIP-INs regardless of their initial firing pattern, (i.e. continuous adapting or irregular spiking; Goff and Goldberg, 2019; Figure S6). In addition, we performed voltage clamp recordings in VIP-INs from WT mice and found that bath application of carbachol led to a reversible decrease in Na<sup>+</sup> current (Figure 2 F-G). This confirms a mechanism whereby VIP-IN function is further impaired in *Scn1a*<sup>+/-</sup> mice during periods of high cholinergic tone both *in vitro* and *in vivo* through Na<sup>+</sup> channel downregulation.

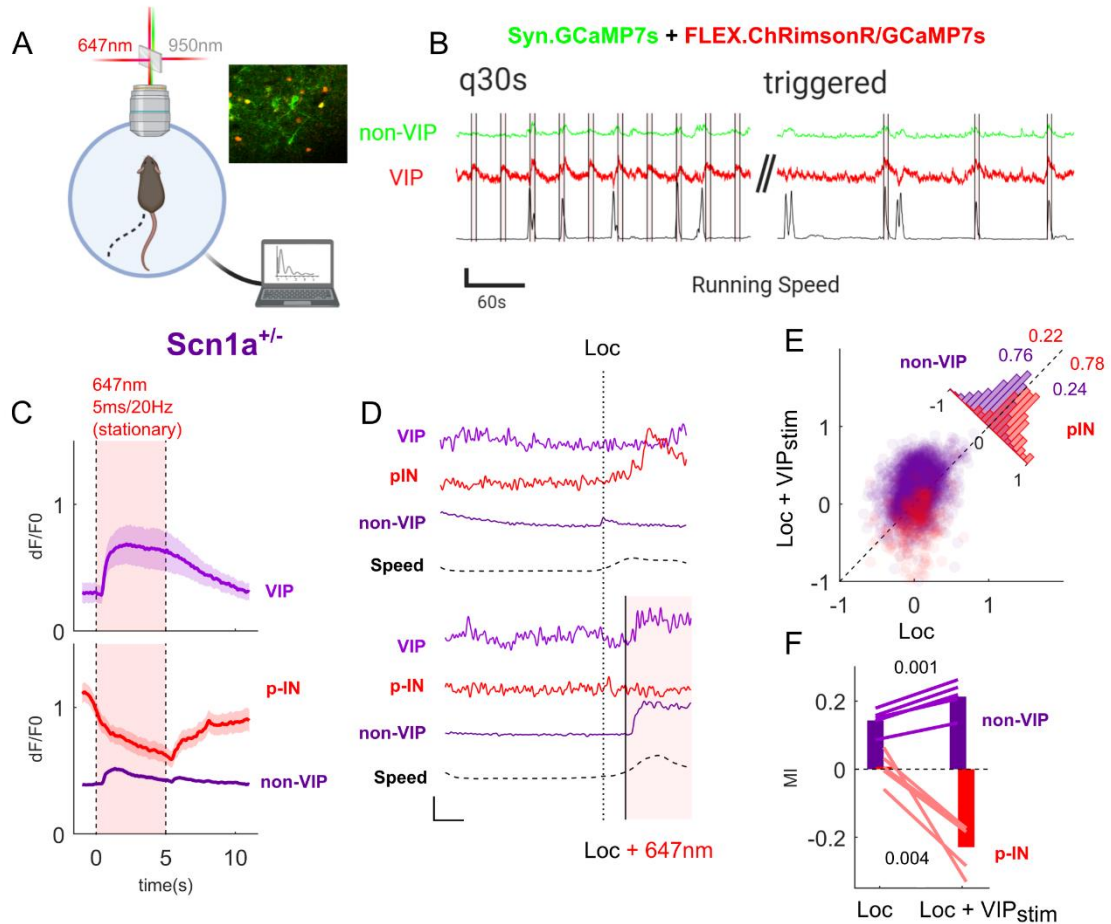


**Figure 3. Optogenetic activation of VIP-INs during locomotion bouts restores aspects of normal cortical dynamics in *Scn1a*<sup>+/-</sup> mice.** A) Schematic of experimental design, as in figure 3A. In addition to recording neural activity, a 1-P laser with a  $\lambda = 647\text{nm}$  was directed through the imaging objective for photoactivation of Crimson. B) Gcamp7s fluorescence was aligned to locomotion data as before, and VIP-INs expressing ChRimsonR.mCherry were stimulated for 5 s with 20Hz/5ms red light pulses either every 30 seconds (q30s) or triggered by the onset of locomotion with a 60 second time-out period in between stimulations (triggered). In this way, we ensured that stimulation epochs occurred during both locomotion and quiet resting periods for each mouse. The depicted neural data is an average of all cells within a single FOV. Scale bar; 0.5  $\text{dF}/\text{F}_0$ , 60 seconds. C) VIP-IN and non-VIP GCaMP7s fluorescent activity elicited by 5 second laser stimulation during stationary epochs. VIP-INs are uniformly activated as expected, and non-VIP neurons show a heterogenous response with an average disinhibitory response across most cells, and strong inhibition of approximately  $\sim 10\%$  of non-VIP cells which are likely the population of INs directly targeted by VIP-INs (p-INs). Lines and shaded area represent mean  $\pm$  95% CI. D) Example  $\text{dF}/\text{F}_0$  traces from a single VIP-IN, p-IN, and non-VIP neuron aligned to a single locomotion bout with and without concurrent laser stimulation. The lower dotted line represents running speed, the vertical dotted line is the detected locomotion onset (Lon) and the solid line and shaded area represents laser stimulation. Scale bar; 1  $\text{dF}/\text{F}_0$  or 100  $\text{mm}/\text{s}$ , 2 seconds. E) The

locomotion modulation index was calculated for each non-VIP neuron separately for locomotion epochs either with optogenetic VIP-IN activation (Loc + VIP<sub>stim</sub>) or without (Loc) compared to quiet wakefulness with no direct VIP-IN activation. 76% of non-VIP neurons show a greater locomotion modulation index with concurrent VIP-IN activation, while 78% of p-INs have a lower (more negative) modulation index with concurrent VIP-IN activation (inset histogram). F) The average locomotion MI for all non-VIP neurons and p-IN with or without VIP-IN stimulation. Lines represent the average response of individual *Scn1a*<sup>+/-</sup> mice, and bars represent the grand average of all mice. *n* = 3,246 non-VIP and 69 VIP cells from *n* = 5 *Scn1a*<sup>+/-</sup> mice. Within group comparisons made with a paired student's t-test using the average of each mouse.

---

## **Closed loop VIP-IN optogenetic stimulation rescues abnormal network dynamics**

### **in *Scn1a*<sup>+/-</sup> mice**

The above results suggest that enhancing VIP-IN activity during CSTs could potentially restore normal network dynamics in *Scn1a*<sup>+/-</sup> mice. To test this, we performed simultaneous 2P imaging with *in vivo* optogenetic activation of VIP-INs using the red shifted opsin ChRimsonR (Klapoetke et al., 2014). We found this reliably activated VIP-INs during quiescent periods, resulting in local disinhibition of many non-VIP cells (Figure 3 A-C). There was a small population of cells that were inhibited by VIP-IN activation which had high baseline activity and low skew calcium traces, likely comprised of putative INs (p-INs) directly targeted by VIP-INs (Figure S6). Optogenetic photoactivation of VIP-INs during locomotion bouts in *Scn1a*<sup>+/-</sup> mice restored network activity during CSTs to WT levels (Figure 3 D-F, modulation index,  $+0.07 \pm 0.006$ ;  $p = 0.001$ ), while the activity of p-INs was dramatically reduced ( $-0.23 \pm 0.04$ ;  $p = 0.004$ ). Therefore, direct activation of VIP-INs rescued local cortical circuit function in *Scn1a*<sup>+/-</sup> mice by enhancing inhibition of inhibitory INs and disinhibiting target principal cells.

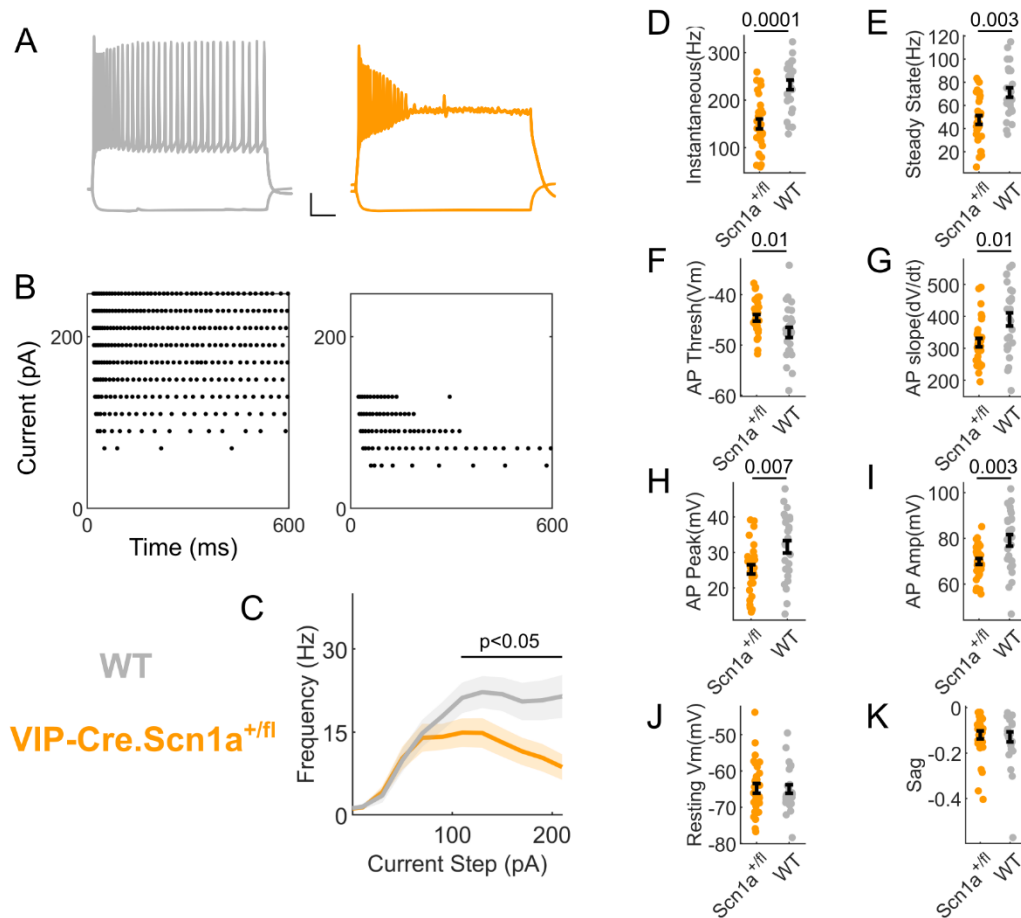


**Figure 4. VIP-IN specific loss of *Scn1a* recapitulates the cellular deficits observed in VIP-INs in global *Scn1a*<sup>+/-</sup> mice** A) Voltage response of a WT and VIP-Cre.*Scn1a*<sup>+/-</sup> VIP-IN to a -50 pA and a 2X rheobase 600ms square current injection. Scale bar = 15 mV and 100 ms. B) Raster plots for all APs elicited from the cells in A in response to increasing 600ms current injections. The *Scn1a*<sup>+/-</sup> cell enters depolarization block starting at 100 pA (shown in A), while the WT VIP-IN continues firing past 250 pA. C) Current frequency relationship for all cells recorded as in A-B. (D) Bar graphs showing individual cell values (dots) and the population mean ± SEM for the maximal instantaneous firing frequency of each cell. E) Same for the maximal Steady State firing frequency (APs during a single 600ms current injection). F – I) Several properties of single action potentials including F) Action potential voltage threshold G) AP maximum rise slope H) AP peak voltage and I) amplitude (Peak – threshold). J-K) Other intrinsic properties of VIP-INs which do not directly reflect function of voltage-gated Na<sup>+</sup> channels are unaffected including J) Resting membrane potential and K) voltage sag in response to a -50 pA square current injection. *n* = 30 VIP-INs from 4 VIP-Cre.*Scn1a*<sup>+/-</sup> mice, and *n* = 27 VIP-INs from 4 WT mice.

## Conditional deletion of *Scn1a* in VIP-INs recapitulates physiology and circuit deficits

In order to better delineate the specific contributions of VIP-INs to DS-related phenotypes, we crossed *Scn1a*<sup>+/*fl*</sup> mice to VIP-Cre mice to generate VIP-Cre.*Scn1a*<sup>+/*fl*</sup> mice in which *Scn1a* loss was genetically limited to VIP-INs. Consistent with the primarily disinhibitory role of VIP-INs, 0 of 60 of these mice had observable seizures or sudden unexpected death (SUDEP) prior to experimental end points or sacrificing at >P150, and 0 of 8 had temperature induced seizures at P21 (up to 42.5° C). We then confirmed the intrinsic electrophysiological phenotype of VIP-INs is also present in VIP-Cre.*Scn1a*<sup>+/*fl*</sup> mice as in *Scn1a*<sup>+/-</sup> mice. VIP-INs in VIP-Cre.*Scn1a*<sup>+/*fl*</sup> mice showed nearly identical deficits in AP generation and repetitive firing compared to their WT littermates, including decreased maximum instantaneous and steady state firing frequencies, as well as elevated AP threshold, and lower amplitude, peak voltage, and maximum AP rise slope (Figure 4).

We next measured the *in vivo* activity of VIP-INs and local non-VIP neurons in VIP-Cre.*Scn1a*<sup>+/*fl*</sup> mice and WT littermates using 2P calcium imaging. Interestingly, we found a qualitatively different deficit in VIP-Cre.*Scn1a*<sup>+/*fl*</sup> mice compared to what we showed for the global *Scn1a*<sup>+/-</sup> model. Rather than having decreased modulation at the onset of locomotion, deconvolved event frequency was decreased at rest in *Scn1a*<sup>+/*fl*</sup>.VIP-Cre mice (Figure 5 A-C, arbitrary units,  $-0.03 \pm 0.003$ ;  $p = 0.04$ ). Unexpectedly, the dynamics of calcium signals from VIP-INs were similar in both genotypes. We hypothesized that VIP-IN and network activity may remain state-dependent under enhanced cholinergic states beyond spontaneous locomotion. To test

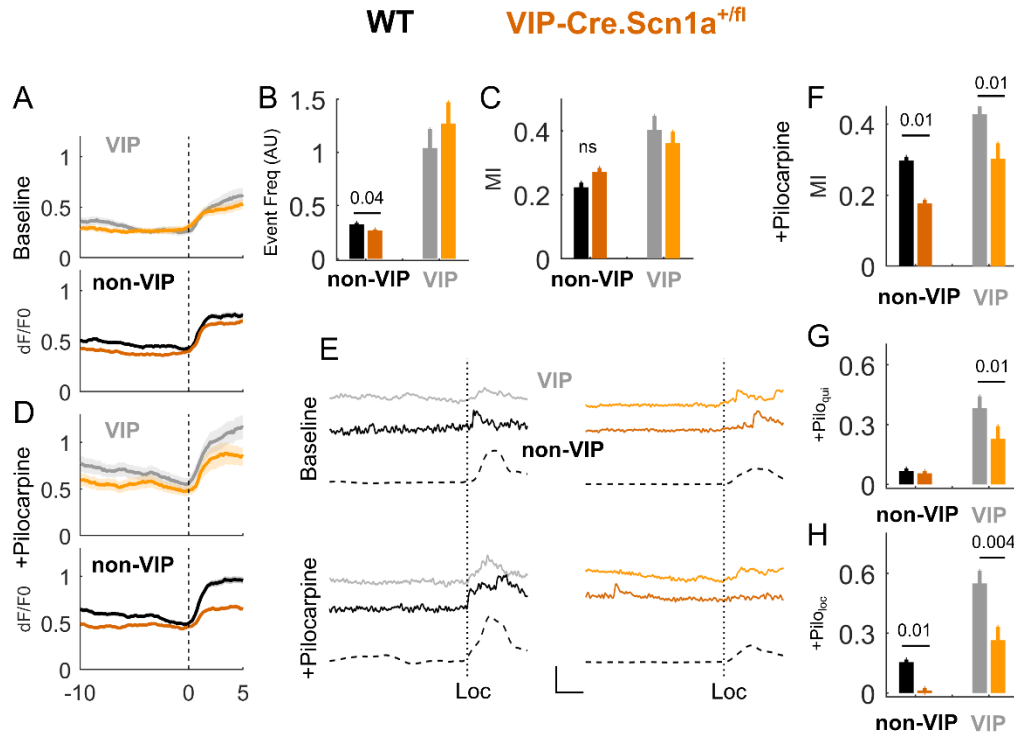


**Figure 5. Loss of *Scn1a* in VIP-INs produces circuit deficits *in vivo* that are exacerbated by muscarinic activation.** A) Average  $dF/F_0$  for all VIP-INs and non-VIP neurons aligned to the onset of locomotion in WT and *Scn1a*<sup>+/-</sup> mice (as in Figure 1D). B) Deconvolved event frequency during stationary epochs. C) Locomotion MI as in Figure 1E. D) Averaged  $dF/F_0$  response, as in A, aligned to locomotion bouts after the injection of 10mg/kg pilocarpine. E) Left: Example of the  $dF/F_0$  trace from a single VIP and non-VIP neuron aligned to a single locomotion bout, below is the same cell after IP injection of pilocarpine. Right: same but for example cells from and *Scn1a*<sup>+/-</sup> mouse. F) Locomotion MI of VIP-IN and non-VIP neurons after injection of pilocarpine. G) The effect of pilocarpine on deconvolved firing frequencies during stationary epochs calculated as an index value. H) The same as G but for locomotion epochs. For A-C, n = 3343 tdT<sup>-</sup> and 232 VIP-INs from N = 6 WT mice, n = 3552 tdT<sup>-</sup> and 316 VIP-INs from N = 7 *Scn1a*<sup>+/-</sup> mice. For D-H, n = 2068 tdT<sup>-</sup> and 119 VIP-INs from N = 6 WT mice, n = 2384 tdT<sup>-</sup> and 178 VIP-INs from N = 7 *Scn1a*<sup>+/-</sup>. All cells in D-H were recorded before and after injection of pilocarpine.

this hypothesis, we injected each mouse for a subset of imaging fields with a low dose of the muscarinic agonist pilocarpine (10mg/kg) to boost VIP-IN activity, and potentially recruit the Na<sup>+</sup> channel downregulation mechanisms that magnifies the difference between WT and *Scn1a*<sup>+/-</sup> cells (Figure 5 D-F). We compared how pilocarpine modulated

the activity of individual cells within the same imaging field in both stationary and locomotion epochs. Overall, pilocarpine caused a rise in the deconvolved event rate of VIP-INs, with a greater increase in WT VIP-INs compared to those from *Scn1a<sup>+/fl</sup>*.VIP-Cre mice during both stationary (pilocarpine index,  $-0.1 \pm 0.06$ ;  $p = 0.01$ ) and locomotion ( $-0.3 \pm 0.1$ ;  $p = 0.004$ ) epochs. There was also an increase in non-VIP-IN activity that was greater in WT mice during locomotion epochs (pilocarpine index,  $-0.15 \pm 0.06$ ;  $p = 0.01$ ). Overall, this locomotion modulation index of VIP and non-VIP neurons increased in WT mice but decreased it in *Scn1a<sup>+/fl</sup>*.VIP-Cre mice resembling what is found in the global DS model (Figure 5 G). Therefore, VIP-IN mediated dysfunction persists and is modulated by cholinergic brain states in *Scn1a<sup>+/fl</sup>*.VIP-Cre mice.

### **Loss of *Scn1a* in VIP-INs causes ASD and ID endophenotypes**

Based on our results from both *Scn1a<sup>+/-</sup>* and *Scn1a<sup>+/fl</sup>*.VIP-Cre mice, we hypothesized that cell intrinsic dysfunction of VIP-INs in DS could give rise to pathological behaviors linked to abnormal disinhibitory circuits. VIP-INs have a relatively well conserved disinhibitory role across the neocortex and hippocampal formation, and are important for spatial memory, sociability, and sensory processing. Many of these behaviors are linked to the pathophysiology of ASD and ID overlap with dysfunctional behaviors found in *Scn1a<sup>+/-</sup>* mice. We tested whether any of the ASD and ID endophenotypes found in DS models were present in *Scn1a<sup>+/fl</sup>*.VIP-Cre mice. We used paradigms to probe social behavior, spatial memory, anxiety, and repetitive motor behavior. VIP-Cre.*Scn1a<sup>+/fl</sup>* mice interacted less with a novel mouse over a novel object in a 3 chamber task (social index,  $-0.14 \pm 0.05$ ;  $p = 0.009$ ), buried more marbles ( $+0.16\% \pm 0.05$ ;  $p = 0.005$ ), and showed no preference for a novel object at 24h during a



novel object recognition (NOR) task compared to their WT littermates (object preference index,  $-0.16 \pm 0.06$ ;  $p = 0.01$ ). However, there were no differences in open field activity, or time spent in the open arms of an elevated plus maze (EPM) compared to WT littermates. Therefore, VIP-Cre.*Scn1a*<sup>fl/fl</sup> mice show several abnormal behaviors consistent with the global DS model and conserved among other models of ASD (Han et al., 2012; Mossner et al., 2020).

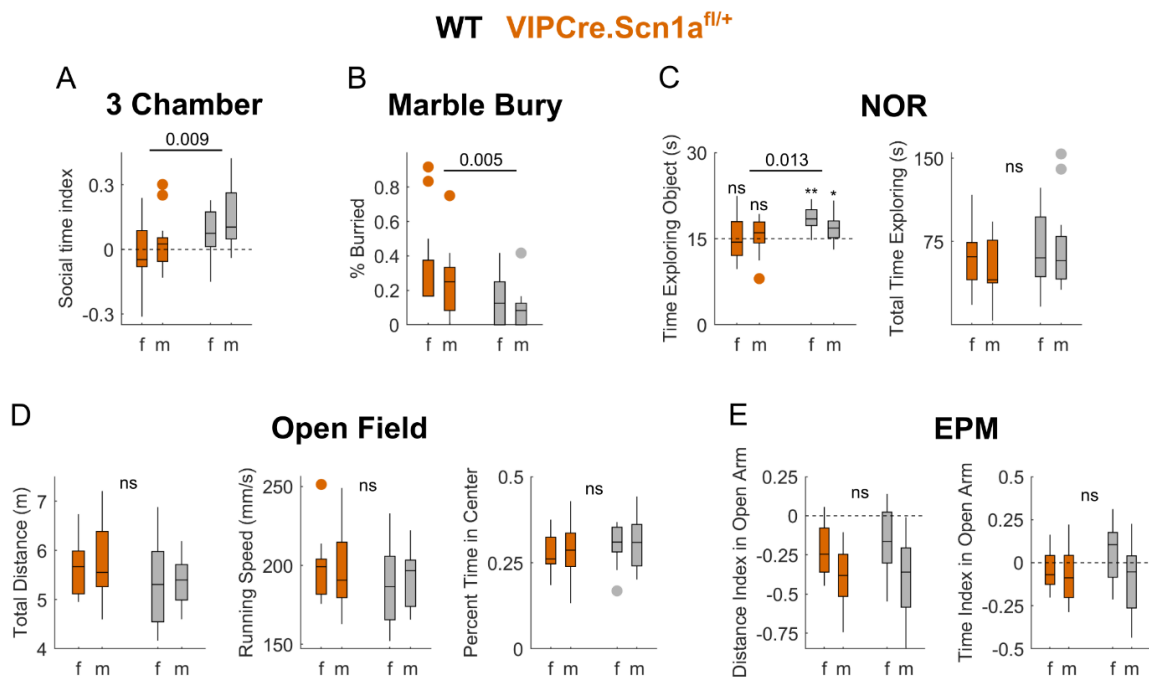


**Figure 6. Loss of *Scn1a* in VIP-INs replicates core cognitive impairments and ASD endophenotypes of the global *Scn1a*<sup>+/−</sup> DS model.** A) Social interaction index for time spent with a novel conspecific mouse under a holding cage vs. an identical cage in the opposite chamber. B) Percent of marbles buried during a 30-minute period in an individual cage. C) Left: Time exploring a novel object during the first 30 seconds of exploration. 15 seconds (dotted line) represents equal time spent exploring the novel and familiar object. \*,  $p < 0.05$ ; \*\*,  $p < 0.01$  for within group comparisons indicating significantly more time spent with the novel object vs. the familiar object. Right: Total time spent exploring both the novel and familiar object during a 5-minute test period. D) Left: total distance travelled during a 15-minute open field period. Center: Running speed, calculated as the top 10<sup>th</sup> percentile in speed for each mouse. Right: Percent of

total time spent in the center of the arena. E) Left: Index of Distance travelled in the open arm of the elevated plus maze. Right: Index of the total time spent exploring the open arm. An index of 0 (dotted line) indicates equal time/distance in the open/closed arm. A-D) All data are shown as violin plots where the lines represent 5-95% of the population distribution, the box represents 25-75%, and the middle line is the median value of each group. Outliers that are > 1.5 the interquartile range are plotted as separate points but are still included in the analysis. Data from male and female (m/f) mice are plotted separately, and p-values represent comparisons between genotypes using a mixed effects model (see materials and methods). N = 26 VIPCre.*Scn1a<sup>fl/+</sup>* and n = 23 WT mice.

---

## DISCUSSION

In this study we explored the known circuit functions of VIP-INs related to a devastating neurological disorder and investigated the *in vivo* impact of VIP-IN dysfunction as it relates to the so-far enigmatic and untreatable ASD and ID comorbidities of DS. Our main questions were: 1) how does impaired VIP-IN excitability as observed in *Scn1a<sup>+/-</sup>* mice *in vitro* alter the *in vivo* disinhibitory circuit function subserved by this important class of INs, and 2) does cellular and circuit dysfunction of VIP-INs *in vivo* translate to abnormal ASD-linked behaviors that define DS. We found that heterozygous loss of *Scn1a* produces profound circuit and network level defects in neocortex which are at least partially caused by VIP-IN intrinsic dysfunction and can be rescued by enhancing VIP-IN activity during CSTs. Additionally, selective VIP-IN dysfunction gives rise to features of ASD and ID independent of seizures. Overall, our work expands our understanding of the role of VIP-INs in the pathogenesis of DS and more broadly in ASD and ID.

### **2P imaging in V1 reveals VIP-IN dysfunction and an abnormal disinhibitory microcircuit in *Scn1a<sup>+/-</sup>* mice**

We focused on one of the most widely reproduced and well-studied aspects of *in vivo* VIP-IN function using 2P calcium imaging to simultaneously assess their activity

and their impact on the local network. We found that CSTs – which align with active behavioral states – are impaired in *Scn1a*<sup>+/-</sup> mice, with lower VIP-IN and network activity during active behavioral states. CSTs are largely driven by ascending cholinergic and noradrenergic tone in sensory cortices, so we also performed simultaneous pupillometry which accurately tracks this form of neocortical input (Reimer et al., 2014). We found that the correlation structure of both VIP-INs and local excitatory neurons was degraded in *Scn1a*<sup>+/-</sup> mice, with fewer VIP-INs positively correlated to pupil diameter, decreased correlation between VIP-IN and network activity, and a shift from a general disinhibitory response to a push-pull type response in local network activity. Interestingly, network activity in V1 of *Scn1a*<sup>+/-</sup> mice resembles normal dynamics in prefrontal cortex during similar active behaviors, where SST-INs compete more aggressively with VIP-INs and cause nearly equal amounts of opposing inhibition (Garcia-Junco-Clemente et al., 2017). Our general underlying framework is that VIP-INs are now being outcompeted by other inhibitory INs in V1 in *Scn1a*<sup>+/-</sup> mice, consistent with data that shows multiple other IN types regaining excitability in adult mice (Favero et al., 2018, Almog et al., 2021, Kaneko et al., 2021). As such, optogenetically stimulating VIP-IN activity during active behaviors reinstates normal network dynamics by silencing a small population of neurons, likely representing INs targeted directly by VIP-INs. Overall, this indicates that boosting VIP-IN function corrects the circuit deficits found in *Scn1a*<sup>+/-</sup> mice.

Conditional deletion of Nav 1.1 in VIP-INs also was able to reproduce the intrinsic electrophysiological phenotype found in *Scn1a*<sup>+/-</sup> mice, as well as altered cortical dynamics consistent with decreased disinhibition. Overall network activity was reduced in *Scn1a*<sup>+fl</sup>.VIP-Cre mice, however VIP-IN activity as measured by 2P imaging was similar between WT and *Scn1a*<sup>+fl</sup>.VIP-Cre mice. This indicates that loss of Nav1.1 in

VIP-INs causes decreased local network activity, although why this is not reflected in VIP-IN activity is unclear. One explanation is that VIP-IN cellular deficits are too subtle to reflect in the calcium dynamics recorded at the soma of VIP-INs, but the enhanced circuit deficit (in both *Scn1a*<sup>+/-</sup> and VIP-Cre.*Scn1a*<sup>+fl</sup> mice) is the result of a combination of both impaired spike generation and propagation (Kaneko et al., 2021). Layered on top of this is the possibility that other disinhibitory INs in the circuit could be compensating for decreased VIP-IN function, as compensation in other IN subtypes clearly occurs (Favero et al., 2018, Almog et al., 2021). Likely candidates are the NDNF expressing INs, which target PV-INs and are also partially responsible for disinhibition occurring during locomotion (Cohen-Kashi Malina et al., 2021; Takesian et al., 2018; Tasic et al., 2016). NDNF-INs likely express Nav1.1 based on single cell RNA-seq data (Tasic et al., 2016; Yao et al., 2021) which may indicate that these cells are dysfunctional in *Scn1a*<sup>+/-</sup> mice, but are unimpaired when Nav1.1 deletion is experimentally limited to VIP-INs.

Nevertheless, while baseline *in vivo* VIP-IN activity was not different in *Scn1a*<sup>+fl</sup>.VIP-Cre mice, VIP-INs were sensitive to increased cholinergic tone *in vivo* similar to our results in acute slices. Low dose pilocarpine greatly boosted the activity of VIP-INs in WT mice *in vivo* yet had a markedly reduced effect in *Scn1a*<sup>+fl</sup>.VIP-Cre mice. In the setting of elevated cholinergic tone, we observed deficits in the modulation of VIP-IN and network activity that closely resembled that seen in the global *Scn1a*<sup>+/-</sup> mice. We interpret this data as evidence for context/brain state-dependent VIP-IN dysfunction in *Scn1a*<sup>+fl</sup>.VIP-Cre mice.

### **VIP-IN dysfunction underlies ASD and ID endophenotypes but not epilepsy**

Ultimately, *Scn1a*<sup>+/fl</sup> mice showed behavioral abnormalities consistent with the global DS model and other models of ASD yet were seizure free and did not exhibit premature lethality. Therefore, VIP-INs do not contribute to the seizure phenotype of DS, but instead give rise to non-seizure features of DS including ASD and ID. The disinhibitory circuit function of VIP-INs is remarkably conserved in various neocortical regions as well as the hippocampus and amygdala (Guet-McCreight et al., 2020; Krabbe et al., 2019; Turi et al., 2019), and VIP-INs are consistently impaired in *Scn1a*<sup>+/-</sup> mice across multiple sensory cortices (Goff & Goldberg, 2019). Recent large scale single cell RNA sequencing work has demonstrated that IN subtypes, while diverse, tend to show consistent expression patterns across disparate regions of the neocortex and hippocampal formation indicating that VIP-IN dysfunction in *Scn1a*<sup>+/-</sup> mice could be widespread (Gouwens et al., 2020; Yao et al., 2021). Future work could help identify which VIP-IN population(s) in which brain region(s) contribute to the ASD and ID behavioral abnormalities in DS. For instance, VIP-INs in the hippocampus appear to play a critical role in the remapping of place cells (Turi et al., 2019), which theoretically could affect spatial learning tasks in DS mice. Taking a deeper look at V1, VIP-INs also shape sensory processing in complex ways, boosting gain on small but salient stimuli, discriminating between novel and familiar images, and coordinating an interaction between arousal and visual processing (de Vries et al., 2020; Garrett et al., 2020; Khan et al., 2018; Millman et al., 2020). Future work could also identify the impact of VIP-IN dysfunction on these important computational processes in DS and other neurodevelopmental disorders.

While many studies have replicated how various IN subtypes are impaired by loss of Nav1.1 *in vitro*, this is the first to show hypofunction of a particular subtype *in*

*vivo*. Our work demonstrates that VIP-IN activity is impaired in a mouse model of DS, leading to abnormal *in vivo* disinhibitory microcircuit function and attenuated CSTs. This is due to intrinsic Na<sup>+</sup> channel deficiency and compounded by the effect of ascending cholinergic modulation of Na<sup>+</sup> current density of VIP-INs in *Scn1a*<sup>+/-</sup> mice. VIP-IN dysfunction may be a common locus of cellular dysfunction in models of ASD, and here may underlie comorbid ASD and ID endophenotypes independent of any direct role in epilepsy. Indeed, genes implicated in ASD and ID are enriched in VIP-INs, while transcripts of epilepsy-linked genes are enriched in PV-INs (Goff & Goldberg, 2021). Therefore, manipulation of VIP-IN activity could represent a therapeutic strategy across a range of neurodevelopmental disorders. Our data also suggest that the durable ASD and ID features of DS, which persist through patients' lives while seizures tend to improve over time, could potentially be addressed later in life by enhancing VIP-IN function. Conversely, using seizure control as an output measure may not be the optimal approach for the development of meaningful therapeutic approaches for DS. VIP-INs represent a targetable nexus of dysfunction common to a diverse set of neurological conditions, highlighting the importance of developing new cell type specific tools and therapies.

## MATERIALS AND METHODS

<b>Table 1. Key Resources</b>				
Reagent type (species) or resource	Designation	Source	Identifiers	Additional information
Genetic reagent ( <i>M. musculus</i> )	129S- <i>Scn1atm1Kea/Mmjax</i>	Jax	RRID:MMRRC_037107-JAX	Dr. Jennifer A. Kearney, Northwestern University
Genetic reagent ( <i>M. musculus</i> )	<i>Viptm1(cre)Zjh/J</i>	Jax	RRID:IMSR_JAX:010908	
Genetic reagent ( <i>M. musculus</i> )	B6;129P2- <i>Pvalbtm1(cre)Arbr/J</i>	Jax	RRID:IMSR_JAX:008069	
Genetic reagent ( <i>M. musculus</i> )	B6J.Cg- <i>Ssttm2.1(cre)Zjh/MwarJ</i>	Jax	RRID:IMSR_JAX:028864	
Genetic reagent ( <i>M. musculus</i> )	B6.129X1(SJL)- <i>Scn1atm2.1Wac/Mmucd</i>	UC Davis	RRID:MMRRC_041829-UCD	
Genetic reagent ( <i>M. musculus</i> )	129S6.SvEvTac	Taconic	RRID:IMSR_TAC:129sve	
Genetic reagent ( <i>M. musculus</i> )	C57BL/6J	Jax	RRID:IMSR_JAX:000664	
recombinant DNA reagent	AAV.CAG.Flex.tdTomato	Penn Vector Core	AV-9-ALL864	2XE+12 GC/mL
recombinant DNA reagent	AAV.syn.Flex.Gcamp7s			7.5XE+12 GC/mL
recombinant DNA reagent	AAV.syn.Gcamp7s			
chemical compound,	Carbamoylcholine chloride	Sigma	C4382	5 $\mu$ M

drug				
chemical compound, drug	Pilocarpine hydrochloride	Sigma	P6503	10mg/kg IP injection
software, algorithm	Pclamp 10	Clampfit		V10.0
software, algorithm	Matlab	Mathworks		2021a
software, algorithm	Gramm	10.21105/joss.00568		Data visualization for Matlab
software, algorithm	Python			v3.7.1
software, algorithm	Deeplabcut (Deeplabcutcore)	Mathis et al 2018	0.0b3	Nvidia RTX3090 compatible (added to DLC > v2.2)
software, algorithm	Mobile Home Cage	Neurotar		Locomotion Tracking Software
software, algorithm	FlyCapture2	Point Grey (now FLIR)		SDK for acquiring video

### *Experimental animals*

All procedures and experiments were approved by the Institutional Animal Care and Use Committee at the Children’s Hospital of Philadelphia and were conducted in accordance with the ethical guidelines of the National Institutes of Health. For 2P imaging experiments and slice electrophysiology, male and female mice were used in equal proportions. For mouse behavior experiments, both sexes were used, and sex was considered in our statistical design (see below); no sex-specific differences were identified unless otherwise noted, in which case the data was pooled. After weaning at



P21, mice were group-housed with up to 5 mice per cage and maintained on a 12-hour light/dark cycle with ad libitum access to food and water.

Mouse strains used in this study included: *Scn1a*<sup>+/-</sup> mice on a 129S6.SvEvTac background (RRID:MMRRC\_037107-JAX) generated by a targeted deletion of exon 1 of the *Scn1a* gene, VIP-Cre mice (Viptm1(cre)Zjh/J; RRID:IMSR\_JAX:010908 on a mixed C57BL/6;129S4 background), PV-Cre mice (B6;129P2-Pvalbtm1(cre)Arbr/J; RRID:IMSR\_JAX:008069), SST-Cre mice (B6J.Cg-Ssttm2.1(cre)Zjh/MwarJ; RRID:IMSR\_JAX: 028864), wild-type 129S6.SvEvTac (Taconic Biosciences model #129SVE; RRID:IMSR\_TAC: 129sve), and wild-type C57BL/6J (RRID:IMSR\_JAX:000664). *Scn1a*<sup>+fl</sup> mice (RRID:MMRRC\_041829-UCD) were rederived from frozen embryos in the CHOP mouse genetics core.

Female VIP-Cre homozygous mice were crossed to male 129S6.*Scn1a*<sup>+/-</sup> mice to generate *Scn1a*.VIP-Cre mice and WT VIP-Cre littermate controls. The genotype of all mice was determined via PCR of tail snips obtained before P10. All mice used for experiments were on a near 50:50 129S6:B6J background, and *Scn1a*<sup>+/-</sup> mice on this background have been shown to replicate the core phenotype of Dravet Syndrome (Miller et al., 2014; Mistry et al., 2014). We previously confirmed that this particular breeding configuration had similar rates of SUDEP and epilepsy expected (Goff and Goldberg. 2019). The same approach was used to generate VIP-Cre.*Scn1a*<sup>+fl</sup> mice and WT VIP-Cre littermate controls, however these mice are on a pure B6J background and thus WT control groups were not combined. Additionally, both male and female *Scn1a*<sup>+fl</sup> were used for breeding.

*AAV9 injections and Cranial window implantation*

Mice that were used for slice electrophysiology recordings were injected at P0 with AAV9.CAG.Flex.tdTomato as described previously (Gao et al., 2019). Briefly, P0 mice were anesthetized on ice, and then subdurally injected with 1.5  $\mu$ l of AAV9 split between both hemispheres. For 2P imaging experiments, VIP-INS from double transgenic *Scn1a*.VIP-Cre and WT.VIP-Cre littermates from the cross described above were labeled via stereotaxic injection of AAV.CAG.Flex.tdTomato. >P35 mice were anesthetized with isoflurane (induction, 3-4%; maintenance, 1-1.5%) and body temperature and breathing were continuously monitored. A craniotomy 1 mm anterior and 3 mm lateral to lambda was made and virus was injected with a 50-75  $\mu$ m tip diameter glass pipette driven by a Nanoject III (Drummond Scientific). 60 nL of a mixture of AAV9.hSyn. GCaMP7s, AAV9.FLEX. GCaMP7s, and AAV9.FLEX.tdT diluted in sterile PBS was injected at 20 nL/min across 4-5 locations separated by at least 0.5 mm centered around primary visual cortex V1. The pipette was held in place for 5 min to allow the virus to spread at each injection location. Following virus injection, a cranial window made of a 3mm circular coverslip glued to a 5mm circular coverslip was affixed in place over the craniotomy, and a titanium headbar was cemented on top of the coverslip. All mice were given Buprenorphine-SR 0.5 mg/kg, cefazolin 500mg/kg, and dexamethasone 5mg/kg perioperatively and monitored for recovery and infection periodically for 48 hours following surgery.

#### *Acute slice preparation*

Mice were anesthetized with isoflurane and transcardially perfused with ice cold artificial cerebral spinal fluid (ACSF) containing (in mM): NaCl, 87; sucrose, 75; KCl, 2.5; CaCl<sub>2</sub>, 1.0; MgSO<sub>4</sub>, 6.0; NaHCO<sub>3</sub>, 26; NaH<sub>2</sub>PO<sub>4</sub>, 1.25; glucose, 10, and equilibrated with

95% O<sub>2</sub> and 5% CO<sub>2</sub>. The brain was removed and mounted on a holder of the Leica VT-1200S vibratome and sliced at 300-350 μm thickness. Slices were allowed to recover for 30 minutes in ACSF warmed to 30°C, then maintained at room temperature before recording. Slices were transferred to a recording chamber on the stage of a BX-61 upright microscope and perfused with recording solution at 30-32° C and 2-3 mL/min containing, in mM: NaCl, 125; KCl, 2.5; CaCl<sub>2</sub>, 2.0; MgSO<sub>4</sub>, 1.0; NaHCO<sub>3</sub>, 26; NaH<sub>2</sub>PO<sub>4</sub>, 1.25; glucose, 25.

### *Slice recordings*

VIP-INs were identified by tdT expression. Whole-cell recordings were obtained from superficial (layer 2/3) primary somatosensory cortex (S1; “barrel”) and visual cortex (V1) as described previously. Patch pipettes were pulled from borosilicate glass using a Narashigi PC-100 puller and filled with intracellular solution containing (in mM): K-gluconate, 130; KCl, 6.3; EGTA, 0.5; MgCl<sub>2</sub>, 1.0; HEPES, 10; Mg-ATP, 4.0; Na-GTP, 0.3; pH was adjusted to 7.30 with KOH, and osmolarity adjusted to 285 mOsm with 30% sucrose. Pipettes had a resistance of 4-6 MΩ when filled and placed in recording solution, with the majority having a resistance of 4.5 – 5 MΩ. Voltage was sampled at 50 kHz with a MultiClamp 700B amplifier (Molecular Devices), filtered at 10 kHz, digitized using a DigiData 1550A, and acquired using pClamp10 software. Recordings were discarded if the cell had an unstable resting membrane potential and/or a membrane potential greater than -50 mV, or if access resistance increased by > 20% during the recording. We did not correct for liquid junction potential. For experiments using carbachol, repeat measurements were made 5 minutes after wash-in and up to 30 minutes after wash-out of drug.

### *Electrophysiology data analysis*

All analysis was performed blind to genotype using custom written Matlab (Mathworks) code. Resting membrane potential ( $V_m$ ) was the average value of a 1 s sweep with no direct current injection. Input resistance ( $R_m$ ) was calculated using the responses to -10 to -50 pA hyperpolarizing current injections near rest using  $R_m = \Delta V/I$  for each sweep. AP threshold was the value at which the derivative of the voltage ( $dV/dt$ ) reached 10 mV/ms. Spike peak refers to the maximum voltage value of an individual AP, while spike amplitude is the difference between spike height and AP threshold. Maximum rise slope was taken as the max value of  $dV/dt$  during a single AP. Unless indicated, all quantification of single spike properties was done using the first AP elicited at rheobase.

Rheobase was determined as the minimum current injection that elicited APs using a 600 ms sweep at 10 pA intervals. Maximal instantaneous firing was calculated using the smallest inter-spike interval (ISI) elicited at near-maximal current injection (before entering depolarization block). Maximal steady-state firing was defined as the maximum number of spikes generated in a single 600ms sweep, with a minimum requirement for a spike being an amplitude of 40 mV and height overshooting at least 0 mV.  $I/f$  relationships were generated from 600ms current steps as well as from 8 second ramp depolarizations (Figure 1) as described previously. For Figure 1, the maximum instantaneous firing rate was calculated from the shortest ISI during a single 8 second ramp depolarization. The effect of carbachol on firing was calculated as an index value from the total number of spikes generated before ( $S_0$ ) and after ( $S_{carb}$ ) bath application of carbachol:

$$\frac{S_0 - S_{carb}}{S_0 + S_{carb}}$$

### *Voltage clamp recordings*

Na<sup>+</sup> currents were recorded in modified ACSF containing (in mM): NaCl, 125; KCl, 2.5; CaCl<sub>2</sub>, 2.0; MgSO<sub>4</sub>, 1.0; NaHCO<sub>3</sub>, 26; NaH<sub>2</sub>PO<sub>4</sub>, 1.25; glucose, 10; TEA-Cl, 10; CdCl<sub>2</sub>, 0.1. Pipettes had a resistance of 3-4 MΩ, and cells which were stable and had an access resistance < 20 MΩ for 5 minutes after break in were recorded using a series of 100 ms voltage steps from -80 to 50 mV. Peak current was calculated as the maximum absolute value of the current response. All values in Figure 1 were calculated using the peak current elicited at 0 mV.

### *In vivo 2-P calcium imaging*

Imaging was performed using a mode-locked pulsed infrared laser (18-30 mW, InSight, SpectraPhysics) controlled by a Pockels cell (Conoptics) on a commercial 2P microscope (Bruker) equipped with a resonant scanner (Cambridge Technology). A 16/0.8 NA water-immersion objective (Nikon) was used. GCaMP7s was imaged at 950 nm with a gallium arsenide phosphide photodetector (H7422-40, Hamamatsu). Simultaneously, tdT was imaged with a multi-alkali detector (R3896, Hamamatsu). For experiments using ChRimsonR.mCherry, a single reference image (average of 100 frames) was taken before and after each imaging field at 1020 nm to isolate and verify mCherry signal. Data were acquired and converted to .tif stacks for analysis. Fluorescence data was acquired at 30 Hz.

Approximately 3 weeks after headbar implantation, mice were allowed to habituate to head fixation in a floating Mobile Home Cage (Neurotar) in the imaging apparatus for 20-30 minutes daily for 5 days prior to the first imaging experiment. By the end of habituation, all mice showed spontaneous running bouts, occasional grooming, and the absence of escape or prolonged freezing behaviors. For test sessions, mice were allowed to freely 'move' in the floating chamber for 12-15 minutes. The chamber had a transparent siding, and a 7 inch LCD screen (resolution: 1024X600, refresh: 60Hz) displaying a greyscale image (mean luminance 50 cd/m<sup>2</sup>) was positioned 15 centimeters away from and perpendicular to the contralateral eye. Airflow into the Mobile Home Cage stage provided approximately pink noise during the experiment, measured at ~40-45 db. An infrared (IR) ccd camera (Grasshopper 3, Point Grey) was positioned 15 centimeters away from the ipsilateral eye, and the image field was adjusted to include the entirety of the pupil, whisker pad, and nose, illuminated by a IR light source (850nm). Pupillometry videos were acquired at 100Hz, and locomotion speed was tracked by the mobile home cage locomotion tracking software (Neurotar). Neural and behavioral data acquisition was synced by a TTL pulse at the start and end of each recording session, and all behavioral data was decimated to match the sample frequency of the fluorescence data prior to analysis. For *in vivo* optogenetics experiments, a separate TTL output from either a master9 (for q30s stimulation, A.M.P.I.) or the mobile home cage interface (running triggered stimulation) was used to trigger a red laser routed through the imaging objective (10 mW/mm<sup>2</sup>, 647 nm OBIS, Coherent). This combination of stimulation patterns was used to ensure that we collected sufficient epochs where there was: 1) Laser stimulation during quiescence, 2) Laser stimulation concurrent to locomotion, and 3) Locomotion epochs without laser stimulation.

For experiments with pilocarpine, a single FOV was recorded per mouse as above, then acquisition was stopped, and the mouse was given an intraperitoneal injection of 10mg/kg pilocarpine. After 10 minutes, the injection was verified by an increased pupil diameter and increased salivation by the mouse. Imaging and behavioral data acquisition was restarted after manually adjusting the 2P imaging field to landmarks such that the same cells were recorded before and after pilocarpine injection.

#### *Cell detection and extraction of neuron activity*

The Suite2p package was used for preprocessing of the acquired 2P calcium imaging data followed by cell detection and extraction of neural activity (Pachitariu et al., 2017). A non-rigid registration was implemented for the data set in which each image was divided into sub blocks for more accurate movement correction. Once the images were registered, alignment metrics were checked for quality of data and few sessions were excluded if z drift was detected. After registration, cells were detected as ROIs spatially located around the peaks of the smoothed principal components, and a blinded experimenter manually rejected non-cell ROIs that were erroneously assigned as cells. Fluorescence values were extracted from the detected cells and neuropil values are derived from the area around the cells across the imaging session. In cases where two imaging sessions on the same field of view were recorded in series (before and after pilocarpine injection, or using different optogenetic stimulation patterns), the resulting fluorescence data was aligned and combined prior to cell detection in suite2P.

#### *Normalization and background correction*

Because background fluorescence is correlated with locomotion, we adopted the method of diPoppa et al. (2018) for estimating the adjacent neuropil signal for each cell and finding the correct scaling factor for background subtracting. Suite2P was used to output a neuropil mask for each cell extending 30  $\mu\text{m}$  from each ROI, excluding regions belonging to other detected ROIs. Then, we determined the minimum cellular fluorescence that corresponded to the surrounding neuropil signal by binning the neuropil signal  $N_i(t)$  into 20 segments and calculating the 5<sup>th</sup> percentile of the cellular signal  $F_i(t)$  that corresponded to each bin. We then used linear regression to calculate the correction factor  $\alpha_i$  for each cell. To avoid overestimating  $\alpha_i$  with highly active cells which are strongly correlated to  $N_i(t)$ , for each FOV we averaged  $\alpha_i$  from sparsely firing cells with high skew values ( $>4$ ) to give a correction value for that experiment  $\alpha_{FOV}$  (Figure S2). For a minority of FOVs that did not have at least 20 high skew cells, we used an average correction factor from all other FOVs  $\langle \alpha_{FOV} \rangle = 0.62$ .

### *Analysis of neural activity*

Fluorescence values in all figures are reported as  $dF(t)/F_0 = (F(t) - F_0)/F_0$ , where  $F_0$  is the 10th percentile of each neuron's fluorescence trace.  $F_0$  was adjusted for long ( $>6$  minute) recording sessions by using a linear interpolation between the average  $F_0$  values for the first and second half of the recording.

To measure how neural activity is modulated by locomotion, we calculated a modulation index MI for each cell by separating the entire neural trace into 1 s and computing the average activity  $F(t)$  for each. These chunks were separated based on the average running speed  $V(t) > 25\text{mm/s}$  into locomotion (FL) and quiescent (FQ) epochs. MI was calculated for each cell as



$$MI = \frac{\langle F^L \rangle - \langle F^Q \rangle}{\sqrt{(\sigma^2[F^L] + \sigma^2[F^Q])}}$$

For Figure 3, MI was calculated independently for  $F^L$  chunks which also had concurrent red-light stimulation during at least 15 of 30 sample points within the chunk length. Chunks with between 1-15 sample points where there was red-light stimulation were discarded. Using this method, we were able to combine the q30s and triggered data sets, although our results were nearly identical if we separated our analysis based on stimulation pattern (not shown).

A Pearson correlation coefficient was used to describe the relationship between neural activity and pupil diameter  $r_p$ . We then used a shuffle test to determine whether an individual cell was either positively or negatively correlated with pupil diameter. Briefly, neural data was divided into 1s chunks and randomly shuffled  $n = 10000$  times, then  $r_n$  was recalculated for each cell in each shuffle to give a distribution of values  $r_N$ . A cell was considered to be positively or negatively correlated with pupil diameter if  $r_p > P_{95}(r_N)$  or  $r_p < P_5(r_N)$  after correcting for multiple comparisons.

For demonstration purposes, we extracted individual running bouts defined by a duration of running of at least 5s preceded by 10s of quiescence. We then averaged the  $dF(t)/F_0$  trace for each cell across running bouts and plotted the grand averaged and bootstrapped 95% CI across all cells.

We additionally extracted deconvolved 'spiking' event trains  $S(t)$  for some analyses. Briefly, after calculating  $dF(t)/F_0$  for each cell as described above, we used the OASIS deconvolution algorithm to extract  $S(t)$ . In order to tune the values for the

transient decay constant ( $\tau$ ) and noise floor, we randomly selected a high skew ( $>2.5$ ) non-VIP neuron and a moderately high skew ( $>1$ ) VIP-IN from each FOV and used a simple threshold to extract a template kernel from each trace. We then fit the decay time of the kernel as well as the noise floor and averaged across all FOVs used these values across all experiments.

We then used a previously described de-noising algorithm to remove low amplitude events that are near the noise floor. Briefly, the maximum of  $S(t)$  was scaled to the maximum of  $dF(t)/F_0$  for each cell, and then calculated the median absolute deviation  $\sigma_i$  of  $dF_i/F_0$ . We then binned  $S(t)$  into 100ms intervals and set the value of each bin equal to zero if it fell below a multiple of the noise level  $n \times \sigma_i$  where  $n = 3$ .

For calculating the modulation index based on ne-noised deconvolved events  $S(t)$  from each cell, we segmented the chunked data in the same way into locomotion ( $S^L$ ) and stationary ( $S^Q$ ) epochs, and used the simplified formula:

$$MI_S = \frac{\langle S^L \rangle - \langle S^Q \rangle}{\langle S^L \rangle + \langle S^Q \rangle}$$

We found that the calculation of locomotion MI using either event traces or  $dF(t)/F_0$  yielded very similar results. We included analyses using event trains primarily as a tool to describe the baseline activity of neurons independent of locomotion or any external stimulus, or to compare activity within the same cell across conditions (e.g. +/- pilocarpine). However, because the exact relationship between spiking and calcium

fluorescence likely differs between cell types, we did not attempt to estimate exact firing rates for any cells or compare firing rates across cell types.

### *Mouse Behavior*

All animal behavior was filmed through a glass bottom chamber (25 x 15 inches) with opaque sides and lid using a Google Pixel 5 phone camera (1920x1080 30hz). All mice performed the same panel of behavioral experiments on consecutive days in the order described below. Mice were maintained on a regular 12h light dark schedule, and all experiments were performed in a six-hour window around the transition from light to dark in an isolated dimly lit room. The blinded experimenter exited the room after initializing all tests. Mice were handled daily for one week prior to performing behavioral experiments.

### *Three chamber social task*

The test chamber was divided into three equal sections with plexiglass dividers. A novel C57BL/6 mouse that was age and sex matched to the test animal was placed under a small square cage that was clear and had gaps large enough for nose-to-nose interactions. An identical cage was placed in the opposite chamber, and then the test mouse was placed in the central compartment and allowed to habituate for 5 minutes. After this time, a portion of the Plexiglas divider was removed exposing a path into each side chamber, and the test animal was allowed to explore for ten minutes. After this time, both mice were returned to their home cages, and the apparatus was thoroughly cleaned with 70% EtOH. Mouse, divider, and holding cage position were extracted from

behavioral videos using Deeplabcut (DLC, see below) and social preferences were calculated as index values:

$$\frac{(T_M - T_E)}{(T_M + T_E)}$$

Where  $T_M$  denotes the total time the test mouse spent on the side with the novel mouse and  $T_E$  on the side with the empty chamber.

#### *Novel object recognition and open field task*

Prior to the familiarization phase of the NOR task, mice were allowed to freely explore and habituate to the empty test chamber for 15 minutes. This open field period was recorded, and the mouse and chamber positions were extracted using DLC. We calculated the total distance travelled, average running speed, and percent of time spent in the center (> 3 inches from the walls). After habituation, the test animal was briefly removed, and two identical objects were placed diagonally from one another, 3 inches away from the side wall. The mouse was returned to the chamber and allowed to explore the objects for 7 minutes. 24 hours later, each mouse was returned to the chamber and allowed to explore a novel object placed in a new symmetrical location, and a familiar object used on the day before for a total of 5 minutes. Mouse and object location were extracted using DLC. However, we found that interaction times based solely on proximity using these videos were heavily affected by non-exploratory behaviors near each object, so videos were scored by an independent blind experimenter for time spent interacting with each object based on previously reported guidelines (Leger et al., 2013) (Figure S8). The time spent interacting with the novel  $T^N$  and familiar  $T^F$  objects was recorded during the first 30 seconds of total interaction time.  $T^N$  was compared across groups for

genotype differences, and we tested the null hypothesis  $T^N - T^F = 0$  within each experimental group with a paired student's t-test to determine if there was any preference towards the novel object. Three mice (2 *Scn1a*<sup>+fl</sup>, 1 WT) were excluded for not spending at least 30 seconds interacting with either object (Leger et al., 2013). Total time spent exploring both objects was also reported.

### *Marble Burying*

Compulsive and repetitive behaviors were assessed with a marble burying test. Twelve equally sized marbles were placed in a uniform grid in a standard housing cage with 2 inches of bedding. A single mouse was allowed to explore the cage for 30 minutes, and following this period of time a single en face photo was taken from 1 ft away from the surface of the bedding and was scored for % marbles buried by two blinded experimenters.

### *Elevated plus maze (EPM)*

Two identical EPM apparatus (2ft elevation, arm length of 12 in) with two closed and two open arms were placed in the test room and separated by a white curtain. Videos were taken from 6 ft above the apparatus, and two mice were tested simultaneously if they were from the same housing cage. Mice were placed in the center of the apparatus and allowed to freely explore for 5 minutes. Mouse position and apparatus arm location were extracted with DLC, and both the time and distance travelled on the open ( $T^O$  and  $D^O$ ) and closed ( $T^C$  and  $D^C$ ) arm were calculated. Willingness to explore the open arm was calculated as an index for both time and distance.

$$\frac{(T^O - T^C)}{(T^O + T^C)}$$

### *DLC markerless pose estimation*

DLC (deeplabcut core development branch v0.0b3, compatible with tensorflow 2.3 and Nvidia ampere architecture) was used on a Windows system equipped with an Nvidia RTX 3090 GPU. We used separately trained networks for the following applications: A) Pupil and whisk-ometry during 2P imaging, B) Three chamber social task, C) Open field and NOR task, and D) EPM task. In all cases, we extracted 5 frames per animal (10 for pupillometry) using the *k-means* algorithm and manually labelled the desired body parts and/or apparatus markers (below). For training, we used the resnet 50 pre-trained model, and otherwise default parameters. We trained each network for 300,000 iterations, and then evaluated the networks for accuracy and generalization, and in some cases extracted additional outlier frames for labelling and retrained the network to improve results. Details for the various networks are listed in Table S1.

All marker locations were exported as a csv and analyzed in MATLAB. Where indicate, 'mouse position' refers to an average of the nose, neck, and tail base position. For pupillometry, the four markers identifying the bounds of the pupil were fit with a circle, and the diameter was calculated. Saccades, closed eyelids, and grooming were detected and excluded from analysis. We also extracted a motion index for whisking and found this to be correlated with pupil diameter as previously reported, but we did not include this in our analysis of neural activity. All behavioral data extracted from DLC was filtered with a 300ms rolling average.

### *Statistical analysis*

Because of the highly nested structure of our data, unless otherwise noted we primarily relied on linear mixed effects models to determine significant differences between genotypes. For 2P datasets, where many hundreds of cells are recorded from each animal, we treated individual mice as random effects and genotype as the fixed effect. For a given measured parameter (e.g. MI) we constructed models with default settings in MATLAB using the following formula:

$$MI \sim genotype + (1|mouse) + \epsilon$$

accounting for different baseline values for each mouse (random intercept model). Slope coefficients and errors (normalized as effect sizes in relation to WT values), and p-values representing the estimated difference between genotypes are reported in the main text.

For mouse behavior experiments, we included both male and female mice in our analysis in accordance with guidance from the NIH. We used mixed effects models to test for differences between genotypes

$$behavior \sim genotype + (1 + genotype|sex) + \epsilon$$

and tested whether sex influenced behavior by comparing the above model to a simplified one:

$$behavior \sim genotype + \epsilon$$

Sex only had a trend towards an effect on distance travelled in the open arm of the EPM with males spending less time in the open arm (Effect size: -0.18; Error: 0.06; p-value:

0.1). For all differences we observed between genotypes, sex did not significantly affect performance.

In some indicated cases, within group comparisons are made using a paired student's t-test. For slice electrophysiology experiments, we treated each cell as  $n = 1$  and made all comparisons using the Kruskal-Wallis test as several parameters did not have normal distributions. Sample sizes were not estimated with power analyses but were based on previous studies examining similar phenomenon in models of ASD and epilepsy. All line and bar graphs show mean +/- bootstrapped 95% CI of the mean unless noted otherwise. Boxplots show the median, 25/75<sup>th</sup> and 5/95<sup>th</sup> percentiles, as well as statistically determined outliers as indicated.



## SUPPLEMENTAL FIGURES

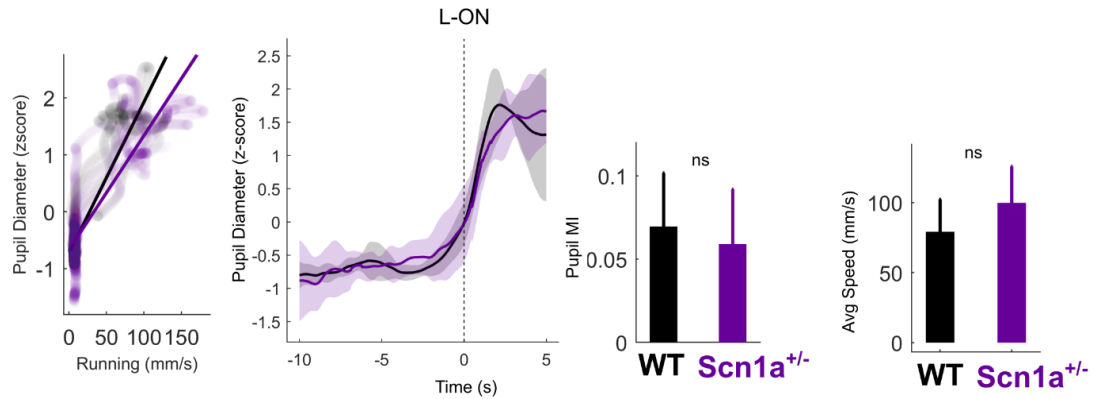


**Figure S1: Markers of behavioral state changes are consistent across genotypes during 2P imaging sessions.** A) Scatter plot of the pupil diameter and running speed from a single trial from a WT and *Scn1a*<sup>+/-</sup> mouse. Each line represents a simple linear fit of the data. B) Average pupil dilation aligned to the onset of locomotion for all WT and *Scn1a*<sup>+/-</sup> mice. C) the increase in pupil diameter during running bouts calculated as an index value. D) Average running speed of all WT and *Scn1a*<sup>+/-</sup> mice.

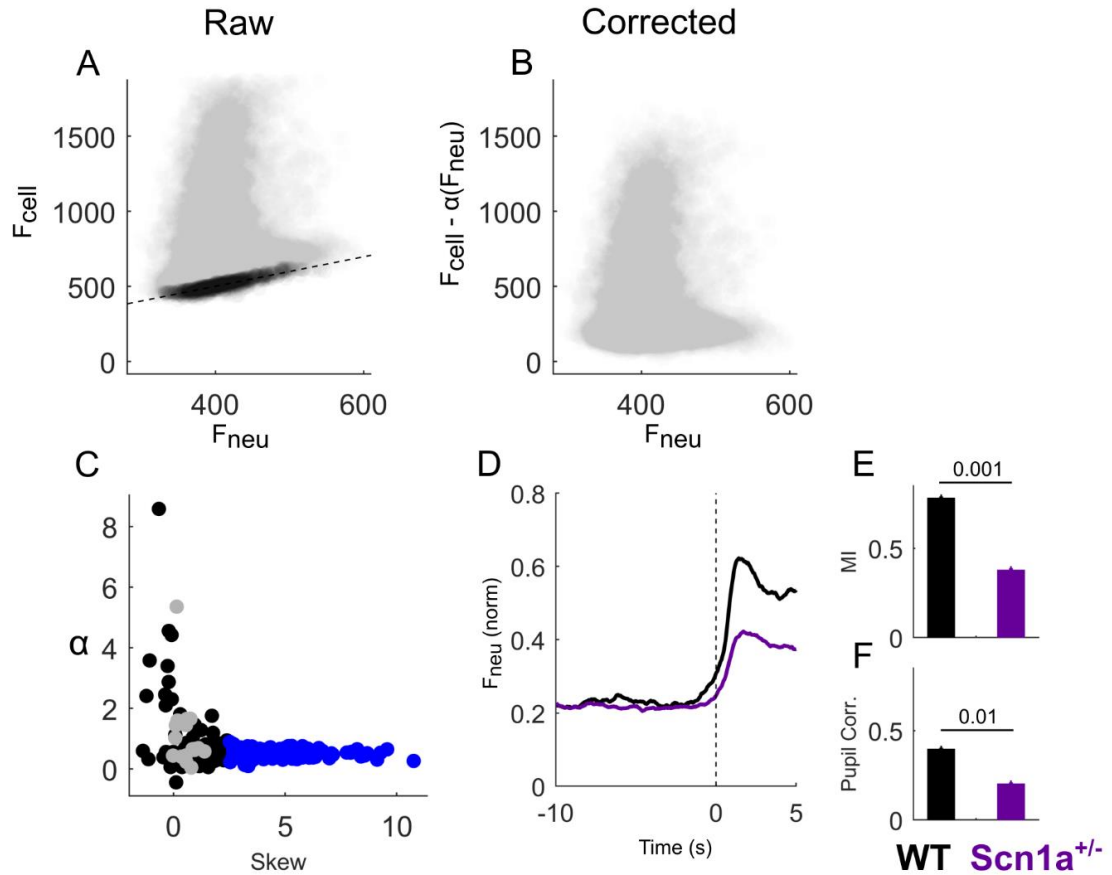


**Figure S2: Neuropil background fluorescence correction.** A) A scatterplot of a single non-VIP neuron from a WT mouse with raw cell fluorescence ( $F_{cell}$ ) plotted on the y axis, and the background neuropil fluorescence for that cell ( $F_{neu}$ ) at the corresponding time point. An algorithm to fit the bottom envelope of this plot, corresponding to the lowest  $F_{cell}$  for any given value of  $F_{neu}$ , was used to calculate the correction factor  $\alpha$  (see Methods). B) The same as in A, but now plotting the corrected cellular fluorescence signal  $F_{cell} - \alpha(F_{neu})$  on the y axis. C) The same process in A-B was carried out for all cells in each field of view, including all VIP-INs (gray) and non-VIP neurons (black). However, to avoid overestimating  $\alpha$  for low skew cells, we averaged  $\alpha$  for cells with skew  $>2.5$  and used this value for all cells with skew  $<2.5$ . D) Average normalized neuropil

signal ( $dF_{neu}/F_{0neu}$ ) as in Figure 1D. E) Locomotion MI of the neuropil signal was reduced in *Scn1a*<sup>+/-</sup> mice. F) Average correlation coefficient with pupil diameter is also reduced.  $n = 2511$  regions from  $n = 5$  WT mice,  $n = 4378$  regions from  $n = 6$  *Scn1a*<sup>+/-</sup> mice.

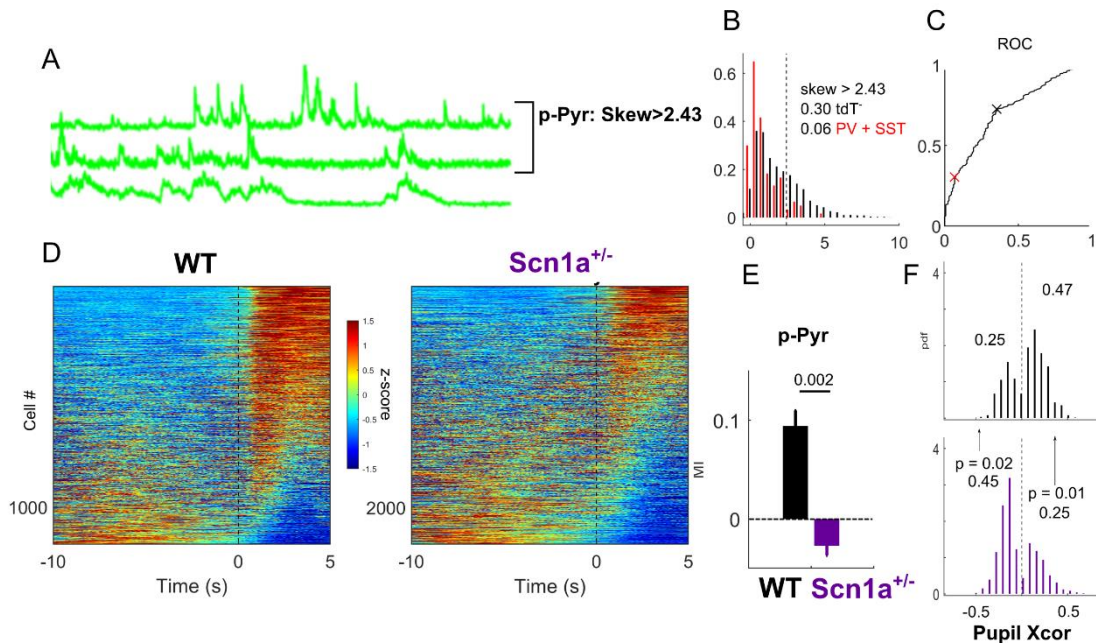


**Figure S3: Isolating definitive pyramidal neurons from tdT<sup>-</sup> non-VIP neurons.** A) Calcium traces (as shown in Figure 3B) from tdT<sup>-</sup> non-VIP neurons have a range with skew values, where high skew cells show sharp transients, and low skew cells have broader transients. B) Left: Histogram of skew values from 2803 tdt<sup>-</sup>, 180 PV-Cre.tdT<sup>+</sup> and 27 SST-Cre.tdT<sup>+</sup> cells (combined, red) from  $N = 6$  WT mice, previously reported data (Somarowthu et al., 2021). Right: Receiver operating characteristic (ROC) curves comparing the skew values from tdT<sup>-</sup> neurons to skew values from PV and SST-INs. The optimal value for distinguishing tdT<sup>-</sup> neurons from PV and SST-INs is indicated by the black X, and when false positives (IN classified as pyramidal neurons) are weighted

twice as much as false negative, the optimum value is shown by the red X. We used this more conservative cutoff of 2.43 in our data to isolate a population of non-VIP neurons that are very likely to be pyramidal neurons (p-Pyr). D) Heatmap of the z-scored  $dF/F_0$  response from each WT and *Scn1a*<sup>+/-</sup> p-Pyr aligned to the onset of locomotion. E) The average locomotion MI for WT and *Scn1a*<sup>+/-</sup> mice. F) Histograms of the correlation coefficient between all p-Pyr and pupil diameter. Only cells that are significantly correlated with pupil diameter are plotted, and the percent which are either positively or negatively correlated are indicated above each histogram.  $n = 1,169$  p-Pyr from  $n = 5$  WT mice,  $n = 2,334$  p-Pyr from  $n = 6$  *Scn1a*<sup>+/-</sup> mice.

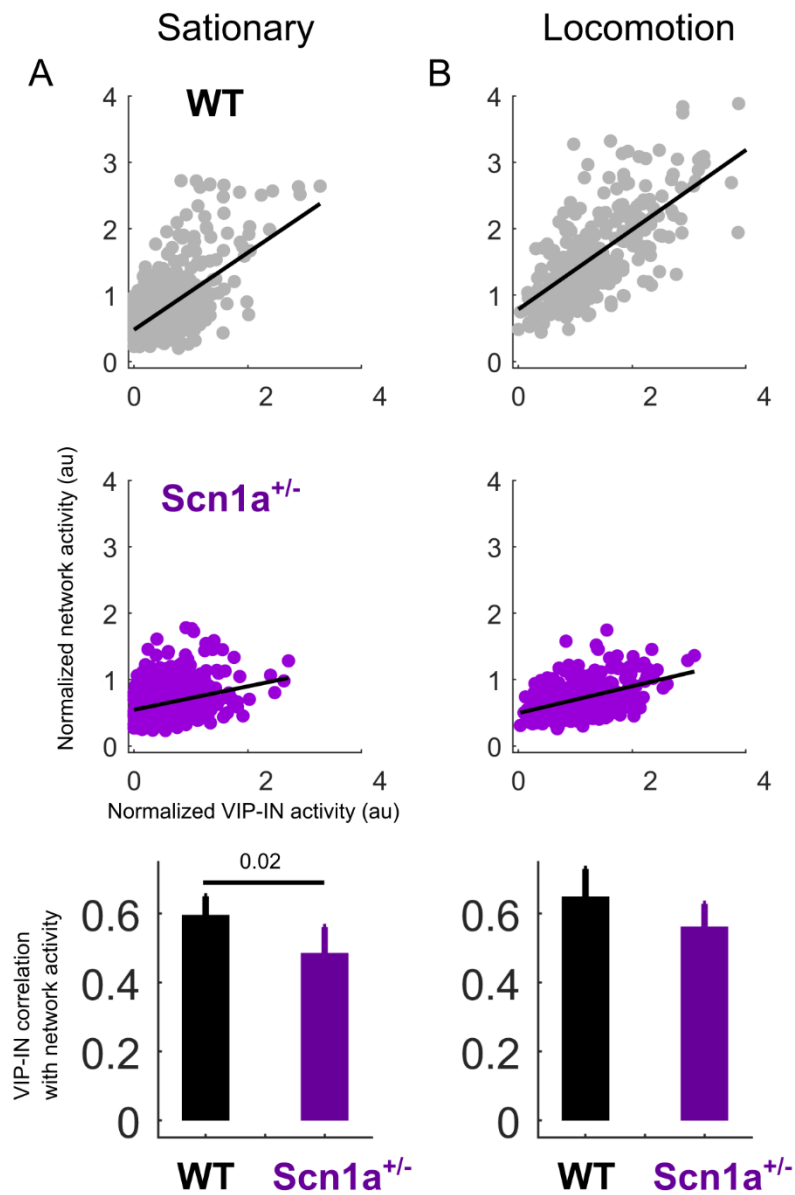


**Figure S4: VIP-IN to network correlation is reduced in *Scn1a*<sup>+/-</sup> mice.** A) Top: Scatter plot of normalized network (non-VIP neurons) and VIP-IN activity for an example imaging experiment during stationary epochs. Each dot represents activity during a 1 second interval. Middle: the same for an example *Scn1a*<sup>+/-</sup> mouse. Bottom: Average VIP-

IN to network correlation is reduced in *Scn1a*<sup>+/-</sup> mice during stationary epochs (Pearson correlation coefficient,  $-0.11 \pm 0.04$ ,  $p = 0.02$ ). B) The same as in A, but during locomotion bouts. Note the increased VIP-IN and network activity in the WT mouse that is not present in the *Scn1a*<sup>+/-</sup> mouse. Bottom: *Scn1a*<sup>+/-</sup> mice trend lower in VIP-IN to network correlation during locomotion bouts ( $-0.08 \pm 0.05$ ,  $p = 0.1$ ).

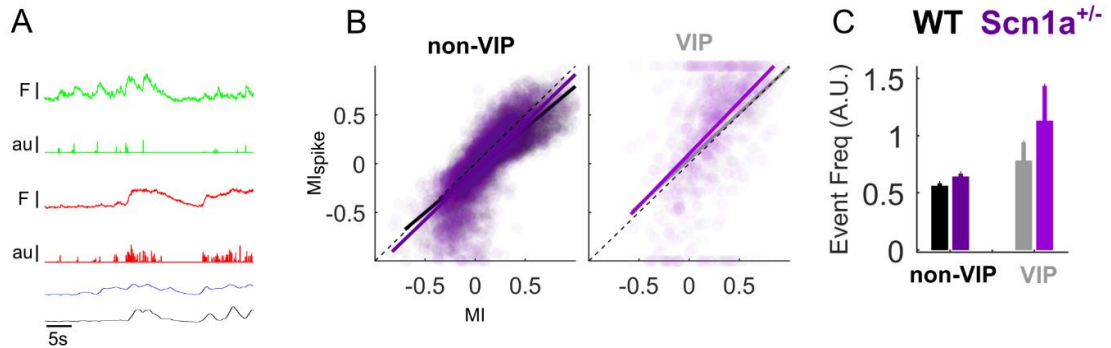


**Figure S5: Event deconvolution from dF/F<sub>0</sub>.** A) Example dF/F<sub>0</sub> traces from a WT VIP-IN and non-VIP neuron, with associated z-scored pupil diameter (*blue*) and locomotion (*black*). B) Calculating the locomotion MI using either dF/F<sub>0</sub> or deconvolved event trains give similar results. Dots represent values for individual cells, and data is fit with a generalized linear model. Slope + intercept: non-VIP neurons,  $0.99x - 0.07$  vs.  $0.87x - 0.07$ , *Scn1a*<sup>+/-</sup> vs. WT ( $p = 0.57$ ,  $p = 0.72$ ); VIP-INS,  $1.07x - 0.1$  vs.  $0.95x - 0.05$ , *Scn1a*<sup>+/-</sup> vs. WT ( $p = 0.33$ ,  $p = 0.88$ ). C) Estimated event rate during stationary epochs is not different between genotypes.  $n = 2511$  tdT- and 368 VIP-INS from  $n = 5$  WT mice,  $n = 4378$  tdT- and 577 VIP-INS from  $n = 6$  *Scn1a*<sup>+/-</sup> mice.

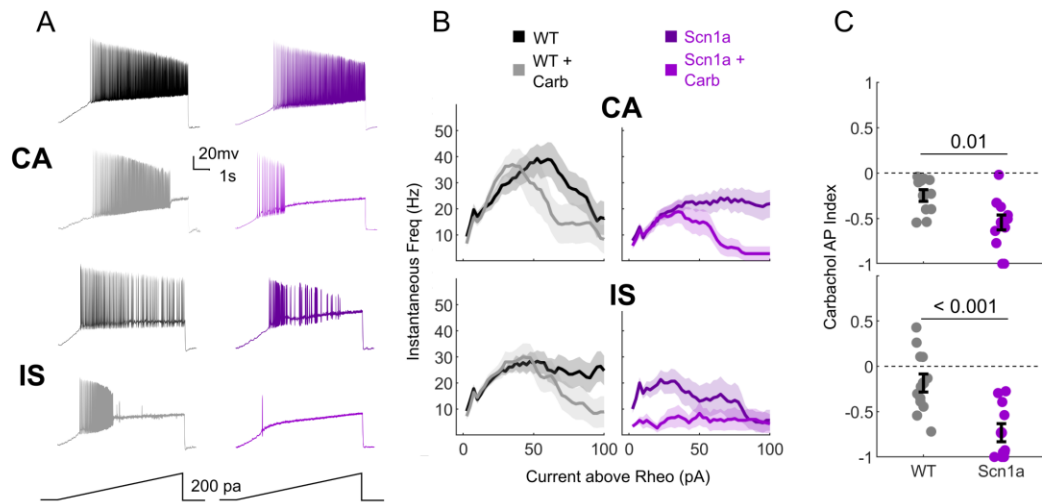


**Figure S6: Carbachol has a similar effect on VIP-INs with differing firing patterns.**

A) Example continuous adapting (CA) and irregular spiking (IS) VIP-INs in acute slices from *Scn1a*<sup>+/-</sup> and WT adult mice. The voltage response to a 200 pA 8s ramping current (as in Figure 1) before and after bath application of 5 μm Carbachol is shown for each cell. B) As in Figure 1 B, the average firing frequency response to 8s ramp depolarizations for both cell types and both genotypes. C) As in Figure 1 E, the effect of carbachol on the total number of spikes generated during an 8s ramp calculated as an index value. Indicated p-values represent differences between genotypes.

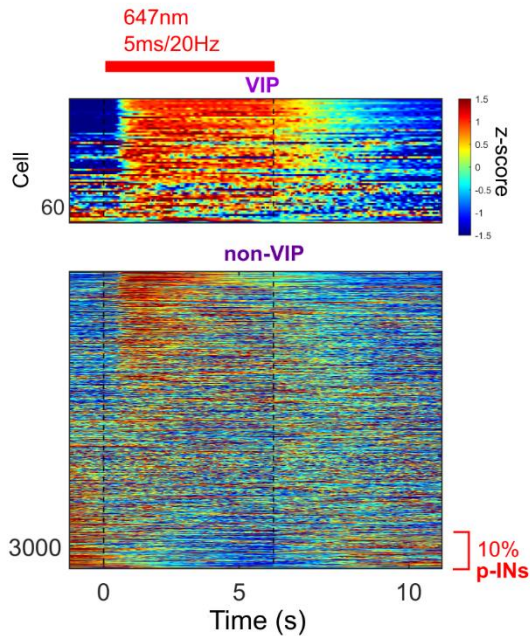


**Figure S7: Diverse network responses in response to optogenetically stimulation of VIP-INs.** Heatmap representing z-scored  $dF/F_0$  of cells during 2P imaging experiments aligned to red laser stimulation (described in Figure 3). Top: VIP-INs expressing ChRimsonR.mCherry are uniformly activated by red light during stationary epochs Bottom: local non-VIP neuron show diverse responses, with a small disinhibitory response in the majority of cells, and a strong inhibitory response in 10% of cells that represent putative inhibitory INs (p-INs ) targeted directly by VIP-INs. Cells are arranged based on correlation with laser stimulation, and the bottom 10% (large negative), which approximates the number of non-VIP neurons in layer II/III (Rudy et al., 2011), are taken to be p-INs.



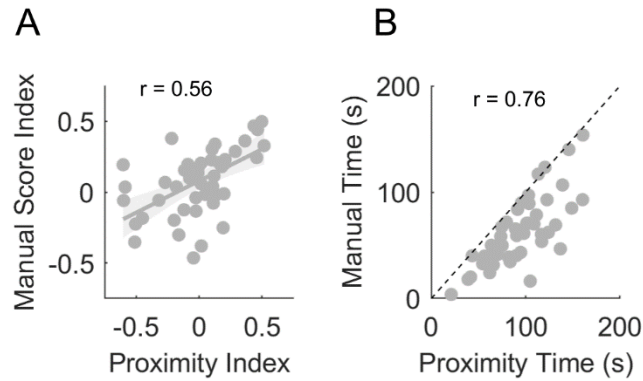


**Figure S8: Comparison of DLC based proximity scoring and blinded manual scoring of NOR interactions.** A) Correlation of the time spent interacting with the novel object as an index, either calculated from manually scored videos or based on proximity from DLC markerless tracking. B) The total time spent exploring either the novel or familiar object when scored manually vs with DLC. Blinded manual scoring rarely produces ‘more’ time interacting (above the dotted line) but often produces a lower amount of total interaction, typically by disregarding grooming or freezing epochs when the animal is close to each object but not exploring the object.

Network	Resolution (down sampled)	FPS (Hz)	Mouse parts labelled (connected by a skeleton)	Apparatus labelled
Three Chamber	960x540	30	Nose, neck, tail base, tail tip	Plexiglass dividers, mouse cage, empty cage
Open field/NOR	960x540	30	Nose, neck, tail base, tail tip, paws, ears	Corners of chamber, 4 demarcated positions 3 inches from the wall, objects if present
EPM	1280x720	30	Nose, neck, tail base, tail tip	Entrance to Open and closed arms
Pupillometry	512x440	100	4 points on pupil (top, bottom, left, right), 2 most posterior whiskers (insertion and tip)	N/A

**Table 2 (S1). Data and network training parameters used in DLC pose estimation.**

## REFERENCES

- Acsády, L., Göröcs, T. J., & Freund, T. F. (1996). Different populations of vasoactive intestinal polypeptide-immunoreactive interneurons are specialized to control pyramidal cells or interneurons in the hippocampus. *Neuroscience*, *73*(2), 317–334. [https://doi.org/10.1016/0306-4522\(95\)00609-5](https://doi.org/10.1016/0306-4522(95)00609-5)
- Almog, Y., Fadila, S., Brusel, M., Mavashov, A., Anderson, K., & Rubinstein, M. (2021). Developmental alterations in firing properties of hippocampal CA1 inhibitory and excitatory neurons in a mouse model of Dravet syndrome. *Neurobiology of Disease*, *148*, 105209. <https://doi.org/10.1016/j.nbd.2020.105209>
- Cantrell, A. R., & Catterall, W. A. (2001). Neuromodulation of Na<sup>+</sup> channels: An unexpected form of cellular plasticity. *Nature Reviews Neuroscience*, *2*(6), 397–407. <https://doi.org/10.1038/35077553>
- Cantrell, A. R., Ma, J. Y., Scheuer, T., & Catterall, W. A. (1996). Muscarinic modulation of sodium current by activation of protein kinase C in rat hippocampal neurons. *Neuron*, *16*(5), 1019–1026. [https://doi.org/10.1016/S0896-6273\(00\)80125-7](https://doi.org/10.1016/S0896-6273(00)80125-7)
- Catterall, W. A. (2017). Forty Years of Sodium Channels: Structure, Function, Pharmacology, and Epilepsy. *Neurochemical Research*, *42*(9), 2495–2504. <https://doi.org/10.1007/s11064-017-2314-9>
- Claes, L., Del-Favero, J., Ceulemans, B., Lagae, L., Van Broeckhoven, C., & De Jonghe, P. (2001). De novo mutations in the sodium-channel gene *SCN1A* cause severe myoclonic epilepsy of infancy. *American Journal of Human Genetics*, *68*(6), 1327–1332. <https://doi.org/10.1086/320609>
- Cohen-Kashi Malina, K., Tsivourakis, E., Kushinsky, D., Apelblat, D., Shtiglitz, S., Zohar,

- E., Sokoletsky, M., Tasaka, G., Mizrahi, A., Lampl, I., & Spiegel, I. (2021). NDNF interneurons in layer 1 gain-modulate whole cortical columns according to an animal's behavioral state. *Neuron*, 1–15.  
<https://doi.org/10.1016/j.neuron.2021.05.001>
- De Stasi, A. M., Farisello, P., Marcon, I., Cavallari, S., Forli, A., Vecchia, D., Losi, G., Mantegazza, M., Panzeri, S., Carmignoto, G., Bacci, A., & Fellin, T. (2016). Unaltered Network Activity and Interneuronal Firing during Spontaneous Cortical Dynamics *in vivo* in a Mouse Model of Severe Myoclonic Epilepsy of Infancy. *Cerebral Cortex*, 26(4), 1778–1794. <https://doi.org/10.1093/cercor/bhw002>
- de Vries, S. E. J., Lecoq, J. A., Buice, M. A., Groblewski, P. A., Ocker, G. K., Oliver, M., Feng, D., Cain, N., Ledochowitsch, P., Millman, D., Roll, K., Garrett, M., Keenan, T., Kuan, L., Mihalas, S., Olsen, S., Thompson, C., Wakeman, W., Waters, J., ... Koch, C. (2020). A large-scale standardized physiological survey reveals functional organization of the mouse visual cortex. *Nature Neuroscience*, 23(1), 138–151.  
<https://doi.org/10.1038/s41593-019-0550-9>
- Dipoppa, M., Ranson, A., Krumin, M., Pachitariu, M., Carandini, M., & Harris, K. D. (2018). Vision and Locomotion Shape the Interactions between Neuron Types in Mouse Visual Cortex. *Neuron*, 98(3), 602-615.e8.  
<https://doi.org/10.1016/j.neuron.2018.03.037>
- Dravet, C. (2011). Dravet syndrome history. *Developmental Medicine and Child Neurology*, 53(SUPPL. 2), 1–6. <https://doi.org/10.1111/j.1469-8749.2011.03964.x>
- Dravet, C., & Oguni, H. (2013). Dravet syndrome (severe myoclonic epilepsy in infancy). In *Handbook of Clinical Neurology* (1st ed., Vol. 111). Elsevier B.V.  
<https://doi.org/10.1016/B978-0-444-52891-9.00065-8>

- Favero, M., Sotuyo, N. P., Lopez, E., Kearney, J. A., & Goldberg, E. M. (2018). A Transient Developmental Window of Fast-Spiking Interneuron Dysfunction in a Mouse Model of Dravet Syndrome. *The Journal of Neuroscience*, *38*(36), 7912–7927. <https://doi.org/10.1523/JNEUROSCI.0193-18.2018>
- Fu, Y., Kaneko, M., Tang, Y., Alvarez-Buylla, A., & Stryker, M. P. (2015). A cortical disinhibitory circuit for enhancing adult plasticity. *ELife*, *2015*(4), 1–12. <https://doi.org/10.7554/eLife.05558>
- Fu, Y., Tucciarone, J. M., Espinosa, J. S., Sheng, N., Darcy, D. P., Nicoll, R. A., Huang, Z. J., & Stryker, M. P. (2014). A Cortical Circuit for Gain Control by Behavioral State. *Cell*, *156*(6), 1139–1152. <https://doi.org/10.1016/j.cell.2014.01.050>
- Gao, Y., Hisey, E., Bradshaw, T. W. A., Erata, E., Brown, W. E., Courtland, J. L., Uezu, A., Xiang, Y., Diao, Y., & Soderling, S. H. (2019). Plug-and-Play Protein Modification Using Homology-Independent Universal Genome Engineering. *Neuron*, *103*(4), 583-597.e8. <https://doi.org/10.1016/j.neuron.2019.05.047>
- Garcia-Junco-Clemente, P., Ikrar, T., Tring, E., Xu, X., Ringach, D. L., & Trachtenberg, J. T. (2017). An inhibitory pull-push circuit in frontal cortex. *Nature Neuroscience*, *20*(3), 389–392. <https://doi.org/10.1038/nn.4483>
- Garrett, M., Manavi, S., Roll, K., Ollerenshaw, D. R., Groblewski, P. A., Ponvert, N. D., Kiggins, J. T., Casal, L., Mace, K., Williford, A., Leon, A., Jia, X., Ledochowitsch, P., Buice, M. A., Wakeman, W., Mihalas, S., & Olsen, S. R. (2020). Experience shapes activity dynamics and stimulus coding of VIP inhibitory cells. *ELife*, *9*, 1–25. <https://doi.org/10.7554/eLife.50340>
- Genton, P., Velizarova, R., & Dravet, C. (2011). Dravet syndrome: The long-term

outcome. *Epilepsia*, 52(SUPPL. 2), 44–49. <https://doi.org/10.1111/j.1528-1167.2011.03001.x>

Goff, K. M., & Goldberg, E. M. (2019). Vasoactive intestinal peptide-expressing interneurons are impaired in a mouse model of dravet syndrome. *ELife*, 8, 1–28. <https://doi.org/10.7554/eLife.46846>

Goff, K. M., & Goldberg, E. M. (2021). A Role for Vasoactive Intestinal Peptide Interneurons in Neurodevelopmental Disorders. *Developmental Neuroscience*, 1–13. <https://doi.org/10.1159/000515264>

Goldberg, E. M., & Coulter, D. A. (2013). Mechanisms of epileptogenesis: a convergence on neural circuit dysfunction. *Nature Reviews Neuroscience*, 14(5), 337–349. <https://doi.org/10.1038/nrn3482>

Gouwens, N. W., Sorensen, S. A., Baftizadeh, F., Budzillo, A., Lee, B. R., Jarsky, T., Alfiler, L., Baker, K., Barkan, E., Berry, K., Bertagnolli, D., Bickley, K., Bomben, J., Braun, T., Brouner, K., Casper, T., Crichton, K., Daigle, T. L., Dalley, R., ... Zeng, H. (2020). Integrated Morphoelectric and Transcriptomic Classification of Cortical GABAergic Cells. *Cell*, 183(4), 935-953.e19. <https://doi.org/10.1016/j.cell.2020.09.057>

Guet-McCreight, A., Skinner, F. K., & Topolnik, L. (2020). Common Principles in Functional Organization of VIP/Calretinin Cell-Driven Disinhibitory Circuits Across Cortical Areas. *Frontiers in Neural Circuits*, 14(June), 1–14. <https://doi.org/10.3389/fncir.2020.00032>

Han, S., Tai, C., Westenbroek, R. E., Yu, F. H., Cheah, C. S., Potter, G. B., Rubenstein, J. L., Scheuer, T., De La Iglesia, H. O., & Catterall, W. A. (2012). Autistic behavior

- in *Scn1a* +/- mice and rescue by enhanced GABAergic transmission. *Nature*, 489(7416), 385–390. <https://doi.org/10.1038/nature11356>. Autistic
- Harris, K. D., & Thiele, A. (2011). Cortical state and attention. *Nature Reviews Neuroscience*, 12(9), 509–523. <https://doi.org/10.1038/nrn3084>
- Jacob, J. (2016). Cortical interneuron dysfunction in epilepsy associated with autism spectrum disorders. *Epilepsia*, 57(2), 182–193. <https://doi.org/10.1111/epi.13272>
- Jansen, N. A., Perez, C., Schenke, M., Van Beurden, A. W., Dehghani, A., Voskuyl, R. A., Thijs, R. D., Ullah, G., Van Den Maagdenberg, A. M. J. M., & Tolner, E. A. (2021). Impaired  $\theta$ - $\gamma$  Coupling indicates inhibitory dysfunction and seizure risk in adravet syndromemouse model. *Journal of Neuroscience*, 41(3), 524–537. <https://doi.org/10.1523/JNEUROSCI.2132-20.2020>
- Jiang, X., Shen, S., Cadwell, C. R., Berens, P., Sinz, F., Ecker, A. S., Patel, S., & Tolias, A. S. (2015). Principles of connectivity among morphologically defined cell types in adult neocortex. *Science*, 350(6264). <https://doi.org/10.1126/science.aac9462>
- Kaneko, K., Currin, C. B., Goff, K. M., Somarowthu, A., Vogels, T. P., & Goldberg, E. M. (2021). Developmentally-regulated impairment of parvalbumin interneuron synaptic transmission in an experimental model of Dravet syndrome. *BioRxiv*. <https://doi.org/10.1101/2021.07.28.454042>
- Kepecs, A., & Fishell, G. (2014). Interneuron Cell Types: Fit to form and formed to fit. *Nature*, 505(7483), 318–326. <https://doi.org/10.1038/nature12983>. Interneuron
- Khan, A. G., Poort, J., Chadwick, A., Blot, A., Sahani, M., Mrsic-Flogel, T. D., & Hofer, S. B. (2018). Distinct learning-induced changes in stimulus selectivity and interactions of GABAergic interneuron classes in visual cortex. *Nature Neuroscience*, 21(6),

851–859. <https://doi.org/10.1038/s41593-018-0143-z>

- Klapoetke, N. C., Murata, Y., Kim, S. S., Pulver, S. R., Birdsey-Benson, A., Cho, Y. K., Morimoto, T. K., Chuong, A. S., Carpenter, E. J., Tian, Z., Wang, J., Xie, Y., Yan, Z., Zhang, Y., Chow, B. Y., Surek, B., Melkonian, M., Jayaraman, V., Constantine-Paton, M., ... Boyden, E. S. (2014). Independent optical excitation of distinct neural populations. *Nature Methods*, *11*(3), 338–346. <https://doi.org/10.1038/nmeth.2836>
- Krabbe, S., Paradiso, E., d'Aquin, S., Bitterman, Y., Courtin, J., Xu, C., Yonehara, K., Markovic, M., Müller, C., Eichlisberger, T., Gründemann, J., Ferraguti, F., & Lüthi, A. (2019). Adaptive disinhibitory gating by VIP interneurons permits associative learning. *Nature Neuroscience*, *22*(11), 1834–1843. <https://doi.org/10.1038/s41593-019-0508-y>
- Lee, A. T., Cunniff, M. M., See, J. Z., Wilke, S. A., Luongo, F. J., Ellwood, I. T., Ponnaveolu, S., & Sohal, V. S. (2019). VIP Interneurons Contribute to Avoidance Behavior by Regulating Information Flow across Hippocampal-Prefrontal Networks. *Neuron*, *102*(6), 1223-1234.e4. <https://doi.org/10.1016/j.neuron.2019.04.001>
- Lee, S., Kruglikov, I., Huang, Z. J., Fishell, G., & Rudy, B. (2013). A disinhibitory circuit mediates motor integration in the somatosensory cortex. *Nature Neuroscience*, *16*(11), 1662–1670. <https://doi.org/10.1038/nn.3544>
- Leger, M., Quiedeville, A., Bouet, V., Haelewyn, B., Boulouard, M., Schumann-Bard, P., & Freret, T. (2013). Object recognition test in mice. *Nature Protocols*, *8*(12), 2531–2537. <https://doi.org/10.1038/nprot.2013.155>
- Lunden, J. W., Durens, M., Phillips, A. W., & Nestor, M. W. (2019). Cortical interneuron function in autism spectrum condition. *Pediatric Research*, *85*(2), 146–154.



<https://doi.org/10.1038/s41390-018-0214-6>

McGinley, M. J., Vinck, M., Reimer, J., Batista-Brito, R., Zaghera, E., Cadwell, C. R., Tolias, A. S., Cardin, J. A., & McCormick, D. A. (2015). Waking State: Rapid Variations Modulate Neural and Behavioral Responses. *Neuron*, *87*(6), 1143–1161. <https://doi.org/10.1016/j.neuron.2015.09.012>

Meisler, M. H., Hill, S. F., & Yu, W. (2021). Sodium channelopathies in neurodevelopmental disorders. *Nature Reviews Neuroscience*, *22*(3), 152–166. <https://doi.org/10.1038/s41583-020-00418-4>

Millman, D. J., Ocker, G. K., Caldejon, S., Kato, I., Larkin, J. D., Lee, E. K., Luviano, J., Nayan, C., Nguyen, T. V., North, K., Seid, S., White, C., Lecoq, J., Reid, C., Buice, M. A., & de Vries, S. E. J. (2020). VIP interneurons in mouse primary visual cortex selectively enhance responses to weak but specific stimuli. *ELife*, *9*, 1–22. <https://doi.org/10.7554/eLife.55130>

Mossner, J. M., Batista-Brito, R., Pant, R., & Cardin, J. A. (2020). Developmental loss of MeCP2 from VIP interneurons impairs cortical function and behavior. *ELife*, *9*, 1–14. <https://doi.org/10.7554/eLife.55639>

Munoz, W., Tremblay, R., Levenstein, D., & Rudy, B. (2017). Layer-specific modulation of neocortical dendritic inhibition during active wakefulness. *Science*, *355*(March), 954–959.

Newmyer, B. A., Whindleton, C. M., Klein, P. M., Beenhakker, M. P., Jones, M. K., & Scott, M. M. (2019). VIPergic neurons of the infralimbic and prelimbic cortices control palatable food intake through separate cognitive pathways. *JCI Insight*, *4*(9). <https://doi.org/10.1172/jci.insight.126283>

- Oakley, J. C., Kalume, F., Yu, F. H., Scheuer, T., & Catterall, W. A. (2009). Temperature- and age-dependent seizures in a mouse model of severe myoclonic epilepsy in infancy. *Proceedings of the National Academy of Sciences of the United States of America*, *106*(10), 3994–3999. <https://doi.org/10.1073/pnas.0813330106>
- Ogiwara, I., Iwasato, T., Miyamoto, H., Iwata, R., Yamagata, T., Mazaki, E., Yanagawa, Y., Tamamaki, N., Hensch, T. K., Itohara, S., & Yamakawa, K. (2013). Nav1.1 haploinsufficiency in excitatory neurons ameliorates seizure-associated sudden death in a mouse model of dravet syndrome. *Human Molecular Genetics*, *22*(23), 4784–4804. <https://doi.org/10.1093/hmg/ddt331>
- Pachitariu, M., Stringer, C., Dipoppa, M., Schröder, S., Rossi, L. F., Dalgleish, H., Carandini, M., & Harris, K. D. (2017). Suite2p: beyond 10,000 neurons with standard two-photon microscopy. *BioRxiv*. <https://doi.org/10.1101/061507>
- Pfeffer. (2013). Inhibition of Inhibition. *Nat Neurosci*, *16*(8), 1068–1076. <https://doi.org/10.1038/nn.3446>.Inhibition
- Pi, H. J., Hangya, B., Kvitsiani, D., Sanders, J. I., Huang, Z. J., & Kepecs, A. (2013). Cortical interneurons that specialize in disinhibitory control. *Nature*, *503*(7477), 521–524. <https://doi.org/10.1038/nature12676>
- Prönneke, A., Witte, M., Möck, M., & Staiger, J. F. (2020). Neuromodulation leads to a burst-tonic switch in a subset of VIP neurons in mouse primary somatosensory (Barrel) cortex. *Cerebral Cortex*, *30*(2), 488–504. <https://doi.org/10.1093/cercor/bhz102>
- Reimer, J., Froudarakis, E., Cadwell, C. R., Yatsenko, D., Denfield, G. H., & Tolias, A. S. (2014). Pupil Fluctuations Track Fast Switching of Cortical States during Quiet

- Wakefulness. *Neuron*, *84*(2), 355–362.  
<https://doi.org/10.1016/j.neuron.2014.09.033>
- Rubinstein, M., Han, S., Tai, C., Westenbroek, R. E., Hunker, A., Scheuer, T., & Catterall, W. A. (2015). Dissecting the phenotypes of Dravet syndrome by gene deletion. *Brain*, *138*(8), 2219–2233. <https://doi.org/10.1093/brain/awv142>
- Rudy, B., Fishell, G., Lee, S., & Hjerling-Leffler, J. (2011). Three groups of interneurons account for nearly 100% of neocortical GABAergic neurons. *Developmental Neurobiology*, *71*(1), 45–61. <https://doi.org/10.1002/dneu.20853>
- Somarowthu, A., Goff, K. M., & Goldberg, E. M. (2021). Two-photon calcium imaging of seizures in awake, head-fixed mice. *Cell Calcium*, *96*, 102380.  
<https://doi.org/https://doi.org/10.1016/j.ceca.2021.102380>
- Tai, C., Abe, Y., Westenbroek, R. E., Scheuer, T., & Catterall, W. A. (2014). Impaired excitability of somatostatin- and parvalbumin-expressing cortical interneurons in a mouse model of Dravet syndrome. *Proceedings of the National Academy of Sciences of the United States of America*, *111*(30), 3139–3148.  
<https://doi.org/10.1073/pnas.1411131111>
- Takayama, R., Fujiwara, T., Shigematsu, H., Imai, K., Takahashi, Y., Yamakawa, K., & Inoue, Y. (2014). Long-term course of Dravet syndrome: A study from an epilepsy center in Japan. *Epilepsia*, *55*(4), 528–538. <https://doi.org/10.1111/epi.12532>
- Takesian, A. E., Bogart, L. J., Lichtman, J. W., & Hensch, T. K. (2018). Inhibitory circuit gating of auditory critical-period plasticity. *Nature Neuroscience*, *21*(2), 218–227.  
<https://doi.org/10.1038/s41593-017-0064-2>
- Tasic, B., Menon, V., Nguyen, T. N., Kim, T. K., Jarsky, T., Yao, Z., Levi, B., Gray, L. T.,

- Sorensen, S. A., Dolbeare, T., Bertagnolli, D., Goldy, J., Shapovalova, N., Parry, S., Lee, C., Smith, K., Bernard, A., Madisen, L., Sunkin, S. M., ... Zeng, H. (2016). Adult mouse cortical cell taxonomy revealed by single cell transcriptomics. *Nature Neuroscience*, *19*(2), 335–346. <https://doi.org/10.1038/nn.4216>
- Tatsukawa, T., Ogiwara, I., Mazaki, E., Shimohata, A., & Yamakawa, K. (2018). Impairments in social novelty recognition and spatial memory in mice with conditional deletion of *Scn1a* in parvalbumin-expressing cells. *Neurobiology of Disease*, *112*(December 2017), 24–34. <https://doi.org/10.1016/j.nbd.2018.01.009>
- Tran, C. H., Vaiana, M., Nakuci, J., Somarowthu, A., Goff, K. M., Goldstein, N., Murthy, P., Muldoon, S. F., & Goldberg, E. M. (2020). Interneuron desynchronization precedes seizures in a mouse model of Dravet syndrome. *Journal of Neuroscience*, *40*(13), 2764–2775. <https://doi.org/10.1523/JNEUROSCI.2370-19.2020>
- Turi, G. F., Li, W. K., Chavlis, S., Pandi, I., O'Hare, J., Priestley, J. B., Grosmark, A. D., Liao, Z., Ladow, M., Zhang, J. F., Zemelman, B. V., Poirazi, P., & Losonczy, A. (2019). Vasoactive Intestinal Polypeptide-Expressing Interneurons in the Hippocampus Support Goal-Oriented Spatial Learning. *Neuron*, *101*(6), 1150-1165.e8. <https://doi.org/10.1016/j.neuron.2019.01.009>
- Yao, Z., van Velthoven, C. T. J., Nguyen, T. N., Goldy, J., Sedeno-Cortes, A. E., Baftizadeh, F., Bertagnolli, D., Casper, T., Chiang, M., Crichton, K., Ding, S.-L., Fong, O., Garren, E., Glandon, A., Gouwens, N. W., Gray, J., Grayback, L. T., Hawrylycz, M. J., Hirschstein, D., ... Zeng, H. (2021). A taxonomy of transcriptomic cell types across the isocortex and hippocampal formation. *Cell*, *184*(12), 3222-3241.e26. <https://doi.org/10.1016/j.cell.2021.04.021>

## Chapter 4: Exploring VIP-INs as a therapeutic target in Dravet Syndrome and Beyond

The data presented so far shows that VIP-INs play a critical role in the underlying disease pathology of Dravet Syndrome (DS). Like somatostatin (SST) and parvalbumin (PV-INs), VIP-INs express Nav1.1, and are hypoexcitable in acute brain slices of *Scn1a<sup>+/-</sup>* mice. However, unlike the other IN subtypes studied so far, this dysfunction persists through development, and is also present when recording VIP-IN activity *in vivo* using two-photon (2P) calcium imaging. A widely conserved disinhibitory circuit function of VIP-INs, regulating cortical state transitions (CSTs) driven by ascending cholinergic neuromodulation, is diminished in *Scn1a<sup>+/-</sup>* mice and, to a lesser extent, in mice when Nav1.1 deletion is limited to VIP-INs. Importantly, Nav1.1 deletion in VIP-INs is sufficient to produce multiple autism spectrum disorder (ASD) related phenotypes that are consistent with both the global DS model, and another neurodevelopmental disorder (NDD) model characterized by ASD endophenotypes and shown to involve VIP-IN dysfunction (Mossner et al., 2020). While the present work is important for understanding DS at a mechanistic level, it is also critical for understanding the basic biology of VIP-IN function and to provide a gateway for studying VIP-INs in a broader context of ASD and intellectual disability (ID). The information summarized above will hopefully lead to investigation of VIP-IN function in a host of disease models in the coming years.

## Searching for disease genes important for VIP-IN function

But is it possible to predict which NDDs are more likely to involve VIP-IN dysfunction? Cutting edge tools and open source big data approaches championed by the Allen Institute and others may allow us to do just that. Single cell RNA sequencing (scRNA-seq) provides quantitative gene expression data on thousands of genes per cell and is scalable up to millions of cells given the appropriate resources. The Allen Institute has several large scale scRNA-seq data-sets available for public use (Gouwens et al., 2020; Tasic et al., 2016; Yao et al., 2021), including the most recent set of data for over 1.1 million neurons from 20 different mouse brain regions using a combination of Smart-Seq and 10X genomics (Yao et al., 2021). This massive amount of high dimensional quantitative data is well-positioned for identification of cell types, particularly when correlated with morphological and electrophysiological data (Gouwens et al., 2018, 2020; Scala et al., 2020; Yuste et al., 2020). However, such data is also useful for hypothesis generation when there is limited direct data available for use (Goff and Goldberg, 2019; Yuste et al., 2020). We analyzed this scRNA-seq dataset (available at <https://portal.brain-map.org/atlas-and-data/rnaseq>) to probe the expression of genes associated with NDDs in VIP-INs.

We selected a group of disease genes used for clinical diagnosis of NDDs that are found on standard academic and commercially available NextGen sequencing panels (CHOP Epilepsy Panel v1.0 and a commercial ASD Panel). These two panels include approximately 250 unique genes (140 on the ASD panel, 76 on the Epilepsy panel, 25 shared between the two panels) with murine homologues found in the Allen Brain data. The most common genetic causes of NDDs found in children, including both Dravet (*SCN1A*) and Rett syndrome (*MECP2*), are covered by this selection of genes.

**Cell Type Specific Expression  
Of Neurodevelopmental Disorder Genes**

<b>ASD Panel</b>					
<b>Gene</b>	<b>VIP</b>	<b>SST</b>	<b>PV</b>	<b>other IN</b>	<b>Glu</b>
Nbea	10.2 * †	8.9	9.0	8.7	9.3
Auts2	10.2 * †	9.3	9.1	9.5	9.6
Ank3	10.3 * †	9.9	9.7	9.9	10.0
Zbtb20	8.9 * †	7.7	8.0	8.3	7.3
Nrxn1	12.0 * †	10.5	9.7	10.8	11.2
Nrxn3	12.9 * †	12.7	11.8	11.5	11.4
Cntn6	5.1 * †	4.3	3.0	1.4	0.5
Setbp1	8.4 * †	7.7	8.3	7.4	7.9
Myt1l	9.3 †	9.1	8.6	8.7	9.1
Son	8.1	7.8	7.8	8.0	8.0
Tcf4	11.4 * †	10.8	10.9	11.2	9.5
Dscam	9.5 * †	8.7	0.8	2.2	8.6
Rere	8.3 *	8.3	8.2	8.2	7.8
Cttnbp2	8.5 †	8.0	7.7	8.1	8.7
Cacna2d3	8.9 * †	9.2	0.3	3.4	8.3
Tnrc6b	7.7	7.5	7.7	7.6	7.5
Nfix	8.0 †	0.0	0.0	8.8	8.1
Grip1	9.9 *	10.4	10.2	10.6	3.5
Cntnap2	11.5 *	11.5	12.1	11.6	9.4
Cacna1c	7.9	8.2	7.3	7.9	8.0
Tanc2	8.5	8.4	8.4	8.3	9.0
Shank2	3.3 †	2.4	1.8	3.5	7.4
<b>Epilepsy Panel</b>					
Zeb2	9.6 * †	8.8	9.3	9.3	8.0
Ryr3	2.4 †	1.2	0.0	0.5	3.2
Gabra1	9.3 †	4.7	9.8	9.4	8.7
Scn3a	2.6 †	2.7	0.4	2.8	4.0
Chrna4	0.3 * †	0.2	0.0	0.9	0.0
Gnao1	8.7	8.8	8.2	9.3	8.7
Lgi1	4.8 †	3.8	2.2	7.6	7.3
Prickle1	7.9	7.5	8.0	7.9	9.1
Atp1a3	9.1	9.4	9.7	9.2	8.8
Kcnc1	5.0 *	7.8	9.5	8.1	2.1
<b>Shared Genes</b>					
Ube3a	9.3 *	9.2	9.1	9.0	8.8
Grin2b	10.4 †	10.2	10.1	10.1	10.6
Slc6a1	8.7 *	9.3	10.3	10.5	0.0
Scn1a	7.8 *	7.9	9.0	8.0	4.6
Scn2a	8.7	8.8	7.7	8.8	9.1
Gabrb3	8.5	8.2	8.1	8.6	9.1
Hcn1	8.6 *	8.4	10.0	9.4	7.6
Cdkl5	4.2 †	1.5	4.0	7.9	7.8
Cask	3.6	4.6	3.6	4.2	7.1
Arx	0.5 *	7.1	4.2	1.8	0.0
...					
Mecp2	2.8	4.3	4.0	4.1	3.6

**Table 1. Cell Type Specific Expression of NDD Genes.** Values are reported as trimmed means (25-75%) of log<sub>2</sub>(CPM). Cell types were assigned based on the “subclass” labels provided by the Allen Institute. “Glu” includes all glutamatergic cells. Genes are ordered based on relative expression in VIP-INs and all Glu (\*) or all other INs combined (†) were determined by bootstrapping the difference in means 50,000 times using 10% of each sample population and a Bonferroni-corrected significance

cutoff. NB, some individual IN subclasses have higher expression of a given gene even if VIP-INs had higher expression than the combined IN pool. The top genes from each panel are shown up to and including all significantly different genes.

---

We first separated the scRNA-seq data based on clustering results from the Allen Institute (Yao et al., 2021) and focused on gene expression in VIP, SST, and PV-INs compared to all other INs (which include the Lamp5, Scng, and Meis2 subclasses) as well as all glutamatergic (Glu) neurons. We then calculated the trimmed mean expression (25%-75% of Log<sub>2</sub>(CPM)) of each gene from the above panels and ranked them based on relative expression in VIP-INs by z-scoring the expression across groups (Figure 1 A-C). Many genes from both panels were expressed at lower levels in VIP-INs (Figure 2D) perhaps because, on average, fewer total reads and genes are recovered from VIP-INs in this dataset compared to other cell types (Yao et al., 2021). This might particularly affect detection of transcripts with low overall expression levels (see Figure 2D, bottom left quadrant). However, there was a subset of genes that were highly expressed in VIP-INs when compared with all INs and/or all Glu neurons (Figure 1, Table 1).

There were several interesting genes that emerged from this analysis that could aid the investigation into the role of VIP-INs in NDDs as well as inform our understanding of the biology underlying VIP-IN function. On the ASD Panel, *NRXN1* and *NRXN3* were the two most highly expressed genes in VIP-INs, and were both in the top 10 in relative expression compared to other cell types (Table 1). Neurexins (*NRXN1-3*) are a family of synaptic adhesion molecules that are critical for synapse and circuit formation during development, and are implicated in many neuropsychiatric disorders including ASD (Kim et al., 2008; Vaags et al., 2012). Their expression is uniquely regulated on a cell type and regional basis at the transcriptional, translational, and post translational level



(Fuccillo et al., 2015), yet nothing is known about how they influence VIP-IN mediated circuits. Mutations in the transcription factor *TCF4* cause Pitt-Hopkins syndrome, a neurodevelopmental disorder defined by ASD with variable but typically severe developmental delay and ID (Sweatt, 2013). *TCF4* itself regulates the expression of both *NRXN1* and *CNTNAP2* (Forrest et al., 2012), which are both enriched in VIP-INS, and pathogenic variants in *NRXN1* and *CNTNAP2* give rise to a Pitt-Hopkins-like syndromes (Zweier et al., 2009). However, little is known regarding the cell type-specific activity of any of these genes.

As an interesting aside, the neurexins, *TCF4*, and *CNTNAP2* are also associated with neuropsychiatric disorders like schizophrenia through genome wide association studies (GWAS), as are several other ASD-associated genes expressed in VIP-INS, including *NBEA* and *CACNA1C* (associated with Timothy Syndrome) (Ripke et al., 2011). *CHRNA5A*, used in the model of nicotine addiction described above (Koukoulis et al., 2017), is also associated with schizophrenia through GWAS (Schizophrenia Working Group of the Psychiatric Genomics Consortium, 2014). While beyond the scope of this discussion, a similar analysis of genes related to various neuropsychiatric disorders could provide new avenues to study the impact of VIP-INS in this class of pathology.

Many disorders - including Rett syndrome and Dravet syndrome - present with an overlap of ASD and epilepsy. Angelman Syndrome is caused by functional silencing of the maternally-imprinted gene *UBE3A* (through deletion, mutation, or aberrant methylation) (Mabb et al., 2011). Interestingly, restricting deletion of *Ube3a* to INs enhances the abnormal EEG and seizure phenotype found in the global or Glu specific murine model (Judson et al., 2016), although relatively similar expression across IN subclasses suggests involvement of multiple cell types (Table 1). *Mecp2* is present

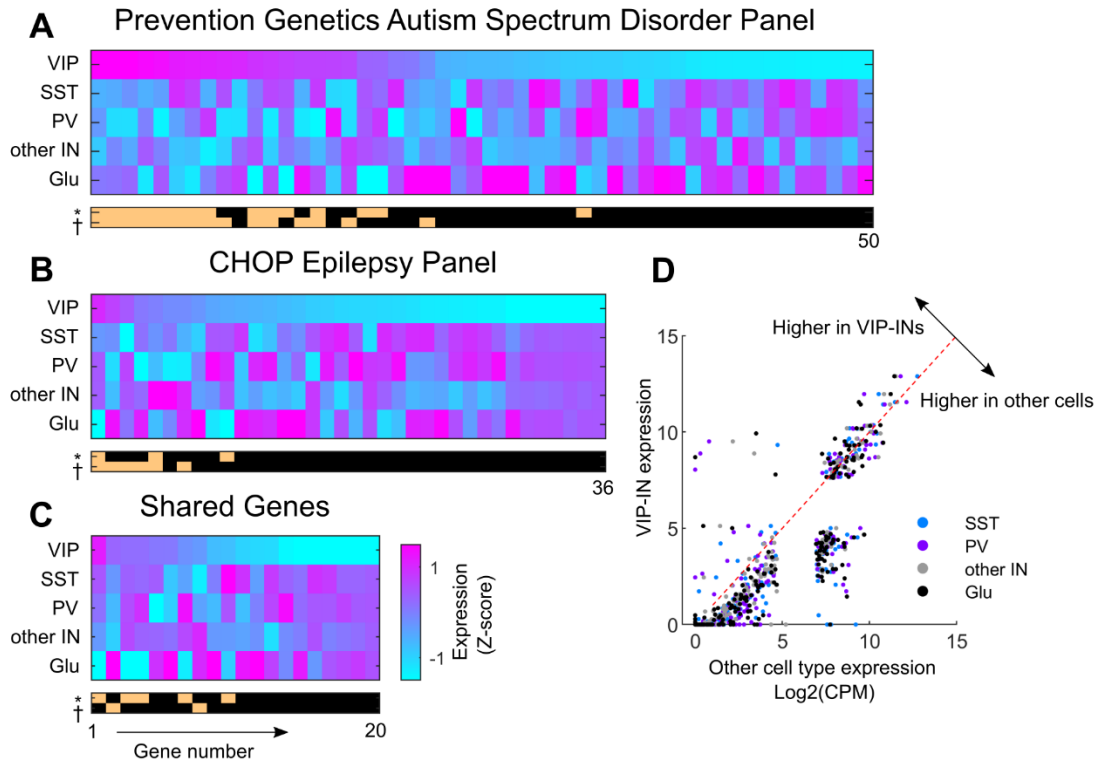


**Figure 1. Relative expression of NDD related disease genes in VIP-INs** A) Heatmap showing the expression of genes in a standard NextGen sequencing panel for ASD calculated as a z-score of the trimmed mean LOG2(CPM) across the 5 indicated cell types. “Other IN” includes all INs not in the three main subclasses (VIP, SST, and PV). Genes are sorted based on relative expression in VIP-INs. Below, tan bars on a black background represent expression of each gene as significantly higher in VIP-INs compared to either all Glutamatergic cells (\*) or all other INs (†, including PV, SST, and other IN). See Table 1 for raw expression values and statistical test information. B) As in Figure 1A, but for genes only found on the CHOP Epilepsy v1.0 Panel. C) The same as Figure 1A-B, but showing genes shared between the two panels. For clarity in Figure 1A-C, genes with no expression in VIP-INs are omitted, including >20 genes with a mean value of 0 in all cell types, and only the first 50 out of 93 genes from the ASD panel are shown. D) A scatter plot of the trimmed mean LOG2(CPM) expression of all 241 genes, where VIP-IN expression is on the Y axis and is plotted against the other indicated cell types on the X axis. Note that equal expression in VIP-INs compared to another subclass would cause the given data point to fall on the indicated diagonal line. Most genes, particularly those that are low expressing, are expressed higher in all other cell types than in VIP-INs. The sparse distribution of points on the top-left of the diagonal line show genes that are enriched in VIP-INs.

although not enriched in VIP-INs in this scRNA-seq data, but decreased *Mecp2* activity can result in lower levels of *Ube3a* and *Gabrb3* (Samaco et al., 2005), both of which are

found at higher levels in VIP-INs. As expected, *Scn1a* is highly expressed in VIP-INs compared to Glu but is similarly expressed compared to other IN subclasses.

Finally, for the Epilepsy panel genes, there were only two that were enriched in VIP-INs compared to both Glu and other INs, highlighting our suggestion that VIP-IN dysfunction may be more closely linked to ASD and ID than epilepsy. Mutations in *ZEB2* cause Mowat-Wilson syndrome which is characterized by moderate to severe intellectual disability, microcephaly, a high rate of Hirschsprung's disease, as well as epilepsy (in 70-75% of cases), but is not a monogenic epilepsy syndrome per se (Cordelli et al., 2013b, 2013a). While expressed at slightly higher levels in adult VIP-INs, *ZEB2* is also prominently expressed across the brain during early development which is more likely to account for the many developmental defects seen in this disorder. The second example, *CHRNA4*, encodes an  $\alpha$  subunit of the nicotinic acetylcholine receptor that is sparsely expressed in the brain compared to *CHRNA2* and 3, similar to *CHRNA5* (Dani and Bertrand, 2007). Mutations in *CHRNA4* cause a subset of autosomal dominant nocturnal frontal lobe epilepsy (ADNFLE), a relatively pure epilepsy syndrome with some motor and cognitive comorbidities (Motamedi and Lesser, 2002). Interestingly, in two mouse models of ADNFLE expressing human *Chrna4a* variants, a seizure phenotype is paradoxically paired with a massive increase in inhibitory post synaptic current frequency recorded from cortical pyramidal neurons after bath application of nicotine (Klaassen et al., 2006). Low dose picrotoxin is able to reduce the abnormal EEG phenotype in these mice, which is counterintuitive and suggests pathologically increased inhibition. In another study, direct activation of  $\alpha 4$ -containing nicotinic acetylcholine receptors also resulted in disinhibition in neocortical layer 5 (Aracri et al., 2017). While these results are not tied directly to VIP-IN function, they are consistent with the

hypothesis that *Chrna4* may be expressed on VIP-INs (Porter et al., 1999), its loss resulting in paradoxically increased inhibition in response to nicotinic stimulation. These studies highlight the complex and varied etiology of seizures and necessitate a better understanding between cell subclass function and disease endophenotype.

For a given NDD, it is possible that the causative disease gene is expressed widely across IN or Glu subclasses (as in *Ube3a* and *Mecp2* above). In other disorders, the causative gene may be preferentially expressed in a specific subclass or subclasses such that the disease predominantly affects a narrow population of cells. While expression of the panel genes across cell types was correlated (Figure 2D), the relative sparsity of genes enriched in VIP-INs suggests that there are at least a handful of diseases that follow this second pattern. We used dimensionality reduction to visualize the expression of 241 NDD-associated genes across IN subclasses (Figure 2A). Surprisingly, the original IN subclasses identified by the Allen Institute were easily extracted from the TSNE1 and TSNE2 dimensions derived from this limited dataset using a simple branching classifier, while the same separation was not possible using random subsets of 250 genes (Figure 2B). Therefore, the information contained within this selection of NDD-associated transcripts is sufficient to distinguish IN subclasses from one another. We suggest that differential disease gene expression across IN subclasses may manifest as distinct disease phenotypes (e.g., epilepsy, features of ASD, ADHD, etc) associated with each subclass. This highlights the potential of investigating the role of disease genes using cell type-specific genetic tools.

### **Points of convergence between experimental models of ASD**

A general theme emerging from the scRNA-seq data discussed above is that disease-related genes enriched in VIP-INs are more highly associated with ASD/ID relative to

developmental epilepsy syndromes. Disorders that have prominent features of both epilepsy and ASD/ID may be the result of mixed dysfunction of multiple cell subclasses. This is perhaps best exemplified by the fact that lesions of PV-INs (genetic or otherwise) tend to produce epilepsy in mice (Jiang et al., 2016; Rubinstein et al., 2015), while lesions restricted to VIP-INs do not produce epilepsy and instead affect attention, learning, and social behavior (Batista-Brito et al., 2017; Fu et al., 2015; Mossner et al., 2020). When integrated together in DS, combined PV and VIP-IN dysfunction closely mirror the development of both epilepsy and ASD. We have discussed the evidence supporting a role for VIP-INs in the pathogenesis of NDDs with features of ASD; however, it is useful to consider this within the broader context of pathological development and function of circuit elements related to ASD, particularly in relation to the role of disinhibition in dendritic integration. For instance, *SCN2A* is also an ASD-associated gene expressed in INs but more prominently in glutamatergic neurons (Table 1). Unlike the DS model, *Scn2a*<sup>+/-</sup> mice exhibit normal PV and SST-IN excitability, yet have early impairment in layer 5b principal neuron excitability (P4) and striking deficiencies in dendritic action potential backpropagation later in development (P27+) (Spratt et al., 2019). This critically interferes with spike timing dependent plasticity and is also correlated with more immature dendritic morphology and a disrupted AMPA-NMDA receptor balance. These results fit well with findings from other ASD models showing abnormalities in synaptic function, either directly involving synaptic proteins or through gene transcription (De Rubeis et al., 2014; Sanders, 2015). In addition, dendritic targeting inhibition provided by SST-INs has precise and compartmentalized control over dendritic integration (Bloss et al., 2016; Chiu et al., 2013; Murayama et al., 2009). Upstream from SST-INs, VIP-INs are poised to have a magnified role over post-synaptic processes like back propagation, spike timing dependent plasticity, and synaptic

integration including during developmental critical periods (Batista-Brito et al., 2017; Fu et al., 2015). Thus, VIP-INs may converge on this common conceptual framework for ASD-associated genes of dysfunctional synaptic plasticity and dendritic integration.

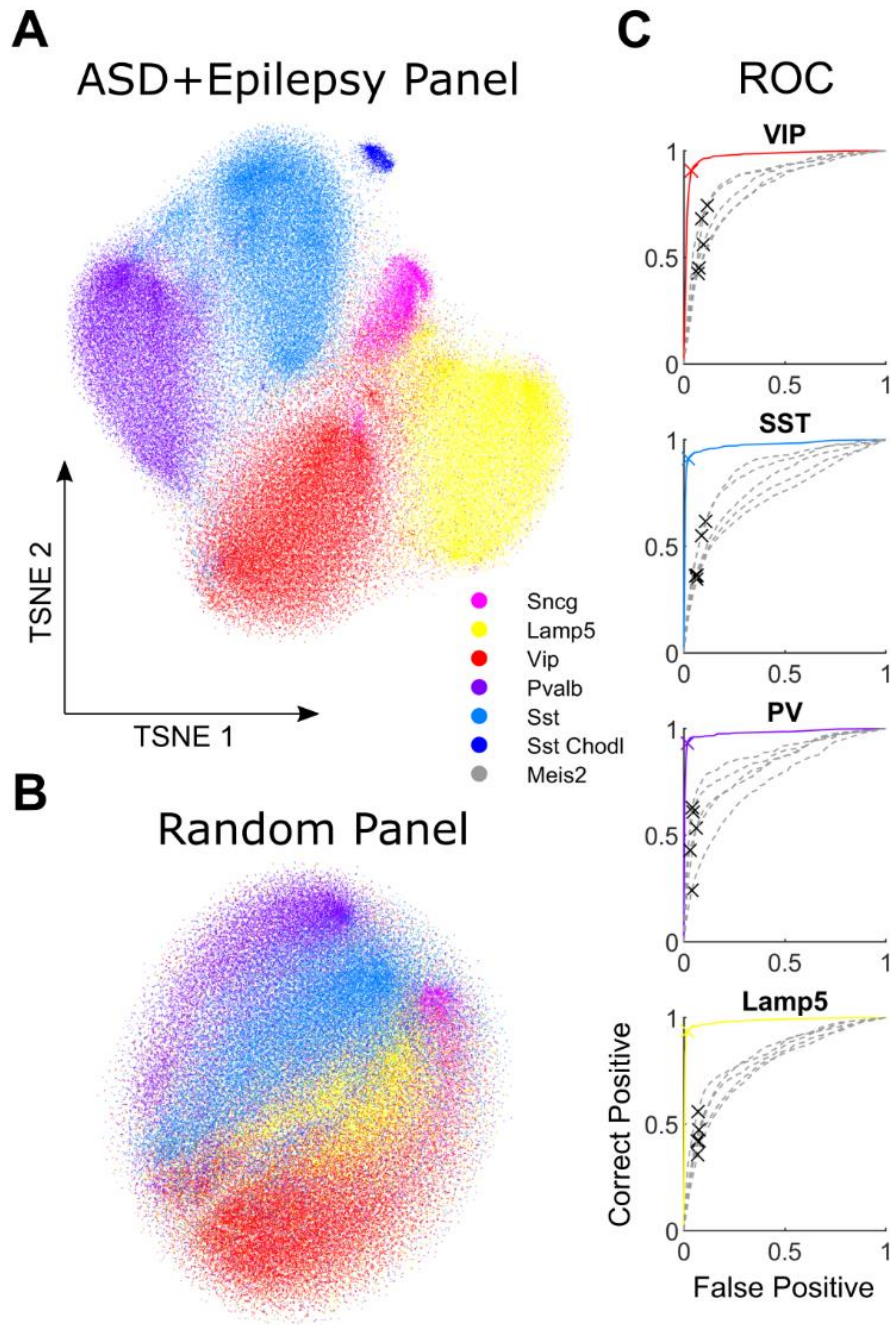


**Figure 2. Separation of IN subclasses based on NDD diagnostic panel genes** A) TSNE plot generated from the first 50 principal components of the 241 unique genes between the ASD and epilepsy panel using the default settings in MATLAB 2019b. Individual cells are coloured based on the cell subclasses identified by the Allen Brain Institute, indicated in the legend. B) The same done for a random selection of 250 genes. The subtypes are more separable when the ASD/Epilepsy panel gene data is used. C) Receiver operating characteristic (ROC) curves demonstrating the effectiveness of a binary decision tree classifier fitted to the TSNE1 and TSNE2 dimensions in A and B at recovering the original subclasses labelled by the Allen Institute. Each ROC curve is created using the posterior probabilities from the trained decision tree classifier model. For each subclass, the coloured line represents a model based on the ASD/Epilepsy gene panels, and the grey lines represent 5 different selections of 250 random genes. The 'X' marks the optimal ROC point for each model. In all cases, the ASD/Panel genes outperform random selections.

---

---

## **Towards cell type-specific therapies**

The evidence we have presented highlights the need to investigate cell-type specific function and dysfunction in NDDs. But why not instead focus on targeting and correcting disease-associated genetic lesions at a global level? Part of the answer to this question lies in the heterogeneity of cell type-specific circuit functions that also change over the course of development. Taking Dravet syndrome as a case study, *SCN1A* was identified as the causative gene twenty years ago (Claes et al., 2001), but the prognosis for children with Dravet syndrome remains bleak. Seizure control in Dravet Syndrome is poor, and SUDEP remains a terrifying spectre for parents. However, even in those patients who attain seizure control, ID and features of ASD remain, and the vast majority are dependent on others for basic care (Berkvens et al., 2015; Genton et al., 2011; Takayama et al., 2014). Aspects of this complex pathology may arise from dysfunction of distinct subclasses of INs that varies over time, suggesting that targeted interventions given at precise developmental timepoints may be necessary to address the distinct aspects of the disease.

Identifying a way to selectively target and manipulate INs could provide an avenue to develop new therapies for Dravet Syndrome. In contrast, global upregulation

of *SCN1A* could theoretically be harmful, as patients with gain of function variants of *SCN1A* suffer from Familial Hemiplegic Migraine Type 3 (Cestèle et al., 2008; Kahlig et al., 2008) and rare *SCN1A* variants identified in an early-onset form of Dravet syndrome have been shown to act via gain of ion channel function (Berecki et al., 2019; Sadleir et al., 2017). VIP-INs remain dysfunctional in young adult *Scn1a*<sup>+/-</sup> mice, while PV-INs follow a different developmental trajectory; hence, *SCN1A* upregulation in discrete IN subclasses would allow for treatments informed by these developmental trajectories targeted to IN subclass-specific disease features. A potential solution to achieving this lies in the *SCN1A* gene itself. There are different enhancer elements within the *SCN1A* locus that drive expression in distinct cell subclasses, including E2 (which drives expression in PV-INs) and E6 (which is limited to VIP-INs) (Vormstein-Schneider et al., 2020). Packaging the E2 enhancer element into a virus creates a tool that selectively drives expression of a desired payload in PV-INs. Moreover, this approach appears to be equally effective in human neurons from cultured brain slices. Ultimately, cell type-specific technology like this could be paired with a gene therapy tool, such as the recently developed catalytically dead Cas9 (dCas9) system that is able to boost Nav1.1 expression and enhance the intrinsic excitability of cultured INs when targeted to the proximal promoter region of the *Scn1a* locus (Colasante et al., 2019). Hypothetically, targeting *Scn1a*-dCas9 or another gene therapy specifically to VIP-INs with the E6 promoter could improve their function without off-target effects and serve as a way to both investigate and address the underlying VIP-IN mediated component of Dravet Syndrome pathology. Perhaps, this approach could be broadly adapted as a therapy for ASD or syndromic NDDs, particularly once we know how mutations in more of the NDD genes identified above affect VIP-IN function.



Novel precision therapeutics that lack subclass specific targeting could still be effective, but ultimately will be limited by the complex and intertwined developmental trajectories of INs. For instance, a single early (P2) dose of an antisense oligonucleotide (ASO) targeting the 'poison exon' (Carvill et al., 2018) in *Scn1a* suppresses a nonproductive alternative splicing event and boosts expression of the remaining copy of *Scn1a*, dramatically suppressing seizures and prevented SUDEP in *Scn1a*<sup>+/-</sup> mice (Han et al., 2020). However, the effect of treatment later in development (P14) is reduced, and treatment after the appearance of spontaneous seizures (P18) – a likely requirement in human patients – is unknown. Further complicating matters, treatment with an ASO targeting *Scn8a* also prevents seizures and SUDEP in *Scn1a*<sup>+/-</sup> mice (Lenk et al., 2020), perhaps indicating that disease symptoms during the chronic phase of Dravet Syndrome may involve homeostatic or pathological upregulation of Nav1.X channel subunits. Treatment boosting *Scn1a* expression in PV-INs later in life, after normalization of intrinsic excitability, might be less effective at controlling seizures. However, treatment at a later developmental timepoint might address the durable deficit in VIP-INs while having limited unintended consequences. As this approach enters human trials (MONARCH Study; monarchstudy.com), it will be critical to determine whether ASOs are capable of not only early seizure control, but long-term seizure control and SUDEP risk reduction as well as an improved neurodevelopmental trajectory without adverse effects.

As we continue to learn more about VIP-INs, accumulating evidence supports the involvement of VIP-IN dysfunction in the pathogenesis of NDDs like DS. Cutting-edge approaches in human and mouse genetics, human induced pluripotent stem cell technology, single cell omics, cell type-specific electrophysiology, opto/chemogenetic manipulation, and *in vivo* imaging in model systems will eventually improve our

understanding of VIP-INs in disease contexts. Ultimately, gene-targeted cell type-specific therapies are on the horizon, informed by continued mechanistic investigation into the basic biological function of disease genes and the circuit roles of defined classes of cells including VIP-INs.

## References

- Aracri, P., Meneghini, S., Coatti, A., Amadeo, A., and Becchetti, A. (2017).  $\alpha 4\beta 2$ (\*) nicotinic receptors stimulate GABA release onto fast-spiking cells in layer V of mouse prefrontal (Fr2) cortex. *Neuroscience* 340, 48–61.
- Batista-Brito, R., Vinck, M., Ferguson, K.A., Chang, J.T., Laubender, D., Lur, G., Mossner, J.M., Hernandez, V.G., Ramakrishnan, C., Deisseroth, K., et al. (2017). Developmental Dysfunction of VIP Interneurons Impairs Cortical Circuits. *Neuron* 95, 884-895.e9.
- Berecki, G., Bryson, A., Terhag, J., Maljevic, S., Gazina, E. V, Hill, S.L., and Petrou, S. (2019). *SCN1A* gain of function in early infantile encephalopathy. *Ann. Neurol.* 85, 514–525.
- Berkvens, J.J.L., Veugen, I., Veendrick-Meekes, M.J.B.M., Snoeijen-Schouwenaars, F.M., Schelhaas, H.J., Willemsen, M.H., Tan, I.Y., and Aldenkamp, A.P. (2015). Autism and behavior in adult patients with Dravet syndrome (DS). *Epilepsy Behav.* 47, 11–16.
- Bloss, E.B., Cembrowski, M.S., Karsh, B., Colonell, J., Fetter, R.D., and Spruston, N. (2016). Structured Dendritic Inhibition Supports Branch-Selective Integration in CA1 Pyramidal Cells. *Neuron* 89, 1016–1030.
- Carvill, G.L., Engel, K.L., Ramamurthy, A., Cochran, J.N., Roovers, J., Stamberger, H., Lim, N., Schneider, A.L., Hollingsworth, G., Holder, D.H., et al. (2018). Aberrant Inclusion of a Poison Exon Causes Dravet Syndrome and Related *SCN1A*-Associated Genetic Epilepsies. *Am. J. Hum. Genet.* 103, 1022–1029.
- Cestèle, S., Scalmani, P., Rusconi, R., Terragni, B., Franceschetti, S., and Mantegazza, M. (2008). Self-limited hyperexcitability: functional effect of a familial hemiplegic migraine

mutation of the Nav1.1 (*SCN1A*) Na<sup>+</sup> channel. *J. Neurosci.* 28, 7273–7283.

Chiu, C.Q., Lur, G., Morse, T.M., Carnevale, N.T., Ellis-Davies, G.C.R., and Higley, M.J. (2013). Compartmentalization of GABAergic inhibition by dendritic spines. *Science* 340, 759–762.

Claes, L., Del-Favero, J., Ceulemans, B., Lagae, L., Van Broeckhoven, C., and De Jonghe, P. (2001). De novo mutations in the sodium-channel gene *SCN1A* cause severe myoclonic epilepsy of infancy. *Am. J. Hum. Genet.* 68, 1327–1332.

Colasante, G., Lignani, G., Brusco, S., Di Bernardino, C., Carpenter, J., Giannelli, S., Valassina, N., Bido, S., Ricci, R., Castoldi, V., et al. (2019). dCas9-Based *Scn1a* Gene Activation Restores Inhibitory Interneuron Excitability and Attenuates Seizures in Dravet Syndrome Mice. *Mol. Ther.* 28, 1–19.

Cordelli, D.M., Pellicciari, A., Kiriazopoulos, D., Franzoni, E., and Garavelli, L. (2013a). Epilepsy in Mowat-Wilson syndrome: Is it a matter of GABA? *Epilepsia* 54, 1331–1332.

Cordelli, D.M., Garavelli, L., Savasta, S., Guerra, A., Pellicciari, A., Giordano, L., Bonetti, S., Cecconi, I., Wischmeijer, A., Seri, M., et al. (2013b). Epilepsy in Mowat-Wilson syndrome: Delineation of the electroclinical phenotype. *Am. J. Med. Genet. Part A* 161, 273–284.

Dani, J.A., and Bertrand, D. (2007). Nicotinic acetylcholine receptors and nicotinic cholinergic mechanisms of the central nervous system. *Annu. Rev. Pharmacol. Toxicol.* 47, 699–729.

Forrest, M., Chapman, R.M., Doyle, A.M., Tinsley, C.L., Waite, A., and Blake, D.J. (2012). Functional analysis of TCF4 missense mutations that cause Pitt-Hopkins syndrome. *Hum. Mutat.* 33, 1676–1686.

- Fu, Y., Kaneko, M., Tang, Y., Alvarez-Buylla, A., and Stryker, M.P. (2015). A cortical disinhibitory circuit for enhancing adult plasticity. *Elife* 2015, 1–12.
- Fuccillo, M. V., Földy, C., Gökce, Ö., Rothwell, P.E., Sun, G.L., Malenka, R.C., and Südhof, T.C. (2015). Single-Cell mRNA Profiling Reveals Cell-Type-Specific Expression of Neurexin Isoforms. *Neuron* 87, 326–340.
- Genton, P., Velizarova, R., and Dravet, C. (2011). Dravet syndrome: The long-term outcome. *Epilepsia* 52, 44–49.
- Goff, K.M., and Goldberg, E.M. (2019). Vasoactive intestinal peptide-expressing interneurons are impaired in a mouse model of dravet syndrome. *Elife* 8, 1–28.
- Gouwens, N.W., Berg, J., Feng, D., Sorensen, S.A., Zeng, H., Hawrylycz, M.J., Koch, C., and Arkhipov, A. (2018). Systematic generation of biophysically detailed models for diverse cortical neuron types. *Nat. Commun.* 9.
- Gouwens, N.W., Sorensen, S.A., Baftizadeh, F., Budzillo, A., Lee, B.R., Jarsky, T., Alfiler, L., Baker, K., Barkan, E., Berry, K., et al. (2020). Toward an Integrated Classification of Cell Types: Morphoelectric and Transcriptomic Characterization of Individual GABAergic Cortical Neurons. *BioRxiv*.
- Han, Z., Chen, C., Christiansen, A., Ji, S., Lin, Q., Anumonwo, C., Liu, C., Leiser, S.C., Meena, Aznarez, I., et al. (2020). Antisense oligonucleotides increase *Scn1a* expression and reduce seizures and SUDEP incidence in a mouse model of Dravet syndrome. *Sci. Transl. Med.* 12.
- Jiang, X., Lachance, M., and Rossignol, E. (2016). Involvement of cortical fast-spiking parvalbumin-positive basket cells in epilepsy. *Prog. Brain Res.* 226, 81–126.
- Judson, M.C.C., Wallace, M.L.L., Sidorov, M.S.S., Burette, A.C.C., Gu, B.,

van Woerden, G.M.M., King, I.F.F., Han, J.E.E., Zylka, M.J.J., Elgersma, Y., et al. (2016). GABAergic Neuron-Specific Loss of Ube3a Causes Angelman Syndrome-Like EEG Abnormalities and Enhances Seizure Susceptibility. *Neuron* 90, 56–69.

Kahlig, K.M., Rhodes, T.H., Pusch, M., Freilinger, T., Pereira-Monteiro, J.M., Ferrari, M.D., van den Maagdenberg, A.M.J.M., Dichgans, M., and George, A.L.J. (2008). Divergent sodium channel defects in familial hemiplegic migraine. *Proc. Natl. Acad. Sci. U. S. A.* 105, 9799–9804.

Kim, H.G., Kishikawa, S., Higgins, A.W., Seong, I.S., Donovan, D.J., Shen, Y., Lally, E., Weiss, L.A., Najm, J., Kutsche, K., et al. (2008). Disruption of Neurexin 1 Associated with Autism Spectrum Disorder. *Am. J. Hum. Genet.* 82, 199–207.

Klaassen, A., Glykys, J., Maguire, J., Labarca, C., Mody, I., and Boulter, J. (2006). Seizures and enhanced cortical GABAergic inhibition in two mouse models of human autosomal dominant nocturnal frontal lobe epilepsy. *Proc. Natl. Acad. Sci. U. S. A.* 103, 19152–19157.

Koukouli, F., Rooy, M., Tziotis, D., Sailor, K.A., O’neill, H.C., Levenga, J., Witte, M., Nilges, M., Changeux, J.-P., Hoeffler, C.A., et al. (2017). Nicotine reverses hypofrontality in animal models of addiction and schizophrenia HHS Public Access Author manuscript. *Nat Med* 23, 347–354.

Lenk, G.M., Jafar-Nejad, P., Hill, S.F., Huffman, L.D., Smolen, C.E., Wagnon, J.L., Petit, H., Yu, W., Ziobro, J., Bhatia, K., et al. (2020). Scn8a Antisense Oligonucleotide Is Protective in Mouse Models of SCN8A Encephalopathy and Dravet Syndrome. *Ann. Neurol.* 87, 339–346.

Mabb, A.M., Judson, M.C., Zylka, M.J., and Philpot, B.D. (2011). Angelman syndrome:

insights into genomic imprinting and neurodevelopmental phenotypes. *Trends Neurosci.* *34*, 293–303.

Mossner, J.M., Batista-Brito, R., Pant, R., and Cardin, J.A. (2020). Developmental loss of MeCP2 from VIP interneurons impairs cortical function and behavior. *Elife* *9*, 1–14.

Motamedi, G.K., and Lesser, R.P. (2002). Autosomal dominant nocturnal frontal lobe epilepsy. *Adv. Neurol.* *89*, 463–473.

Murayama, M., Pérez-Garci, E., Nevian, T., Bock, T., Senn, W., and Larkum, M.E. (2009). Dendritic encoding of sensory stimuli controlled by deep cortical interneurons. *Nature* *457*, 1137–1141.

Porter, J.T., Cauli, B., Tsuzuki, K., Lambolez, B., Rossier, J., and Audinat, E. (1999). Selective excitation of subtypes of neocortical interneurons by nicotinic receptors. *J. Neurosci.* *19*, 5228–5235.

Ripke, S., Sanders, A.R., Kendler, K.S., Levinson, D.F., Sklar, P., Holmans, P.A., Lin, D.-Y., Duan, J., Ophoff, R.A., Andreassen, O.A., et al. (2011). Genome-wide association study identifies five new schizophrenia loci. *Nat. Genet.* *43*, 969–976.

De Rubeis, S., He, X., Goldberg, A.P., Poultney, C.S., Samocha, K., Cicek, A.E., Kou, Y., Liu, L., Fromer, M., Walker, S., et al. (2014). Synaptic, transcriptional and chromatin genes disrupted in autism. *Nature* *515*, 209–215.

Rubinstein, M., Han, S., Tai, C., Westenbroek, R.E., Hunker, A., Scheuer, T., and Catterall, W.A. (2015). Dissecting the phenotypes of Dravet syndrome by gene deletion. *Brain* *138*, 2219–2233.

Sadleir, L.G., Mountier, E.I., Gill, D., Davis, S., Joshi, C., DeVile, C., Kurian, M.A., Mandelstam, S., Wirrell, E., Nickels, K.C., et al. (2017). Not all *SCN1A* epileptic

encephalopathies are Dravet syndrome: Early profound Thr226Met phenotype. *Neurology* 89, 1035–1042.

Samaco, R.C., Hogart, A., and Lasalle, J.M. (2005). Epigenetic overlap in autism-spectrum neurodevelopmental disorders: MECP2 deficiency causes reduced expression of UBE3A and GABRB3. *14*, 483–492.

Sanders, S.J. (2015). First glimpses of the neurobiology of autism spectrum disorder. *Curr. Opin. Genet. Dev.* 33, 80–92.

Scala, F., Kobak, D., Bernabucci, M., Bornaert, Y., Cadwell, C.R., Castro, J.R., Hartmanis, L., Jiang, X., Laturnus, S., Miranda, E., et al. (2020). Phenotypic variation of transcriptomic cell types in mouse motor cortex. *Nature*.

Schizophrenia Working Group of the Psychiatric Genomics Consortium (2014). Biological insights from 108 schizophrenia-associated genetic loci. *Nature* 511, 421–427.

Spratt, P.W.E., Ben-Shalom, R., Keeshen, C.M., Burke, K.J., Clarkson, R.L., Sanders, S.J., and Bender, K.J. (2019). The Autism-Associated Gene *Scn2a* Contributes to Dendritic Excitability and Synaptic Function in the Prefrontal Cortex. *Neuron* 103, 673–685.e5.

Sweatt, J.D. (2013). Pitt-Hopkins Syndrome: Intellectual disability due to loss of TCF4-regulated gene transcription. *Exp. Mol. Med.* 45, 1–15.

Takayama, R., Fujiwara, T., Shigematsu, H., Imai, K., Takahashi, Y., Yamakawa, K., and Inoue, Y. (2014). Long-term course of Dravet syndrome: A study from an epilepsy center in Japan. *Epilepsia* 55, 528–538.

Tasic, B., Menon, V., Nguyen, T.N., Kim, T.K., Jarsky, T., Yao, Z., Levi, B., Gray, L.T., Sorensen, S.A., Dolbeare, T., et al. (2016). Adult mouse cortical cell taxonomy revealed



by single cell transcriptomics. *Nat. Neurosci.* 19, 335–346.

Vaags, A.K., Lionel, A.C., Sato, D., Goodenberger, M., Stein, Q.P., Curran, S., Ogilvie, C., Ahn, J.W., Drmic, I., Senman, L., et al. (2012). Rare deletions at the neurexin 3 locus in autism spectrum disorder. *Am. J. Hum. Genet.* 90, 133–141.

Vormstein-Schneider, D., Lin, J.D., Pelkey, K.A., Chittajallu, R., Guo, B., Arias-Garcia, M.A., Allaway, K., Sakopoulos, S., Schneider, G., Stevenson, O., et al. (2020). Viral manipulation of functionally distinct interneurons in mice, non-human primates and humans. *Nat. Neurosci.* 23, 1629–1636.

Yao, Z., van Velthoven, C.T.J., Nguyen, T.N., Goldy, J., Seden-Cortes, A.E., Baftizadeh, F., Bertagnolli, D., Casper, T., Chiang, M., Crichton, K., et al. (2021). A taxonomy of transcriptomic cell types across the isocortex and hippocampal formation. *Cell* 184, 3222-3241.e26.

Yuste, R., Hawrylycz, M., Aalling, N., Aguilar-Valles, A., Arendt, D., Arnedillo, R.A., Ascoli, G.A., Bielza, C., Bokharaie, V., Bergmann, T.B., et al. (2020). A community-based transcriptomics classification and nomenclature of neocortical cell types. *Nat. Neurosci.* 23, 1456–1468.

Zweier, C., de Jong, E.K., Zweier, M., Orrico, A., Ousager, L.B., Collins, A.L., Bijlsma, E.K., Oortveld, M.A.W., Ekici, A.B., Reis, A., et al. (2009). CNTNAP2 and NRXN1 Are Mutated in Autosomal-Recessive Pitt-Hopkins-like Mental Retardation and Determine the Level of a Common Synaptic Protein in *Drosophila*. *Am. J. Hum. Genet.* 85, 655–666.